Modification of carbon nanocomposites by electromagnetic irradiation for biomedical application

Milica Budimir

UNIVERSITY OF BELGRADE
School of Electrical Engineering

UNIVERSITY OF LILLE
Institute of Electronics,
Microelectronics,
and Nanotechnology (IEMN)

Milica D. Budimir

Modification of carbon nanocomposites by electromagnetic irradiation for biomedical application

Co-directed PhD Thesis

Defence Date: 9 October 2020
President of the jury: Dr. Milan Tadić
Reviewers: Dr. Amitav Sanyal, Dr. Zdenko Špitalsky
Examiner: Dr. Biljana Todorović Marković
Thesis supervisor: Dr. Rabah Boukherroub
Thesis co-supervisor: Dr. Miloš Vujisić

Belgrade, 2020

Универзитет у Београду
Електротехнички факултет

Универзитет у Лилу
Институт за електронику,
микроелектронику
и нанотехнологију

Милица Д. Будимир

Модификација угљеничних нанокомпозита електромагнетним зрачењем за биомедицинску примену

докторска дисертација

у коментерству

Београд, 2020

Université de Belgrade
École de génie électrique

Université de Lille
Institut d'Electronique
de Microélectronique et
de Nanotechnologie (IEMN)

Milica D. Budimir

Modification de nanocomposites de carbone par rayonnement électromagnétique pour des applications biomédicales

Thése de Doctorat en cotutelle

Belgrade, 2020

Mentors:

Dr. Miloš Vujisić, Assistant Professor, University of Belgrade – School of Electrical Engineering

Dr. Rabah Boukherroub, Research Director, Institute of Electronics, Microelectronics and Nanotechnology (IEMN), Lille, France

Jury members:

Dr. Milan Tadić, Full Professor, University of Belgrade – School of Electrical Engineering, Belgrade, Serbia

Dr. Biljana Todorović Marković, Research Professor, "Vinča" Institute of Nuclear Sciences, Belgrade, Serbia

Dr. Amitav Sanyal, Full Professor, Bogazici University, Istanbul, Turkey

Dr. Zdenko Špitalsky, Research Professor, Polymer Insititute, Slovak Academy of Sciences, Bratislava, Slovakia

Date of defense: the 9th of October, 2020

TO MY PARENTS

Acknowledgments

This thesis was prepared as a part of the co-tutorial agreement between the University of Belgrade and the University of Lille. The experiments were performed in "Vinca" Institute of Nuclear Sciences in Belgrade (Laboratory for Radiation Chemistry and Physics) and, the Institute of Electronics, Microelectronics and Nanotechnology in Lille.

I would like to express my deepest thanks to my supervisors Dr. Rabah Boukherroub and Dr. Miloš Vujisić for all the support, discussions and guidance over these four years. They helped me sharpen my scientific thinking and gain the multidisciplinary approach to materials science.

I am deeply thankful to Dr. Biljana Todorović Marković and Dr. Zoran Marković for introducing me to the field of Materials science even before starting my PhD studies, for teaching me scientific and creative thinking, and generously supporting me over the past eight years.

Also, I would like to thank my professor, Dr. Dejan Raković, for giving me the opportunity to see what is it like to be a researcher already at my bachelor studies. Without his guidance and generous help, I would have never been here.

I would like to thank Dr. Sabine Szunerits and Dr. Alexandre Barras for the motivation, great advices, and generous help in the fields that were new to me, and for introducing me to different characterization techniques.

I owe my finest gratitude to my thesis committee members Dr. Milan Tadic, Dr. Amitav Sanyal, and Dr. Zdenko Špitalsky, for accepting to review my thesis.

My deep thanks go to Dr. Roxana Jijie, who generously shared her knowledge and kindness with me, especially in the first months of my stay in France.

This period of moving every six months from one country to another was often hard and overwhelming, but some special people I met on this journey made the whole experience beautiful and unforgettable! I thank my dearest Aleksandra Loczechin and Ioana Hosu, for always being there for me, for all the encouragement, support, and unconditional friendship that lasts. I am so grateful for having you as my little Lilloise family. I thank our fourth musketeer Vedi, for being such a great friend, always ready to cheer us up. I thank Patrik for all the interesting discussions and humor we shared. I thank my dear Anna for genuine kindness and friendship, Vlad and Mathias for all the funny moments and, of course, our Karaoke evenings. I thank Stefania for supportive discussions during our coffee breaks. My stay in Lille would have never been so wonderful without you, dear friends.

I thank all the members of the NanoBioInterfaces group, that I met during the period of my stay in Lille.

I must show my gratitude to my wonderful colleagues from "Vinca" Institute of Nuclear Sciences in Belgrade. I thank Svetlana Jovanović Vučetić, Jovana Prekodravac, and Dejan Kepić for all their help in the chemistry lab, for generously sharing their knowledge with me, and of course, for all those joyful and supportive coffee breaks. I thank Duška Kleut and Dragana Tošić for everything they have taught me about AFM, for their support, patience, and inspiring conversations we shared

over these years. Special thanks go to the lunch group, for the cheerful spirit! I thank my dear friend Danka Stojanović, for her heartfelt friendship and endless encouragement during my PhD.

I thank all the co-authors and collaborators who have helped me undertake this research.

Finally, I owe my deepest gratitude to my parents, to my brother and sister, and my numerous family and friends, for all their love and patience, and for always believing in me, even more than I believed in myself. Finally, I am grateful to Dušan, for endless love, support, and encouragement, especially when I was far from home.

I gratefully acknowledge the financial support from:

- *French Institute in Belgrade and French Government represented by Campus France.*

- *Ministry of Education, Science and Technological Development of the Republic of Serbia via project no. 172003, bilateral project Serbia-Slovakia SK-SRB-2016-0038, and multilateral scientific and technological cooperation in the Danube region (DS-2016-021).*

- *Centre National de la Recherche Scientifique (CNRS), the University Lille, the Hauts-de-France region, the CPER "Photonics for Society", the Agence Nationale de la Recherche (ANR) and the EU union through FLAG-ERA JTC 2015-Graphtivity, and the Marie Sklodowska-Curie action (H2020-MSCA-RISE-2015, PANG-690836).*

Abstract

Microbial contamination is a very important issue worldwide which affects multiple aspects of our everyday life: health care, water purification systems, food storage, etc. Traditional antibacterial therapies are becoming less efficient because inadequate use and disposal of antibiotics have triggered mutations in bacteria that have resulted in many antibiotic-resistant strains. Therefore, it is of great importance to develop new antibacterial materials that will effectively combat both planktonic bacteria and their biofilms in an innovative manner.

In this context, the goal of this thesis was to develop two different carbon/polymer nanocomposites (reduced graphene oxide/polyethylenimine and carbon quantum dots/polyurethane) which exhibit excellent antibacterial properties through two different effects: photothermal and photodynamic. Electromagnetic irradiation was used (near-infrared laser radiation or gamma rays) in these experiments, for the purpose of triggering the photothermal effect and enhancing the photodynamic effect of the nanocomposites.

In the first experimental part of this thesis, a simple and efficient strategy for bacteria capture and their eradication through photothermal killing is presented. The developed device consists of a flexible Kapton interface modified with gold nanoholes (Au NH) substrate, coated with reduced graphene oxide-polyethyleneimine thin films (K/Au NH/rGO-PEI). The K/Au NH/rGO–PEI device was efficient in capturing and eliminating both planktonic Gram-positive *Staphylococcus aureus* (*S. aureus*) and Gram-negative *Escherichia coli* (*E. coli*) bacteria after 10 min of NIR (980 nm) irradiation. Additionally, the developed device could effectively destroy and eradicate *Staphylococcus epidermidis* (*S. epidermidis*) biofilms after 30 min of irradiation.

In the second experimental part, the preparation of a hydrophobic carbon quantum dots/polyurethane (hCQD-PU) nanocomposite with improved antibacterial properties caused by gamma-irradiation pre-treatment is presented. Hydrophobic quantum dots (hCQDs), which are able to generate reactive oxygen species (ROS) upon irradiation with low power blue light (470 nm), were incorporated in the polyurethane (PU) polymer matrix to form a photoactive nanocomposite. Different doses of gamma irradiation (1, 10 and 200 kGy) were applied to the formed nanocomposite in order to modify its physical and chemical properties and improve its antibacterial efficiency. The pre-treatment by gamma-irradiation significantly improved antibacterial properties of the nanocomposite, and the best result was achieved for the irradiation dose of 200 kGy. In this sample, total bacteria elimination was achieved after 15 min of irradiation by blue light, for Gram-positive and Gram-negative strains.

Keywords: antibacterial nanocomposites, reduced graphene-oxide, carbon quantum dots, photodynamic effect, photothermal effect, NIR, gamma-irradiation.

Scientific field: Electrical and Computer Engineering

Scientific subfield: Materials Science in Electrical Engineering (Radiation modified carbon nanomaterials)

Апстракт

Контаминација бактеријама је веома распрострањен проблем који утиче на много различитих аспеката свакодневног живота: здравство, системе за пречишћавање воде, чување хране итд. Традиционалне антибактеријске терапије су постале мање ефикасне, услед неадекватне употребе и одлагања неискоришћених антибиотика, што је довело до мутација бактерија и резултовало појавом многобројних антибиотски отпорних врста. Стога је веома важно да се развију нови антибактеријски материјали који би се ефикасно борили како са планктонским бактеријама тако и са њиховим биофилмовима, на иновативан начин. Сходно томе, циљ ове дисертације био је развијање два различита нанокомпозита на бази угљеника и полимера (редуковани графен оксид/полиетиленимин и угљеничне квантне тачке/полиуретан), који испољавају одлична антибактеријска својства кроз два различита ефекта: фотодинамички и фототермални. Електромагнетно зрачење (блиско инфрацрвено и гама зрачење) коришћено је у оба експеримента, у сврху активирања фототермалног и побољшања фотодинамичког ефекта.

У првом експерименталном делу ове дисертације представљена је једноставна и ефикасна стратегија за хватање бактерија и њихово искорењивање фототермалним убијањем. Развијени уређај се састоји од флексибилног Каптон интерфејса модификованог са златним наношупљинама (Au NH), који је затим обложен танким слојем редукованог графен оксид-полиетиленимина (K/Au NH/rGO–PEI). K/Au NH/rGO–PEI уређај је врло ефикасан у хватању и уклањању планктонских Грам-позитивних *Staphylococcus aureus* (*S. aureus*) и Грам-негативних *Escherichia coli* (*E. coli*) бактерија након 10 мин зрачења ласером у блиској инфрацрвеној области (980 nm). Поред тога, развијени уређај може ефикасно уништити и искоренити биофилмове *Staphylococcus epidermidis* (*S. epidermidis*) након 30 минута озрачивања.

У другом експерименталном делу представљена је припрема нанокомпозита који се састоји од хидрофобних угљеничних квантних тачака и полиуретана (hCQD-PU) са побољшаним антибактеријским својствима узрокованим третманом гама зрачењем. Хидрофобне квантне тачке (енг. hydrophobic carbon quantum dots - hCQD), које су способне да стварају реактивне врсте кисеоника (reactive oxygen species – ROS) након зрачења видљивом плавом светлошћу мале снаге (470 nm), уграђене су у полиуретански (PU) полимер матрикс како би формирали фотоактивни нанокомпозит. Формирани нанокомпозит је затим изложен различитим дозама гама зрачења (1, 10 и 200 kGy) како би се изменила његова физичка и хемијска својства и побољшала његова антибактеријска ефикасност. Третман гама зрачењем значајно је побољшао антибактеријска својства нанокомпозита, а најбољи резултат је постигнут за дозу зрачења од 200 kGy. У овом узорку постигнута је потпуна елиминација бактерија након 15 мин зрачења плавом светлошћу, за Грам-позитивне и Грам-негативне сојеве.

Кључне речи*:* антибактеријски нанокомпозит, редуковани графен оксид, угљеничне квантне тачке, фотодинамички ефекат, фототермални ефекат, гама зрачење.

Научна област: Електротехника и рачунарство

Ужа научна област: Електротехнички материјали и технологије (Угљенични наноматеријали модификовани зрачењем)

Résumé

La contamination microbienne est un problème très important dans le monde entier qui affecte de nombreux aspects de notre vie quotidienne: soins de santé, systèmes de purification de l'eau, stockage des aliments, etc. Les thérapies antibactériennes traditionnelles deviennent moins efficaces, car une utilisation et une élimination inadéquates des antibiotiques ont déclenché des mutations chez les bactéries qui ont conduit à de nombreuses souches résistantes aux antibiotiques. Par conséquent, il est très important de développer de nouveaux matériaux antibactériens pour combattre de manière efficace les bactéries planctoniques et leurs biofilms.

Dans ce contexte, l'objectif de cette thèse était de développer deux nanocomposites différents carbone / polymère (oxyde de graphène réduit / polyéthylénimine et nanostructures de carbone / polyuréthane) originaux qui présentent d'excellentes propriétés antibactériennes à travers deux effets différents : photothermique et photodynamique. Une irradiation électromagnétique a été utilisée (rayonnement laser proche infrarouge ou rayons gamma) dans le but de déclencher l'effet photothermique et d'améliorer l'effet photodynamique des nanocomposites.

Dans la première partie expérimentale de cette thèse, une stratégie simple et efficace pour la capture de bactéries et leur éradication par destruction photothermique est présentée. Le dispositif développé consiste en une interface à base de Kapton modifié avec des nano-trous d'or (Au NH), et recouvert d'une couche mince d'oxyde de graphène/ polyéthylèneimine (K / Au NH / rGO-PEI). Le dispositif K / Au NH / rGO- PEI a été efficace pour capturer et éliminer à la fois les bactéries planctoniques à Gram positif *Staphylococcus aureus* (*S. aureus*) et à Gram négatif *Escherichia coli* (*E. coli*) après 10 min d'irradiation à 980 nm. De plus, le dispositif développé s'est avéré efficace pour détruire et éradiquer des biofilms de *Staphylococcus epidermidis* (*S. epidermidis*) après 30 min d'irradiation.

Dans la deuxième partie expérimentale de ce travail de thèse, la préparation d'un nanocomposite à base de nanostructures de carbone hydrophobes / polyuréthane (hCQD-PU) avec des propriétés antibactériennes améliorées induites par un prétraitement par irradiation gamma est présentée. Des nanostructures de carbone hydrophobes (hCQD), capables de générer des espèces réactives de l'oxygène (ROS) suite à une irradiation avec une lumière bleue de faible puissance (470 nm), ont été incorporées dans la matrice polymère en polyuréthane (PU) pour former un nanocomposite photoactif. Le nanocomposite ainsi formé a été exposé à différentes doses d'irradiation gamma (1, 10 et 200 kGy) afin de modifier ses propriétés physiques et chimiques et d'améliorer son efficacité antibactérienne. Le prétraitement par irradiation gamma a considérablement amélioré les propriétés antibactériennes du nanocomposite, et le meilleur résultat a été obtenu pour la dose d'irradiation de 200 kGy. Cet échantillon a permis l'élimination totale des bactéries après 15 min d'irradiation par la lumière bleue, pour les souches à Gram positif et à Gram-négatif.

Mots-clés : nanocomposites antibactériens, oxyde de graphène réduit, nanostructures de carbone, effet photodynamique, effet photothermique, irradiation gamma.

Contents

PART I: Introduction

This thesis project consists of developing two different carbon/polymer nanocomposites (reduced graphene oxide/polyethyleneimine and carbon quantum dots/polyurethane) that exhibit antibacterial properties through two different effects: photothermal and photodynamic. Additionally, electromagnetic irradiation was used (near-infrared laser radiation and gamma rays), in order to trigger the photothermal effect and enhance the photodynamic effect of the nanocomposites.

Bacterial infections are one of the world's biggest health problems. Traditional antibacterial therapies are becoming less efficient, because inadequate use and disposal of antibiotics have caused mutations in bacteria that led to many antibiotic-resistant bacterial strains. Therefore, the development of novel antibacterial materials that will effectively fight both planktonic Gram-positive and Gram-negative bacteria, and their biofilms is crucial. Microbial contamination is a very important issue that includes multiple fields: health care, water purification systems, food storage, etc. Antibacterial materials can help prevent the formation of biofilms and solve problems related to the use of conventional antimicrobial agents, such as residual toxicity, short-term antimicrobial activity, and development of resistance in microorganisms.

The application of carbon nanomaterials is an emerging area of nanoscience and nanotechnology in the last few decades. When material's dimensions are reduced to nanoscale they display unique physical, chemical, electrical and optical properties compared to their macro-scaled equivalents. Recently, researchers have focused on their biological properties, owing to their great potential as antibacterial agents and their low toxicity.

In the first experimental part of this thesis, a simple and efficient strategy for effective bacteria capture and their subsequent eradication through photothermal killing will be presented. The developed device consists of a flexible Kapton interface modified with gold nanoholes (Au NH) substrate, coated with reduced graphene oxide-polyethyleneimine thin films (K/Au NH/rGO-PEI). The K/Au NH/rGO–PEI device was effective to capture and eliminate efficiently both planktonic Gram-positive *Staphylococcus aureus* (*S. aureus*) and Gram-negative *Escherichia coli* (*E. coli*) bacteria after 10 min of NIR (980 nm) irradiation, and to destroy and eradicate *Staphylococcus epidermidis* (*S. epidermidis*) biofilms after 30 min irradiation.

In the second experimental part, the preparation of a hydrophobic carbon quantum dots/polyurethane nanocomposite (hCQD-PU) with improved antibacterial properties caused by gamma-rays pre-treatment will be discussed. Hydrophobic quantum dots (hCQDs), which are able to generate reactive oxygen species (ROS) upon irradiation with low power blue light (470 nm), were incorporated in the polyurethane (PU) polymer matrix to form a photoactive nanocomposite. Different doses of gamma irradiation (1, 10 and 200 kGy) were applied to the formed nanocomposite in order to modify its physical and chemical properties and improve its antibacterial efficiency. The pre-treatment by gamma-irradiation significantly improved the photodynamic effect in the incorporated hCQDs and consequently, the antibacterial properties of the nanocomposite. The best result was achieved for the irradiation dose of 200 kGy, where the total bacteria elimination was achieved after 15 min of irradiation by blue light, for Gram-positive and Gram-negative strains.

The main contribution of this doctoral thesis is the multidisciplinary approach to the design of novel antibacterial materials and the application of different modification methods in order to change and enhance their properties. Material engineering, chemistry, physics and microbiology were successfully combined in order to achieve the desired results. Two different antimicrobial materials in forms of nanocomposites with the potential in real-life applications, were synthesized and characterized.

Chapter 1. Antimicrobial resistance

In this chapter, I will outline the importance and major challenges of designing antibacterial materials. But first, I need to introduce bacteria and biofilms as concepts, in order to more easily understand the scale of antibiotic resistance and biofilm associated problems.

Bacteria are a *prokaryotic* microorganism, which is typically a few micrometres in length, and have a number of shapes (spheres, rods and spirals). According to the structure, components and function of their cell-wall, bacteria can be divided into two main categories: Gram-positive and Gram-negative. Gram-positive bacteria have a single lipid bilayer surrounded by a thick porous layer of peptidoglycan (20-50 nm), while Gram-negative bacteria have a double lipid bilayer (inner and outer membrane) separated by periplasm and thin peptidoglycan [1] (**Fig. 1.1a, b**). Both Gram-positive and Gram-negative bacteria bear a negative charge [2]. As one of the first forms of life on Earth, they are present in most of its habitats. Additionally, they live in a symbiotic or parasitic relationship with plants, animals and humans. If bacteria live in a parasitic relationship with other organisms, they are called pathogens. Pathogenic bacteria are the main cause of different infections and diseases in humans. The pathogen that so far has the highest disease burden throughout history is *Mycobacterium tuberculosis*, which kills about two million people a year, and is found in both developing and industrialized countries [3]. Other serious infections include nosocomial (hospital-acquired) infections, such as *Clostridium difficile*, *Enterobacter* spp., *Enterococcus faecium*, *Enterococcus faecalis*, *Escherichia coli*, *Haemophilus influenzae*, *Klebsiella pneumoniae*, *Proteus mirabilis*, *Pseudomonas aeruginosa*, *Salmonella* spp., *Serratia* spp., *Staphylococcus aureus*, *Staphylococcus epidermidis*, *Stenotrophomonas maltophilia*, and *Streptococcus pneumoniae* [4]. The term "superbugs" refers to microbes with enhanced morbidity due to multiple mutations providing them a high resistance to antibiotics specifically recommended for their treatment.

Since the discovery of penicillin by Alexander Fleming in 1928, antibiotics have revolutionized medicine and saved countless lives. Unfortunately, the increase in the usage of antibiotics has led to the appearance of many resistant strains. Some predictions are warning of a return to the pre-antibiotic era, with the data confirming over 20,000 potential resistance genes [5].

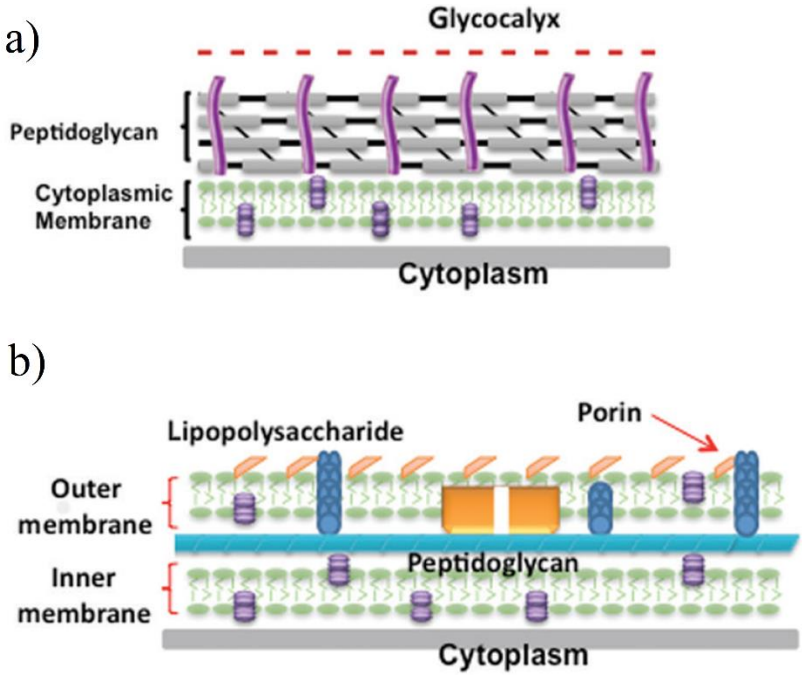

Figure 1.1. The cell wall structure of a) Gram-positive and b) Gram-negative bacteria (reproduced with permission from ref. [2]).

The most notorious Gram-negative pathogens are *Escherichia coli (E. coli)*, *Salmonella enterica*, and *Klebsiella pneumoniae*, which cause a variety of diseases in humans and animals. Over the past fifty years, a strong correlation has been identified between antibiotic use in the treatment of these diseases and the development of antibiotic resistance. Among Gram-positive bacteria, the most prevalent is *Staphylococcus aureus (S. aureus).* It is related to strong skin infections and carried as a nasal commensal in 30% of the population [4]. After the discovery of penicillin, it seemed like *S. aureus* infections were controllable, however, it lasted for a very short time. *S. aureus* and other Gram-positive bacteria could produce enzyme penicillinase, which made them resistant to most of the penicillins. In 1959, methicillin was designed as a first antibiotic that did not contain penicillinase. However, after only 3 years, a new strain of methicillin-resistant *S. aureus* (MRSA) appeared, and shortly after there was a multidrug-resistant strain of *S. aureus.* Not so long ago, MRSA moved from a hospital and became a major community-acquired (CA) pathogen.

Mechanisms and origins of antibiotic resistance are numerous. Molecular mechanisms have been studied extensively, and the findings significantly improved our knowledge about cells. Resistance can occur by modification of RNA or protein components in bacteria cells. The term intrinsic resistance refers to the existence of genes in bacterial genomes that could generate a resistance phenotype, i.e., proto- or quasi- resistance [4]. Among all the possibilities of bacteria to mutate and develop resistance to antibiotics, the human factor has a predominant role in their resistance. Since the 1940s, the amounts of produced antibiotics have been increasing, as well as their use and release in the environment. It is estimated that several million tons of antibiotic compounds have been released into the biosphere over the last 50 years, creating constant maintenance pressure for resistant strains in all the environments [4]. Today, more than 50% of the produced antibiotics are used as additives in animal food, in order to promote animal growth [6]. Another example of human activity that contributes to the environmental reserve of resistance is certainly the use of antibiotics in agriculture and aquaculture. The impact of the disturbing human activity was confirmed by recent studies, which have proven that the acquired resistance to antibiotics was found even in bacteria isolated from humans and wild animals living in remote areas of the planet, who have never been exposed to antibiotic therapies [7,8]. These findings confirm the scale and the complexity of the mechanisms of antibiotic resistance, but also highlight the emergency of finding new innovative measures to fight the bacteria.

1.1 Bacterial adhesion and formation of biofilms

Bacteria can be found in two different forms: the free-floating (planktonic) bacteria, and in the form of a biofilm – a community of bacteria. Biofilm is formed by excreting a slimy, glue-like substance when bacteria adhere to surfaces in moist environments. The sites of biofilm formation include all sorts of surfaces: natural materials, plastics, metals, medical implant materials, even plant and body tissue. It is likely to be found wherever there is a combination of moisture, nutrients and a surface. A single bacterial species may form a biofilm community, however, a majority of biofilms in nature consist of rich mixtures of many species of bacteria, but also fungi, algae, yeasts, protozoa, other microorganisms, debris and corrosion products [9]. For example, in typical dental plaque biofilms, more than 500 bacterial species have been identified [9].

Bacterial adhesion is a very important step in the process of biofilm formation, and it is extremely complicated because it can be affected by many factors such as environmental issues, bacterial characteristics, material surface properties etc. [10]. Bacterial adhesion comprises two phases, first is the initial and reversible physical phase, and the second is time-dependent and irreversible molecular phase [10]. Phase one of bacterial adhesion consists of the initial attraction between cells and the surface through the effects of physical forces: Brownian motion, van der Waals forces, gravitational forces, surface charge electrostatic forces and hydrophobic interactions [10,11]. These forces can be further classified as long-range (distance between cells and surfaces > 50 nm) or

short-range (distance < 5 nm) forces. They are crucial for the initial bacterial adhesion to surfaces. Phase two consists of molecular reactions between bacteria and the surface to which they are about to attach. Bacterial surface polymeric structures, which include capsules, fimbriae, or pili and slime, have a main role in the firm adhesion of bacteria to the surface. The bacterial properties (such as hydrophobicity, surface charge) and surface properties of the material (chemical composition, surface roughness, wettability) are very important in the adhesion process [10,12]. Heaving this in mind, scientists are designing new anti-adhesion materials to stop the biofilm formation. Beyond phase two, some strains are capable of forming a biofilm (**Fig. 1.2**). Following the strong attachment, bacteria start colonizing the surface and creating an extracellular polymeric matrix, which contains a mixture of sugars, proteins, fats and DNA molecules [13]. This matrix makes biofilm extremely resistant to host defense mechanisms, but also creates a physical barrier for antibiotics and disinfectants to reach the bacteria in the biofilm. Additionally, biofilms contain a population of persister cells, which represent the dormant bacterial cells, which survive the antibiotic treatment and adapt to a slow growth rate by forming small sub-colonies [10,14]. Once the structure becomes mature, some bacteria start detaching, enabling the biofilm to spread (**Fig. 1.2**).

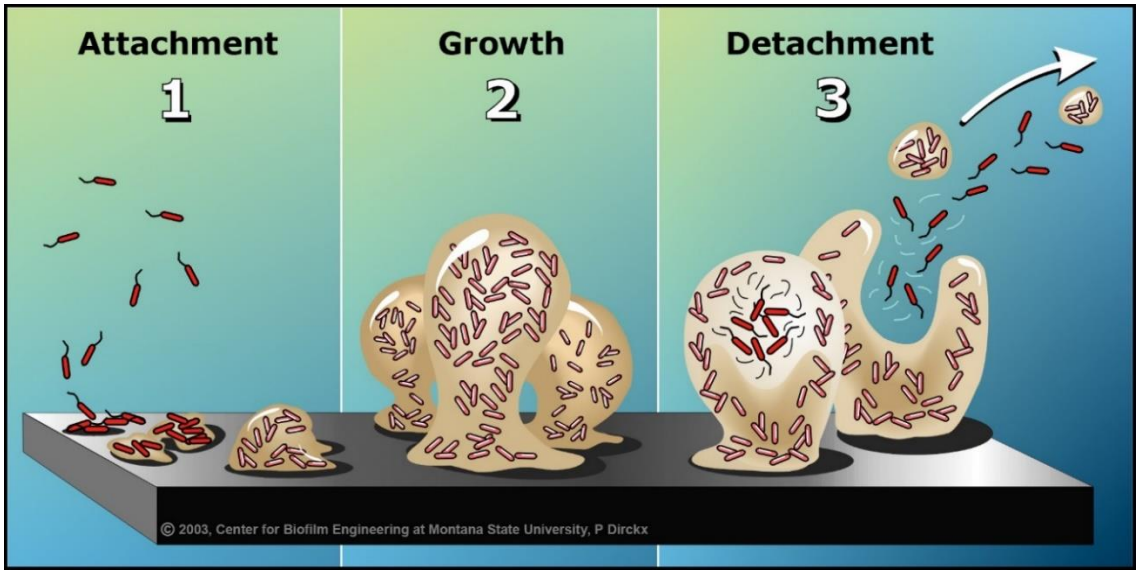

Figure 1.2. Stages of a biofilm life cycle, courtesy of the Montana State University Center for Biofilm Engineering, P. Dirckx.

Nosocomial infections are primarily caused by bacterial colonization of a wide range of biomedical surfaces. The prevalence rate of nosocomial infections ranges from 4% to 10% (reaching up to 30% in intensive care units) in western-industrialized countries, making them the sixth-leading cause of death [15–17]. The proportion is even higher (>15%) in developing countries [18]. The formation of biofilm on a biomedical device for implantation can be very dangerous, leading to many post-surgical complications such as infections, implant rejection and even death [19–21]. Also, the surfaces in the near-patient environment play a major role in the spread of these infections [16]. Therefore, the development of antibacterial surfaces and coatings capable to prevent the bacterial colonization of biomedical surfaces is the key to limiting and eliminating nosocomial infections.

1.2 Nanomaterials as antibacterial agents

Today, there is an urgent need for alternatives to antibiotics, and new antibacterial materials or coatings that would prevent biofilm formation. Microbial contamination is a serious issue, which involves multiple fields, including health care and biomedical industries, water purification systems, food storage and packaging [10]. A disturbing data published by the World Health Organization (WHO) estimate that by 2025 half of the world population will be living in water-stressed areas [22].

Today, around 829 000 people die annually from diarrhea caused by unsafe drinking water [23]. Additionally, there were an estimated 687,000 hospital-acquired infections (HAI) in U.S. acute care hospitals in 2015, and about 72,000 hospital patients with HAIs died during their hospitalizations [24]. These alarming numbers highlight the importance of finding new antimicrobial agents and surfaces.

Nanomaterials and nanotechnology offer a potential replacement for conventional treatment techniques and antibacterial surfaces. Nanomaterials (usually ranging from 1 to 100 nm) exhibit unique physical, chemical and biological properties which are quite different compared to their macro scaled counterparts. Today, nanotechnology-based materials provide a solution to many technological and environmental challenges in different fields, such as water technology, solar energy, catalysis and medicine [10]. Nanomaterials could be used in forms of nanoparticles (NPs) or nanocomposites, and mechanisms of their interaction with bacteria are numerous.

Nanomaterials derived from silver [25–29], gold [30,31], zinc oxide [32,33], calcium oxide [34], titanium dioxide [35–38], magnesium oxide [39], copper oxide [40–42] and graphene-based nanomaterials [43–45] have been researched as efficient coatings, wound dressings, in cosmetics and food storage applications and water treatment. There are many different toxicity mechanisms [1] among nanoparticles, and their main advantage over traditional antibiotics, is the fact that NPs fight the microbes *via* multiple mechanisms simultaneously [46]. For this reason, microbes are unlikely to develop resistance against them, because it is not likely to have multiple mutated genes. However, several studies have revealed that metal nanomaterials induce acute tissue toxicity in humans, which has resulted in their limited use [47].

When it comes to water disinfection, the most important advantages of nanomaterials are their large specific surface area and high reactivity, but also the fact that they are not strong oxidants, and are relatively inert in water. Therefore, they are not expected to form harmful disinfection by-products (DBPs) [48]. Nanoparticles have shown excellent antimicrobial activity towards a broad spectrum of Gram-negative, Gram-positive bacteria [1,21,34,48,49], and fungi [50]. However, there are certain limitations to the direct use of free nanoparticles in water treatment. Firstly, nanoparticles tend to aggregate, which decreases their surface area and thereby their activity [51]. Secondly, certain nanoparticles can be harmful to aquatic life and human health, and thirdly, the separation and disposal or reuse of nanoparticles from the treated water is still a challenging task [52]. Additionally, the fate of released nanomaterials in the aquatic environment needs to be studied more carefully and extensively in the following years, as well as their impact on human health [52].

In order to avoid the potentially adverse effects of nanotechnology, it is very challenging to develop materials that could limit the release of nanoparticles in the environment, but at the same time keep their high reactivity. The development of nanocomposite materials proved to be an effective and promising approach that meets all the required conditions [53]. Nanocomposites can overcome the drawbacks of nanoparticles such as aggregation, the difficulty of separation and leakage into the water, enhance the performance of nanoparticles and allow easier reusability and recycling. The most promising approach is to develop nanocomposites that can take advantage of both, the host material and the impregnated nanoparticles [53]. They are usually designed by incorporating desirable nanoparticles on the supporting material, such as polymers or membranes. Therefore, nanocomposites are often defined as a multiphase material, in which at least one dimension of the component phase is lower than 100 nm [54]. Nanocomposites have promising applications in both water treatment and biomedical field, as antibacterial surfaces and implants.

Some classifications suggest that antibacterial surfaces can be divided into two categories, anti-biofouling and bactericidal [20]. “Anti-biofouling” refers to the surface that is resistant or has the ability to limit the attachment of microbes. On the contrary, “bactericidal surface” allows the attachment of microbes but has a mechanism to disrupt the attached cells, which results in cell death.

Bactericidal surfaces can either chemically or physically disrupt the cell morphology, or by combining both mechanisms [21]. The chemical approach means that the surface is chemically modified, functionalized or coated with biocidal material (nanoparticles [55–58], polymers [59–61], antibiotics [62,63]). While the physical approach includes different methods of modification of the material topography, in order to repel the microbes.

1.3 Photodynamic and photothermal therapy

Photodynamic (PDT) and photothermal therapy (PTT) are very promising alternatives to conventional antibacterial approaches. Both of these treatments are photo-based and they are minimally invasive, with negligible toxicity.

1.3.1 Photodynamic therapy (PDT)

Photodynamic therapy (PDT) is a form of phototherapy which includes the use of a chemical photosensitizer (PS), oxygen and visible light. The concept of photodynamic therapy dates back to 1900, when a medical student Oscar Raab, accidentally discovered that the micro-organisms that had been incubated with certain dyes could be killed when they were exposed to light [64]. After, it was discovered that oxygen is necessary for this effect, so the term "photodynamic action" was coined [65]. However, more profound research and application of PDT started much later [66], in the 1970s, thanks to efforts of Dr. Thomas Dougherty working at Roswell Park Cancer Institute in Buffalo, NY, who introduced the first photosensitizer.

It is proven that PDT kills microbes (bacteria, fungi, and viruses), and therefore, it is used for treating different skin conditions caused by bacteria (acne vulgaris, seborrhoea, rosacea, psoriasis) [67–69], dental infections (periodontitis) [70], in ophthalmology [71] and even gastric Helicobacter Pylori [72]. More importantly, PDT has proven to be efficient against malignant cancer cells, specifically head and neck [73], early-stage lung cancer [74], bladder [74], skin [75], and prostate cancer [76].

- **Mechanism of action**

Molecular oxygen is in the triplet state in nature and tissues, while almost all other molecules are in a single state. Oxygen is relatively inert in physiological conditions because reactions between triplet state and singlet state are "forbidden" by quantum mechanics. A molecule of PS is in the singlet state (ground state) and it has two electrons with opposite spins. When a PS receives one photon of light with appropriate quantum energy (wavelength), one electron is excited into a higher energy orbital (**Fig. 1.3**). This singlet excited state PS is highly unstable, and it is losing its excess energy either by the light emission (fluorescence) or heat generation (internal conversion). However, the excited singlet PS may undergo a process known as "intersystem crossing", in order to create a more stable excited triplet state with parallel spins [65]. This triplet-state PS is much more stable and has a longer lifetime (a few microseconds) than the singlet-state PS (a few nanoseconds). It can decay to the ground state by photon emission (phosphorescence), but more frequently it transfers its energy to molecular oxygen. This process has two pathways:

The Type 1 pathway includes reactions of triplet-state PS with biological substrates (cell membranes, or biomolecules) which result in the production of radical ions. These radicals can react with oxygen and produce **reactive oxygen species (ROS)**, such as **superoxide ($O_2^{\bullet-}$), hydroxyl radical ($^{\bullet}OH$) and hydrogen peroxide (H_2O_2)** [77].

The Type 2 pathway involves energy transfer from the excited triplet state of PS to the ground-state oxygen ($^3O_2$) in order to produce **singlet oxygen ($^1O_2$)**, which can oxidize many biological molecules and lead to cytotoxicity [78]. The generation of ROS is much simpler by the Type 2 pathway, so most of the PSs used in cancer treatment are believed to operate by Type 2 rather than Type 1 mechanism [65]. The whole process is illustrated in **Figure 1.3**.

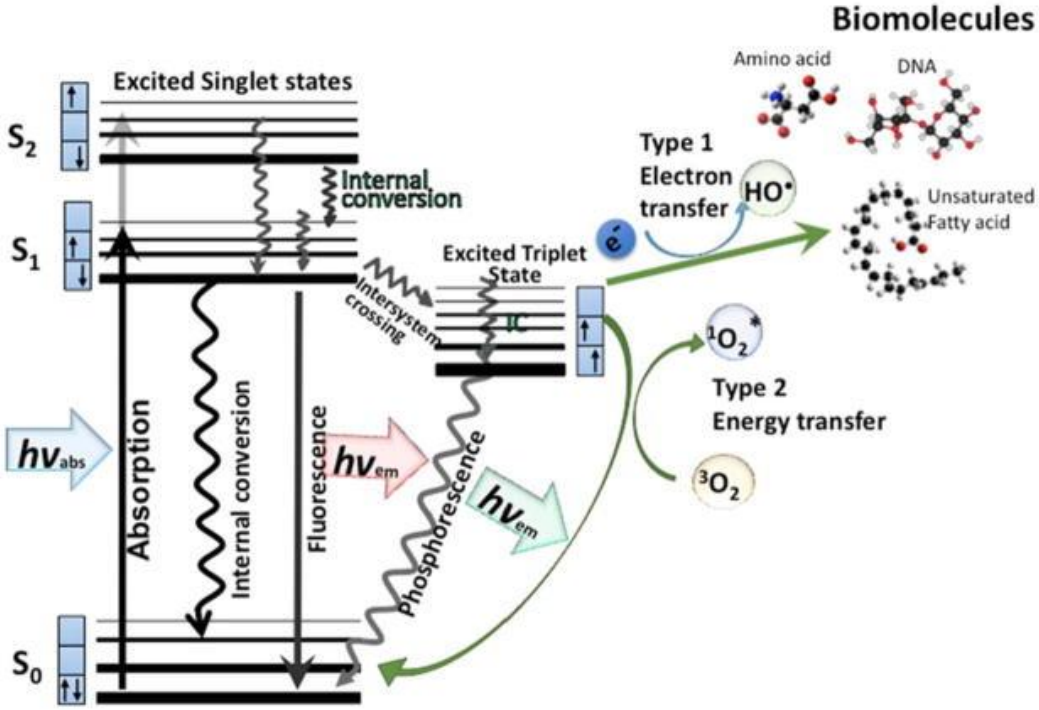

Figure 1.3. Jablonsky diagram. When the PS absorbs light (*hv*), the electron shifts from a non-excited low-energy singlet state to a high-energy singlet state. This excited state can release a photon (fluorescence) or an internal (non-radiative decay) conversion occurs. When the PS reacts with molecular oxygen, Type 1 and Type 2 reactions occur, in which superoxide, hydroxyl radical, hydrogen peroxide (Type 1) and singlet oxygen (Type 2) are formed. Reproduced from [65].

- **Types of photosensitizers and light sources**

An optimal photosensitizer should have favourable physical, chemical and biological properties. There are three generations of PSs used in clinical practice. The first generation was developed in the 1970s and early1980s and belongs to the group of porphyrin-based dyes. The second generation belongs to the group of chlorins, bacteriochlorins, metalated derivatives of PSs etc, and they generally possess higher quantum yield of singlet oxygen. And finally, the third generation of PSs, which should provide the activation with the light of longer wavelength, have better tumour specificity and photosensitivity. There are two pathways of achieving this, either by modifying existing PS with biological conjugates such as peptides and antibodies or by chemical encapsulation of PSs in carriers for a targeted delivery [79].

An ideal PS should possess high stability and water solubility, high ROS production, and a strong absorption peak in red to near infra-red (NIR) region. More importantly, it should not be toxic in dark conditions and should have a rapid clearance from normal tissues [65]. Additionally, there are two drawbacks that are important to overcome by an ideal PS. Light-mediated destruction of PSs, known as “photobleaching”, and a “self-shield” effect, which represents a decrease in the light penetration into tissues, caused by the absorption of light by PS molecules [80]. The application of nanoparticles in PDT is a major step forward in addressing some of the challenges associated with classic PS.

The light source and its wavelength is an important factor that influences PDT. The wavelength of the light source (both lasers and lamps are in use) should match the maximum absorption wavelength of the PS. Most of the PSs absorb in the visible region (below 700 nm), however, the most beneficial is NIR region (700-1100 nm) because of its deep penetration into tissues, without harming the surrounding cells. Also, the advantage of using a laser over a lamp is the emission of highly coherent monochromatic light through an optical fiber, which means that the light can be very precisely delivered to the treatment spot. Consequently, significant efforts are being put into the development of new photosensitizers, which absorb in the NIR region. Naphthalocynanine (776 nm), bacteriochlorin (780 nm), indocyanine green (780 nm) and Alexa fluor (750 nm) are some of them [81].

- **Reactive oxygen species (ROS) and antioxidants**

Reactive oxygen species (ROS) are a group of chemically reactive ions, radicals, and molecules derived from oxygen. ROS are generated as by-products of cellular metabolism, primarily in mitochondria. When the production of ROS is grater than the antioxidant capacity, it can cause damage to cellular macromolecules (lipids, proteins and DNA) [82]. Initially, ROS was considered only as a damaging agent in cell metabolism, however, later it was discovered that it plays a positive role as well. "Humans have a balanced system of reactive species and antioxidants that allows some reactive species to perform useful functions while minimizing oxidative damage" [83].

Very often there is a confusion between terms "reactive oxygen species" and "free radicals", as they are used interchangeably in the literature. This is correct in some cases, but in most cases, it is not. Just to clarify, superoxide anion radical ($O_2^{\bullet-}$), hydroxyl radical ($^{\bullet}OH$) and hydrogen peroxide (H_2O_2) are collectively called reactive oxygen species, but only $O_2^{\bullet-}$ and $^{\bullet}OH$ are free radicals. Apart from them, reactive oxygen species include also diverse peroxides, such as lipid peroxides, and peroxides of proteins and nucleic acids [84]. Other definitions are given in the Glossary. In this thesis, the focus will be mostly on the production of ROS as antimicrobial defense mechanism, through photodynamic therapy.

Glossary

Antioxidant: a molecule that protects a biological target against oxidative damage.
Free radical: any species containing one or more unpaired electrons (electrons singly occupying an atomic or molecular orbital).
Oxidative damage: the damage to cells and tissues caused by reactive oxygen species.
Oxidative stress: a serious imbalance between the generation of reactive oxygen species and antioxidant protection in favor of the former, causing excessive oxidative damage.
Reactive oxygen species: the collective term for oxygen radicals (including hydroxyl $^{\bullet}OH$ or superoxide $O_2^{\bullet-}$) and some other nonradical derivatives of oxygen, such as hydrogen peroxide (H_2O_2), that can easily generate free radicals and/or cause oxidative damage. The superscript dot is the symbol used to denote a free radical. There are also reactive nitrogen, chlorine, iron, copper, and Sulphur species; The general term **'reactive species' (RS)** includes them all. Note that each such species has its own particular types of chemical reactivity.

- Definitions taken from [83]

1.3.2 Photothermal therapy (PTT)

Photothermal therapy (PTT) is an extension of photodynamic therapy, which also includes the use of electromagnetic radiation (usually in infrared wavelength region) for the treatment of various medical conditions, including bacterial infections and cancer [85]. As mentioned earlier, when a photosensitizer is excited by an external light source, it shifts to an excited state (**Fig. 1.3**), and from there it either releases a photon (fluorescence) or releases energy as heat (internal conversion). Photothermal therapy uses this released heat to kill the targeted cells, and it doesn't require oxygen for this interaction (unlike the photodynamic therapy).

Nanotechnology plays a very important role in PTT, offering another alternative approach to treatment of cancer and bacterial infections, which is based on the implementation of heating nanoparticles. According to Jaque et al., the desired properties of those nanoparticles are: i) they are smaller than 100 nm, which enables them easy incorporation into cells, ii) they are dispersable in biocompatible liquids, iii) in the absence of an external stimuli they should exhibit minimal adverse effects on the host biosystem, and iv) they should produce heat efficiently when externally excited [85].

1.3.3 Photothermal and photodynamic treatment of bacteria - state of the art

The lifetime of singlet oxygen is very short (10-320 ns), for this reason, its diffusion is limited to only 10-55 nm in cells, approximately [86]. Therefore, photodynamic damage is most likely to happen close to the intracellular location of PS [87]. There are three main mechanisms of cell death caused by the PDT: apoptotic, necrotic and autophagy-associated cell death. A major role in the type of the cell death mechanism plays a subcellular localization of PS in different organelles. However, it is accepted that apoptosis (programmed cell death) is the principal mechanism of cell death caused by PDT [65]. When it comes to PTT, there are also different mechanisms of cell death, depending on the temperature and time of exposure of cells to the heated nanoparticles. When temperatures are higher than 48°C and exposure is longer than a few minutes, cell death is achieved by a coagulative necrosis process. The effect of such high temperatures is considered drastic and unreversible [88]. However, the problem here is the lack of selectivity and the possibility of damaging also healthy cells. In the temperature range between 41-48°C cells are exposed to hyperthermia, which causes protein denaturation and cell damage [89]. Diathermia treatments include heating up to 41°C. This temperature does not induce significant changes on the cellular level, however, these moderate heating treatments are beneficial for health, and are mainly applied in physiotherapy [85,90].

The structure of PS is very different between anti-cancer drugs and antimicrobial drugs and therapies. Anti-cancer PS is preferably lipophilic with no surface charge, while antimicrobial PS, is preferred to have a positive charge. Additionally, for an anti-cancer PS, it is beneficial to have a longer wavelength (NIR) of an absorption band because of the deeper tissue penetration, while for antibacterial PS this is not necessary [65].

There are numerous reports confirming the excellent results of PDT and PTT in the bacteria eradication. According to Lucky *et al.*, the nanoparticles used in PDT can be classified into (i) PS alone, (ii) carriers of PS and (iii) energy transducers of PS [79]. Additionally, the nanoparticles may be biodegradable (e.g. natural or synthetic polymer-based nanoparticles) and non-biodegradable (e.g. ceramic- and metal-based nanoparticles) [81].

Grinholc et al. used a porphoporphyrin photosensitizer and a light source of 624 nm wavelength to evaluate the photodynamic inactivation of 40 clinical isolates of methicillin-resistant *S. aureus* and 40 clinical isolates of methicillin-sensitive *S. aureus*. The results of the study indicated the reduction of $3\log_{10}$ in the number of bacteria [91]. In another study, Kashef et al. [92] explored

the influence of PDT on *E. coli* (ATCC25922) and resistant strains of *E. coli* using methylene blue (MB) and toluidine blue O (TBO) photosensitizers. Their results showed that MB (50 μg/mL) excited by a laser light (163.8 J/cm^2) induced a reduction of 53.1% and 37.6% of viable *E. coli* (ATCC25922) and drug-resistant *E. coli* (from the initial concentration of 10^4-10^5 CFU/mL). Moreover, TBO (50μg/mL) and a laser dose of 46.68 J/cm^2 killed 98.2% and 83.2% of *E. coli* (ATCC25922) and drug-resistant *E. coli*. Maaoui et al. demonstrated that polyvinyl pyrrolidine-coated Prussian blue nanoparticles (PVP/PB NPs) were an efficient photothermal agent able to inactivate both Gram-positive and Gram-negative pathogens under 810 and 980 nm irradiation for 10 min [93]. Recently, a group of researchers evaluated the efficiency of indosanine green excited by a diode laser (810 nm) on the *Porphyromonas gingivalis*. Their results showed that the number of bacteria was significantly reduced, and the growth of the biofilm was inhibited [94]. There are reports confirming that PS does not have to be in direct contact with the bacteria, to induce the photodynamic effect. If singlet oxygen is generated in sufficient quantities, close to the cell membrane of bacteria, it will be able to diffuse into the cell and cause damage [95]. In some studies, there was even a layer of moist between bacteria and PS, and singlet oxygen was still able to diffuse across the gap [96].

Graphene and graphene-based materials have been extensively studied for PTT, due to their strong ability to convert NIR light into heat. Wang *et al.* used reduced graphene oxide (rGO) functionalized with anti-*S. aureus* polyclonal antibody, through physisorption, for efficient capture and NIR (808nm) killing of *S. aureus* [97]. Colleagues from the group have recently investigated the synergistic effect of gold nanorods and rGO on *E. coli* strain and demonstrated the killing efficiency of 99% of bacteria in solution after only 10 min [98]. They could also achieve a targeted killing of *E. coli* UTI89 by functionalizing graphene coating with multimeric heptyl α-D-mannoside probes. Recently, an antibacterial surface based on a polyelectrolyte-stabilized rGO sheets that kill airborne bacteria on contact upon minutes of solar NIR irradiation was reported by Hui et al. [99]. The observed activity was reported to be retained even when the film was placed underneath a piece of pork tissue, indicating that solar light in the NIR region plays a dominant role in the observed activity.

In summary, photodynamic and photothermal therapies require photosensitizers, the light of a specific wavelength, and oxygen (in the case of PDT). Both PDT and PTT hold a great promise in antimicrobial therapies, due to their efficiency, environment friendliness and the fact that the bacteria are not likely to develop resistance to them. In the experimental part of this thesis, two different strategies to fight microbes are presented. One is based on the photothermal effect on the layer of reduced graphene oxide, and the other uses the photodynamic effect of carbon quantum dots as a new class of photosensitizers. Both of these materials and their properties will be discussed in the following chapters.

Chapter 2. Carbon nanomaterials

Carbon is a basic element of all the organic molecules, and therefore, it is responsible for life on Earth. Also, carbon is a basic building block of all carbon nanomaterials. It is the sixth element in the periodic table, which means that six electrons are surrounding the nucleus (**Fig. 2.1a**) and these electrons are in the following configuration $1s^2 2s^2 2p^2$. The two electrons that occupy the inner shell *1s* are closest to the nucleus and do not affect chemical reactions, while the remaining four electrons occupy the outer shell with *2s* and *2p* orbitals (**Fig. 2.1b**).

For most of the carbon nanomaterials it is characteristic to have an sp^2 hybridization of carbon atoms, resulting from the superposition of one *2s* and two *2p* orbitals (**Fig. 2.1c**). These hybridized orbitals are oriented in the *xy* plane with the 120° angle between them, while the remaining non-hybridized orbital is normal to their plane.

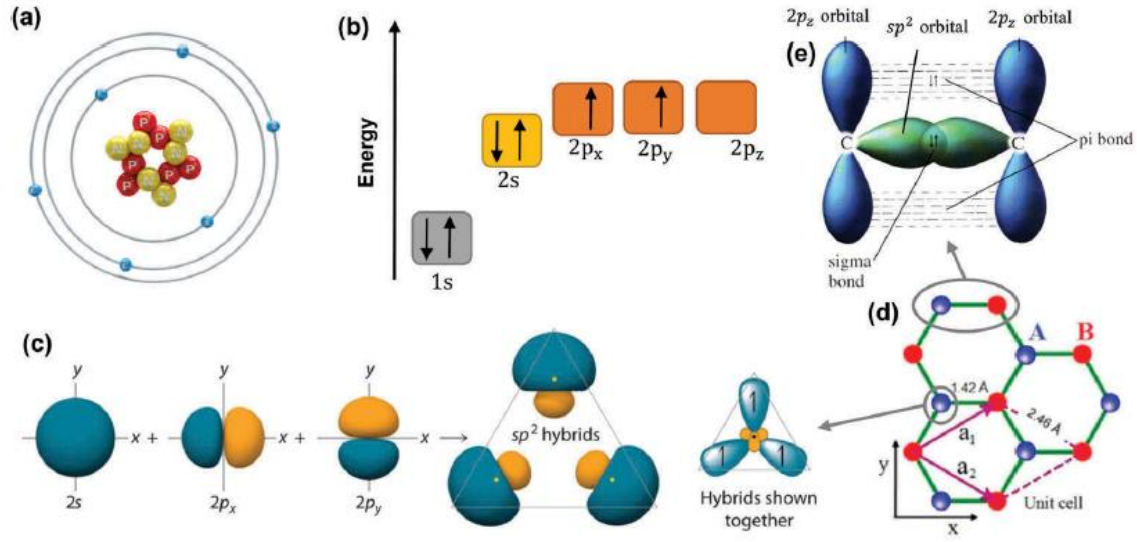

Figure 2.1. (a) Atomic structure of carbon atom. (b) Energy levels of outer electrons in carbon atoms. (c) The formation of sp^2 hybrids. (d) The crystal lattice of graphene, where A and B are carbon atoms belonging to different sub-lattices, a 1 and a 2 are unit-cell vectors. (e) σ bond and π bond formed by sp^2 hybridization. Reproduced with permission from [100].

Carbon has a variety of allotropic modifications, owing to its flexibility and strong bonds. Three of them occur naturally: graphite, amorphous carbon and diamond. The distinction between the three allotropes is the arrangement of the atoms and their bonding within the structure. Diamond possesses a diamond lattice crystalline structure, graphite has lattice structure of the honeycomb, while amorphous carbon (such as coal or soot) has no crystalline structure [101]. Graphite's three-dimensional (3D) structure is useful in various applications like in pencils, batteries, metallurgy, rods, etc.

Carbon nanomaterials include graphene, graphene nanoribbons, carbon nanotubes, nanodiamonds, carbon quantum dots, etc. (**Fig. 2.2**). The physical, chemical, mechanical and other differences between them are due to different structures and shapes. In the experimental part of this thesis, graphene and carbon quantum dots will be used, therefore, in the following chapters their basic properties will be presented.

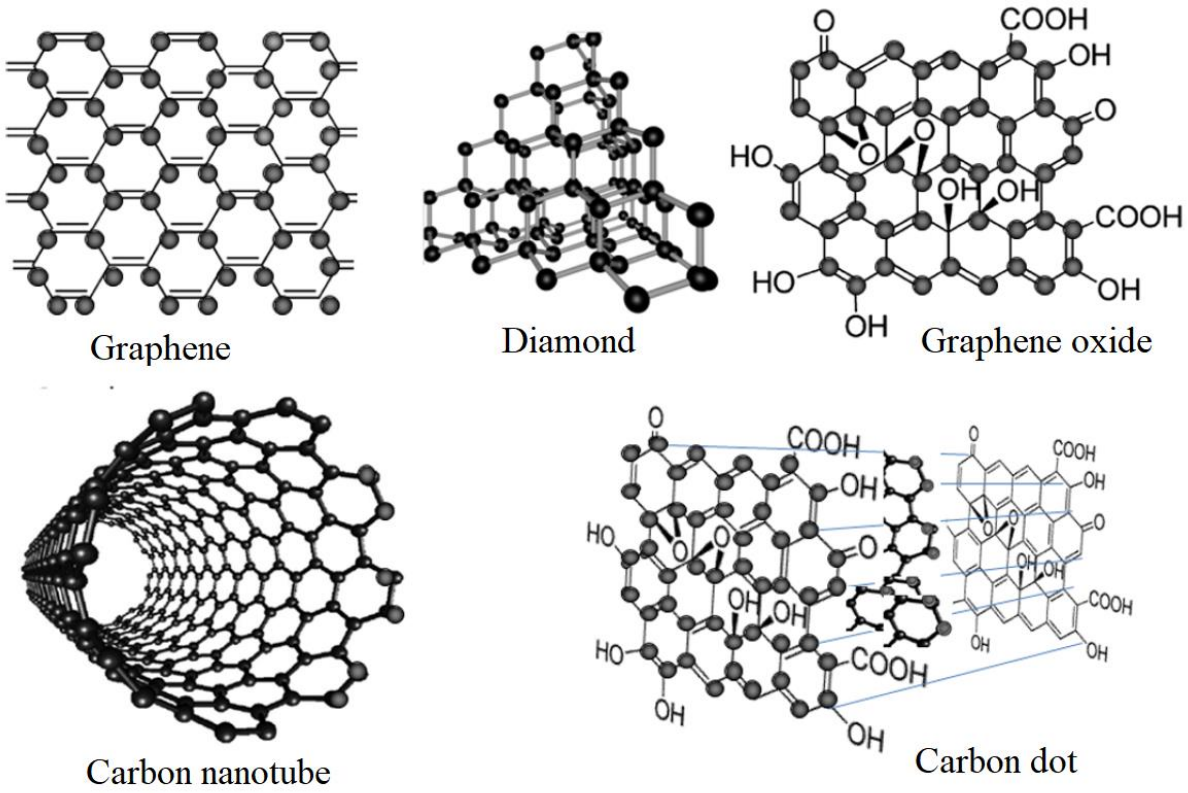

Figure 2.2. The schematic structures of carbon nanomaterials: Graphene, Diamond, Graphene oxide, Carbon nanotube, and Carbon quantum dot. Reproduced with permission from ref. [102].

2.1 Graphene

Graphene is a single layer (monolayer) of graphite, a two-dimensional (2D) material consisting of carbon atoms that are tightly bound in a hexagonal honeycomb lattice. Graphene is the thinnest compound discovered at one atom thickness, the lightest material known, the strongest compound revealed, the best heat conductor at room temperature, and also the best conductor of electricity [101]. The first theoretical research on graphene began already in 1947 [103]. However, the first time graphene was isolated from a highly oriented pyrolytic graphite was in 2004 by Kostya Novoselov and Andre Geim [104]. This was also the first time when existing theoretical descriptions of its composition, structure and properties were confirmed and characterized experimentally. The two scientists finally received a Nobel prize in 2010 for this discovery. After that moment, the explosion in the material science industry started. Due to its unique properties, graphene has been explored in many different fields such as electronic industry, solar cells, light-emitting diodes (LED), touch panels, photovoltaics, energy storage etc. [105–108]. Recently, biomedical researchers started exploiting graphene and graphene-based materials for application in biomaterials, biosensors, tissue engineering and regenerative medicine [109–111].

2.1.1 Structure and properties of graphene

Graphene consists of tightly packed pure carbon atoms arranged in a sp^2 hybridized honeycomb lattice (**Fig. 2.1d**). The bonds between carbon atoms in a hexagonal lattice are extremely strong covalent σ bonds, with a distance of only 0.142 nm [104,112]. These bonds are responsible for

graphene's stability and elasticity. However, in literature, graphene also refers to a multi-layered material, in which layers of sp^2-networks are connected with weak van der Waals forces, $\pi - \pi^*$ stacking interactions with an interlayer spacing of 0.335 nm (**Fig. 2.1e**).

Graphene's honeycomb network is the basic building block of other carbon allotropes, such as 3D graphite (hundreds of thousands of individual layers of linked carbon atoms stacked together), 1D nanotubes and nanoribbons, or 0D fullerenes and graphene quantum dots.

Graphene oxide (GO) is a monolayer of graphene containing numerous oxygen functional groups, such as hydroxy, carbonyl, carboxyl and epoxy groups (**Fig. 2.2**). Reduced graphene oxide (rGO) is more defective than graphene, but easier to modify with different functional groups [113].

A very unique property of graphene is the fact that it has a zero bandgap because the conductive and valence bands meet at Dirac points, which is why it is considered as a semimetal [114]. This property is a drawback in terms of using graphene in certain electronic applications (such as FET transistors technology) because it prevents them from switching off. However, it is possible to turn graphene into a semiconductor by certain modifications. Opening a bandgap is possible by breaking lateral symmetry of graphene sheets by different chemical or structural modifications. For example, if some carbon atoms in the hexagonal structure are replaced by other atoms (e.g. nitrogen), the symmetry of the lattice breaks, and the gap between π - $\pi^*$is formed [114].

Theoretical predictions about the remarkable electronic properties of graphene were confirmed by the experiments many years later. The mobility of the charge carriers in graphene is very high, up to 150 000 cm^2/Vs. Therefore, it is often said that graphene electrons act very much like photons in their mobility, due to the lack of mass [101]. However, the quality of graphene and the substrate that is used, are limiting factors (with silicon dioxide as the substrate, for example, mobility is potentially limited to 40000 cm^2/Vs [101].

Another beneficial characteristic of graphene is its elastic properties. Atomic force microscopy tests conducted on graphene sheets revealed that the sheets with a thickness of 2-8 nm had spring constants from 1-5 N/m and Young's modulus of 0.5 TPa [115]. However, graphene used in these studies was flawless, which is difficult to reproduce, but anyway confirms great elasticity of graphene. Besides being very subtle and flexible material, graphene is the strongest material ever observed due to the very dense network of sp^2 bonds [116].

Optical properties of graphene are also very unique. Firstly, it is transparent, and secondly, a single layer can absorb 2.3% of white light, and adding another layer increases this number by approximately the same value [117]. This feature provides graphene potential application in the field of optical electronics.

Thermal properties of graphene are also remarkable, with the thermal conductivity up to 5000 W/mK at room temperature, which is 20 times higher than copper [118]. This quality makes graphene suitable for application in microelectronics.

2.1.2 Preparation of graphene

Graphene fabrication methods can be divided into top-down and bottom-up approaches. In top-down methods, bulk graphite is used as a starting material, which is exfoliated to single or few-layered graphene. In the bottom-up method, graphene is obtained from smaller carbon sources and includes epitaxial growth on SiC or chemical vapor deposition (**Fig. 2.3**).

Top-down approaches:

- Mechanical exfoliation of graphite

Mechanical exfoliation, known as a "scotch-tape method" was used by Novoselov and Geim when they isolated graphene for the first time. In this method, a single graphene sheet can be separated from the crystalline graphite through the attachment to an adhesive tape [104]. This method is perfect for characterizing physical properties of graphene, because the obtained sheets are micrometer-sized and without defects. However, it is not easy to control the number of layers and the production yield is very low, so it is not a suitable method when it comes to biomedical application of graphene where larger quantities are necessary.

- Chemical oxidation of graphite to graphite oxide

Chemical oxidation of graphite is the most widely used technique, which allows the large-scale production of graphene. In this method, graphite is chemically oxidized to graphite oxide, which is later exfoliated by sonication to graphene oxide (GO), and finally reduced in order to remove oxygen-containing functional groups. The most used oxidation method today, was presented by Hummers in 1958 [119], and it involves the use of sulfuric acid (H_2SO_4) and potassium permanganate ($KMnO_4$) in which graphite is soaked in order to produce graphite oxide.

After the oxidation of graphite, the sonication and stirring are applied to graphite oxide in order to separate the layers, and finally, graphene oxide (GO) is formed. The surface of GO is highly oxygenated, bearing hydroxyl, epoxide, diol, and carbonyl functional groups [120]. These oxygen-containing functional groups allow GO to be dispersible in water and in many other organic solvents and also provide an overall negative surface charge of GO. The presence of these functional groups disrupts the π-conjugation, which results in GO becoming an insulator.

Reducing graphene oxide is the next step, which involves removing oxygen-containing functional groups. This process is crucial because it has an impact on the quality of rGO in terms of how close its structure will be to the pristine graphene. There are many different ways of reduction, such as chemical (e.g., hydrazine monohydrate, sodium borohydride, hydroquinone), thermal or photochemical [121–123]. The most widely used is a chemical reduction by hydrazine monohydrate, mostly because it eliminates the majority of the oxygen-containing functional groups and it results in stable rGO aqueous dispersion [124,125]. However, the main disadvantage of this method is the high toxicity of hydrazine monohydrate and the fact that the final rGO has many defects, which significantly reduces its conductivity. For this reason, many green reductants have been researched in the last few years such as vitamin C, amino acids, phytoextracts etc. [126–128].

- Electrochemical exfoliation of graphite

A recently emerged method of graphene production with low cost and high yield is the electrochemical exfoliation of graphite (usually highly oriented pyrolytic graphite - HOPG) [129,130]. In this method, graphite is used as a working electrode in a solution of electrolytes such as ammonium sulphate or tetra-*n*-butylammonium bisulphate. Upon application of an electric potential, these electrolytes intercalate into the graphite layers which further leads to expanding of graphite and separating the layers, finally. The exfoliated graphene sheets are then collected by vacuum filtration and dispersed in organic solvents (i.e. *N, N*-dimethylformamide) forming a stable dispersion. This method results in high-quality single or few-layer graphene sheets (C:O ratio around 25.3, lateral sizes around 5-10 μm) with high yield (around 75%), and it is faster and simpler than other methods [131]. According to some scientists, this is currently the most promising approach for large-scale industrial production and bulk application, such as polymer fillers and energy storage devices, where high charge-carrier mobilities are not substantial [132].

Bottom-up approaches:

- Epitaxial growth

This method requires a suitable substrate such as silicon carbide (SiC). Graphene "grows" on a SiC substrate while heating at very high temperatures (higher than 1300℃) in ultra-high vacuum [133]. The main advantage of epitaxial growth over other techniques is the fact that the obtained graphene layers are already on semiconducting or semi-insulating substrates, which is convenient for application in electronics [134]. However, this advantage can be also a drawback, because there is no perfect method to transfer graphene to other surfaces. Additionally, the price of SiC monocrystal wafers is very high, so it makes the industrial application very limited.

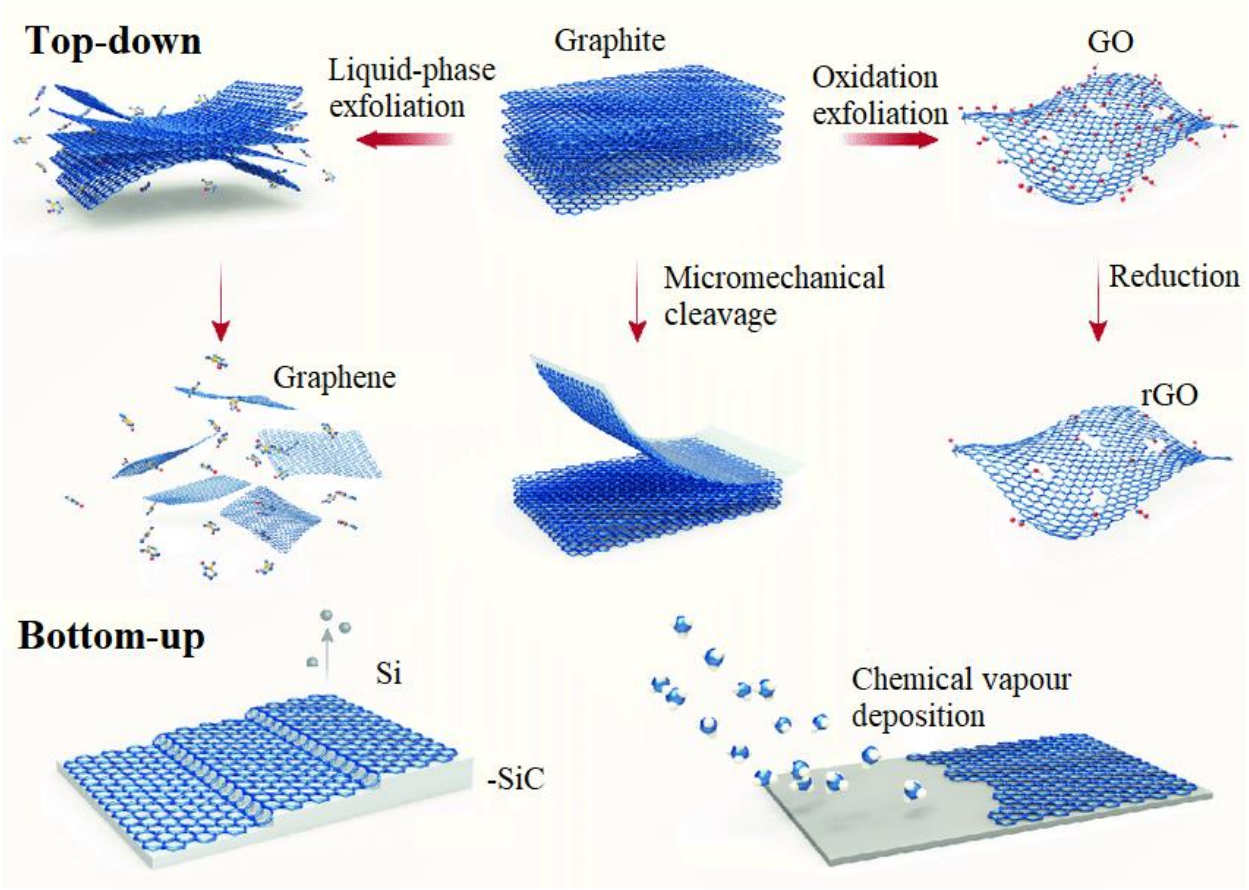

Figure 2.3. Fabrication methods of graphene. Top-down methods which include liquid-phase exfoliation and micromechanical cleavage of graphite. The bottom-up fabrication of graphene is usually performed by means of epitaxial growth on SiC or chemical vapor deposition, typically on Cu using small molecules, such as methane, as precursors. Reproduced from reference [132].

- Chemical Vapor Deposition (CVD) method

Unlike the epitaxially grown graphene, the CVD method allows the transfer of graphene onto different surfaces (gold, Ge) by wet chemical transfer [125,135,136]. The process relies on the use of polymers such as polymethylmethacrylate (PMMA), which is spin-coated on the substrate already coated with graphene. The backside of the graphene can be separated by oxygen plasma treatment from the substrate, before moving the graphene sheets to the new substrate [125].

2.1.3 Application of graphene

As a material with such amazing properties, graphene has consequently numerous applications, some of which are already in use, and some are still in the research stage.

- Optoelectronics

Graphene has a huge potential in optoelectronics, due to its incredible ability to transmit more than 90% of light, and a very low electrical resistance. Additionally, it is highly conductive, so it would work very well in optoelectronic applications such as liquid crystal display (LCD) touchscreens for smartphones, tablet and desktop computers, and televisions [101]. Engineers predict that soon it might replace indium tin oxide (ITO), which is currently the most widely used material for optoelectronic applications. The recent discovery showing that the optical absorption of graphene can be changed by adjusting the Fermi level, as well as its very high tensile strength and flexibility, makes it almost inevitable that it will soon find its application in optical electronics [101].

- Photovoltaic cells

As it was mentioned already, graphene offers a low level of light absorption (around 2.3% of white light) and high electron mobility, which makes it suitable for the manufacture of photovoltaic cells, as an alternative to silicon or ITO. Currently, silicon is most widely used, but when it turns light into electricity it absorbs a photon for every electron produced, which means that a lot of energy is lost as heat [101]. Recent research finds that when graphene absorbs a photon, it produces multiple electrons [137]. Additionally, silicon is able to generate electricity only from the light of a certain wavelength, while graphene is able to work on all the wavelengths. Graphene's flexibility is also very important here because it opens new possibilities of using photovoltaic cells in clothing or curtains that could help power our homes, for example.

- Energy storage

This area of research has been studied a lot, but there is always the same problem: a battery can potentially hold a lot of energy but needs a long time to charge, while a capacitor can be charged very fast, but it cannot hold that much energy [101]. The ideal solution would be to develop the energy storage component such as a supercapacitor or a battery that could have both of the positive characteristics. Graphene is currently studied for a potential application in lithium-ion batteries (as an anode) and as supercapacitors, in order to improve the energy storage capacity and improve the charging rate [138,139]. In the future, graphene-enhanced lithium-ion batteries could be used in much higher energy usage applications, such as electric cars [101].

- Composite materials

Graphene has a great potential in the aircraft industry, because, as we mentioned already, it is a very strong, stiff and extremely light material. It is expected that in the future, a composite material consisted of graphene integrated into plastics could completely replace steel in the aircraft, reducing the weight, and improving fuel efficiency. Due to its electrical conductivity, it could also be used as a coating material which could prevent the damage from the lighting strikes. Graphene coating could also be used as a thermoelectric ice protection system, where the ultra-thin graphene layer could generate heat whenever the current is applied. This could prevent the accumulation of ice on the wings and propellers [140].

- Ultrafiltration

Another fascinating property of graphene is the fact that while it allows water to pass through, it is almost completely impervious to liquids and gases [101]. This opens the possibility of using graphene as an ultrafiltration medium. Recently, a team of researchers has developed a monolayer graphene filter, with pore size of only 3-5 nm (currently used advanced nanoporous membranes with pores of 30-40 nm) [141]. This confirms graphene's great potential in water filtration and desalination systems.

- Biological applications

Graphene has a huge potential in the field of bioengineering, however, there are still some drawbacks that it needs to overcome. Large surface area and high electrical conductivity make it a great candidate for biosensors, which could monitor glucose levels, hemoglobin levels, cholesterol and even DNA sequencing [109]. Additionally, it has potential in the design of antibacterial materials and in tissue engineering [43,111]. However, there is still a lot of research to be done, and more profound *in-vitro* and *in-vivo* studies [142–144].

2.1.4 Antibacterial activity of graphene and graphene-based materials

In the light of the graphene's application as an antibacterial material in the experimental part of this thesis, its interaction with microbes will be discussed more profoundly, and an overview of the new research activities in this direction will be presented.

There are different mechanisms of antibacterial action of graphene-based materials. In the case of the interaction of GO or rGO with bacteria in suspension, the dominant mechanisms are the membrane rupture caused by the direct contact of bacteria with the sharp nanosheets, membrane wrapping and oxidative stress [145–147]. Numerous studies revealed the loss of bacterial cell viability in a concentration and time-dependent manner, with a higher loss of viability of Gram-positive bacteria [125]. Additionally, Liu et al. [148] showed that the antibacterial activity of GO in a suspension is also lateral size-dependent. They proved that larger GO sheets exhibited stronger antibacterial activity because they could more easily cover bacteria cells, and cells could not proliferate once fully covered, which resulted in the cell viability loss. Atomic force microscopy (AFM) images of *E. coli* bacteria covered with GO sheets are presented in **Figure 2.4** (a-c).

However, when it comes to the surfaces coated with GO or rGO, the adhesion of bacteria is a very complex process influenced by many factors. The parameters influencing bacterial adhesion are surface roughness, surface charge, wettability, orientation and size of graphene sheets and surface functionalization [43]. Some of the first studies of bacterial adhesion and interaction with graphene surfaces were published by Akhavan and Ghaderi [149] and Hu et al. [150]. In these investigations, GO nanowells were deposited in a manner that allowed a significant number of edges to be exposed [149]. Therefore, these sheets with extremely sharp edges were able to interact with the bacteria, and physically disrupt the cell membrane, leading to bacterial inactivation. Hu et al. showed that GO significantly suppressed the growth of *E. coli*, leading to viability loss of 98.5%. Transmission electron microscopy (TEM) images confirmed that *E. coli* lost cellular integrity, the cell membrane became destroyed and cytoplasm was flowing out (**Fig. 2.4 d, e**). This was the outcome of the physical disruption of the cell membrane by the GO sharp edges and oxidative stress [150]. Krishnamoorthy et al. demonstrated that graphene nanoflakes had antibacterial activity towards four types of pathogenic bacteria (*E. coli, Salmonella typhimurium, Enterococcus faecalis and Bacillus subtilis*), which was dominantly caused by the formation of ROS [151]. Tu et al. demonstrated that graphene and GO nanosheets can penetrate the cell membrane and induce the degradation of the inner and outer cell membrane of *E.coli* [152]. The wrinkled surface of the GO nanosheet is also favorable for the immobilization of various materials, such as TiO_2 [153] and Ag [154]. Taking into account the antibacterial properties of GO, their large size is very advantageous when used as substrates for

nanocomposites. The GO substrate could prevent the aggregation of nanoparticles and provide enhanced antibacterial activity through synergistic effects. Additionally, the use of GO nanosheets could provide easier recycling of nanocomposites from water, just by using a simple filtration.

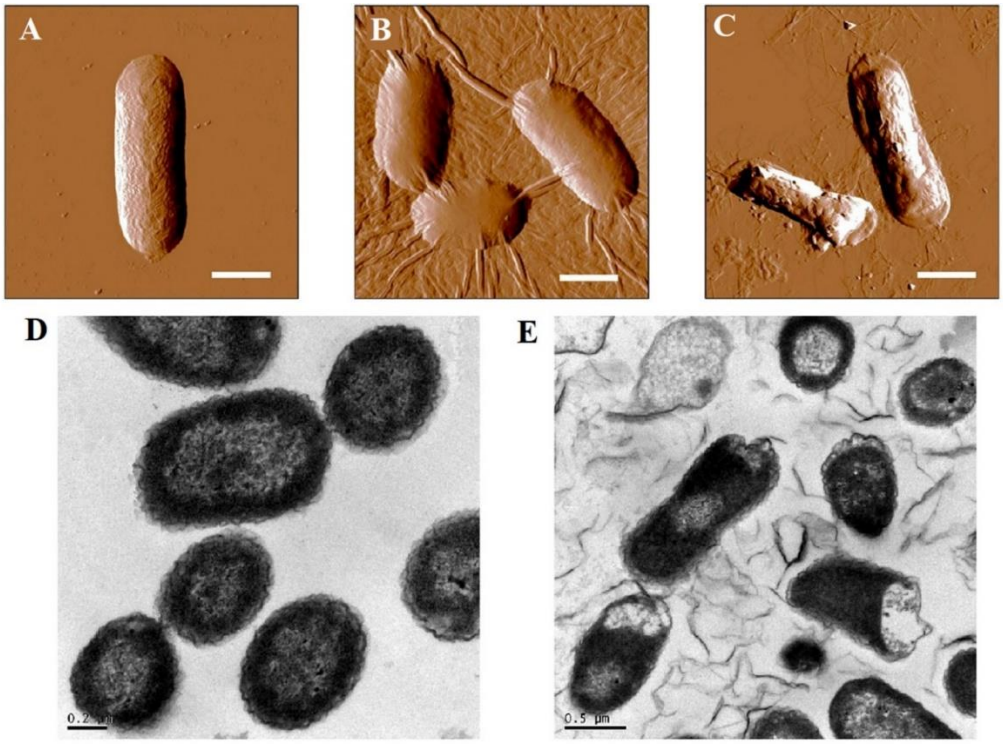

Figure 2.4. AFM image of *E. coli* bacteria after incubation in water (A) and incubation with GO suspension for 2 h (the scale bars are 1µm) (B, C); TEM images of *E. coli* before (D) and after exposure to GO nanosheets for 2 h (E) (reproduced with permission from ref. [148] and ref. [150], respectively).

The antibacterial activity of graphene-based nanomaterials depends on a few crucial factors, such as the size, shape, and surface functional groups. Additionally, the incorporation of graphene into photocatalytic systems can enhance the disinfection rate of semiconductors [155]. Another application of graphene-based materials as an antimicrobial agent is photothermal disinfection. Strong near-infrared absorption ability of rGO nanocomposites can efficiently convert NIR light into heat [43,98], and allow highly efficient photothermal ablation of pathogens [99,156]. Wu and co-workers [157] designed a graphene-based photothermal agent, consisting of magnetic reduced graphene oxide functionalized with glutaraldehyde (MRGOGA), which possesses excellent cross-linking properties with proteins in bacteria and thus was used as a capturing agent for both Gram-positive and Gram-negative bacteria, and subsequent killing of the captured bacteria.

However, apart from many studies that demonstrate the antibacterial activity of graphene, Barbolina et al. [158] pointed out the importance of purity of GO in the antibacterial application. In their work, highly purified and thoroughly washed GO (1 mg mL^{-1}) did not exhibit antibacterial properties towards *E. coli* and *S. aureus*. In contrast, a suspension of insufficiently purified GO exhibited antibacterial properties. During the purification process, the pH of the solution was measured after each washing, and as the pH was increasing to the neutral, the bactericidal effect of GO completely disappeared. After the extensive study, they proved that the antibacterial activity in certain samples was only due to the presence of soluble acidic impurities. The opposed results, such as the one by Barbolina et al. and others [158–162] are important for the research community, because they give insight into new ideas and motivate researchers to conduct more profound studies.

Table 2.1 shows an overview of the mechanisms of antibacterial action of graphene presented in different research papers, together with the results confirming the absence of graphene's antibacterial activity.

Table 2.1. Summary of carbon-based nanomaterials as antibacterial agents.

Material	Size	Toxicity	Antibacterial mechanism	Observations	Ref.
GO	500, 200 and 50 nm	*E. coli:* 90.9%, 51.8%, and 40.1% viability loss, respectively.	Cutting of cell membrane by sharp edges and extraction of lipid molecules.	Good and long-lasting antibacterial activity; no bacteria resistance; Physical damage; However, a tendency to agglomerate is reducing the antimicrobial activity.	[152]
GO	0.753 – 0.01 μm^2	*E. coli:* larger surface, stronger activity.	Trap the bacteria and isolate them.	Larger GO sheets cover bacteria more easily, but after removal of sheets, bacteria can be activated again.	[148]
Comparison of GO coating and suspension	0.01 – 0.65 μm^2	*E. coli:* 27% to 70% viability loss for a coating; In a suspension from 55 to 0.5% viability loss	ROS generation for coating; Cell entrapment in a suspension.	ROS has a long-lasting activity; Cell entrapment method is reversible, bacterial cells could be recovered.	[147]
GO and rGO comparison	From nm to µm lateral dimensions	*E. coli:* 98.5%, and 90 %, respectively;	Cell membrane damage due to direct contact and cutting of cells.	rGO exhibited significantly higher cytotoxicity than GO.	[150]
Electrochemi-cally exfoliated graphene: EHOPG3 and EHOPG12 (depending on the applied voltage of 3 and 12 V)	Average lateral dimensions 23.5 µm for EHOPG3, and 12 µm for EHOPG12	*E. coli* and *S. aureus*: No antibacterial activity in both samples.	Different surface to volume ration did not have any influence on antibacterial activity. Treatment of *S. aureus* with 0.5 mg mL^{-1} of the EHOPG3 had no significant effect on bacterial growth while the same concentration of the EHOPG12 evinced bacteriostatic activity.	Major effect on bacteria was a slight change of bacteria morphology. Membrane remained intact despite significant change of chemical content of membrane components.	[162]
rGO	No data	*E. coli:* 99.9% *S. aureus:* 99.6 % viability loss	Photothermal ablation upon NIR laser irradiation	Can be focused on targeted area; Limited deeper tissue penetration.	[157]

Amino-functionalized GO: with poly(diallyldimethylammoniumchloride) GO-PDDA, and hydrothermal of ammonia solution (AMGO)	No data	*E. coli* ~ 43% for GO; ~ 78 % for GO-PDDA; ~ 98% for AMGO	Positive charge due to amino groups allowed capturing of bacteria, and NIR (808 nm) laser induced photothermal killing.	The higher the number of amino groups, the stronger the antibacterial activity, which was confirmed by zeta potential measurements.	[163]
Graphene treated with fluorine plasma with different durations, 60 and 90 s	No data	*E. coli*	The combined actions of interfacial force and fluorine contribute to good antibacterial activity of partially fluorinated graphene (60 s).	Partially fluorinated graphene (60 s of plasma treatment) exhibited much better antibacterial activity than fluorographene (90 s).	[164]

2.2 Carbon quantum dots - CQDs

Carbon quantum dots are a class of zero-dimensional (0-D) nano carbons, which represent quasi-spherical nanoparticles with sizes below 10 nm and unique properties [165,166]. Their main features are excellent chemical stability, good conductivity, ease of functionalization, strong photoluminescence (PL) emission and optical properties, environmental friendliness, low toxicity and photobleaching resistance [167]. Carbon quantum dots are easy to synthesize with a low cost. The structure and the components of CQDs determine their properties (**Fig. 2.2**). The abundance of carboxyl moieties on the surface of the CQDs provides them a great solubility in water and biocompatibility [165]. Additionally, CQDs are very suitable for surface passivation and chemical modification with several polymeric, inorganic, organic, or biological materials. Surface passivation can significantly enhance physical and fluorescence properties of CQDs [168–170].

CQDs were discovered by chance by Xu et al. in 2004 [171], during single-walled carbon nanotubes (SWCNTs) purification. Since then, extensive studies have been conducted in order to improve the features, synthesis methods and the application of CQDs. The name "carbon quantum dots" was proposed in 2006, by Sun et al. [172] who performed a synthetic route to obtain CQDs with the enhanced fluorescence emission. Similar to other carbon nanomaterials, CQDs can be synthesized by two different approaches: top-down and bottom-up. Compared to conventional semiconductor quantum dots, CQDs have many advantages, including low toxicity, ease of functionalization, tunable fluorescence emission, high stability, solubility in water, etc. Therefore, they have great potential in a wide range of applications, such as bioimaging, drug delivery, photodynamic therapy, photocatalysis, electrocatalysis, chemical sensing. However, there are still some drawbacks that need to be overcome, such as low quantum yield, a complex procedure of purification or functionalization, and sometimes the vagueness of their geometry and structure [165].

2.2.1 Synthesis methods

The top-down approach includes breaking down larger carbon nanostructures, such as graphite [172], nanodiamonds [173], carbon nanotubes [174], carbon soot [175], activated carbon [176], and graphite oxide [177] by different methods (laser ablation, arc discharge, and

electrochemical oxidation). While the bottom-up approach consists of the synthesis of CQDs from molecular precursors, such as citrate [178], carbohydrates [179], and polymer-silica nanocomposites [180] through hydrothermal/solvothermal approach and microwave synthetic routes.

Top-down approaches:

- Arc discharge

The arc discharge is one of the most used methods for the synthesis of carbon nanotubes. In this process, two electrodes are used (usually carbon rods) with the diameter of a few mm. During the purification process of SWCNTs obtained by the arc discharge method, Xu et al. [171] isolated for the first time the unknown fluorescent carbon nanomaterial, which were CQDs. The arc-discharged soot was oxidized with nitric acid, extracted using sodium hydroxide solution, and the black extract suspension was then subjected to gel electrophoresis to obtain CQDs.

- Laser ablation

Sun et al. [172] were the first who synthesized CQDs by laser ablation of a carbon material using argon as a carrier gas in the presence of water vapor. Nanoparticles of carbon were formed in aggregates of different sizes; however, they did not exhibit fluorescence. For this reason, the acid oxidative treatment was performed on the sample, followed by the surface passivation, and the fluorescence was significantly improved.

- Electrochemical oxidation

Zhou and colleagues were the first to describe the electrochemical method of preparation of CQDs [174]. Their experiment included growth of multi-walled carbon nanotubes (MWCNTs) on a carbon paper, which was then inserted into an electrochemical cell that contained degassed acetonitrile with 0.1 M tetrabutyl ammonium perchlorate as a supporting electrolyte [165]. Later, Ming et al. [169] proposed a one-step electrochemical approach using low-cost graphite as a carbon source. This method gave a higher yield of CQDs, without the assistance of any chemicals but pure water.

Bottom-up approaches:

- Hydrothermal/solvothermal method

Hydrothermal carbonization is a low cost, non-toxic and environmentally friendly approach in synthesizing CQDs, from different starting materials. Starting materials can be citric acid [181], polymers like chitosan [182] or polyethyleneimine [183], glucose [184], different fruit and vegetables sources, like orange juice [185], garlic [186]; animal derivatives such as dried shrimp [187], honey [188], etc. In this technique, a solution of an organic precursor is reacted and sealed in a hydrothermal reactor and high temperatures are applied.

- Microwave approach

Microwave irradiation of organic compounds is a rapid and low-cost method to synthesize CQDs [189]. In the work of Zhu et al. [190] as a carbon source, a saccharide (glucose, fructose, etc.) was used, and as a reaction medium, different amounts of polyethylene glycol (PEG-200) were added to distilled water in order to form a transparent solution. The solution was exposed to microwave irradiation (500 W) during 2-10 min. The solution changed color from transparent to yellow (5 min) and dark brown (10 min), which implied the formation of CQDs.

2.2.2 Chemical structure of CQDs

Unlike other carbon materials, CQDs have high fluorescence and solubility in water. For this reason, they have received the attention of many research groups. However, their properties vary together with their structure, a huge number of carboxyl groups on their surface has an important role in their water solubility and biocompatibility [165,191]. Another advantage of CQDs is that they are very convenient for surface passivation and chemical modification with different polymeric, organic, inorganic and biological materials. The synthesis method can affect the properties of CQDs, but what they all have in common is the spherical shape. CQDs consist of smaller carbon nanoparticles with or without crystal lattice [192]. Additionally, the distance between the layers of CQDs is around 0.34nm, which conforms to (002) spacing of the crystalline graphite [191].

2.2.3 Surface modification of CQDs

Surface functionalization is very important for the photoluminescence properties of CQDs [193]. Functionalization affects their ability to interact with other organic molecules, drugs, prokaryotic and eukaryotic cells. However, when it comes to biological applications of CQDs, surface passivation plays an essential role [194]. Different macromolecules can be used for surface passivation of CQDs. The most common cationic macromolecule is polyethyleneimine (PEI), which provides a positive charge to CQDs. This is advantageous when they need to bind to negatively charged cell membranes or proteins, or DNA/RNA [195,196]. Neutral macromolecule that is often in use is polyethylene glycol (PEG). It is convenient because of its biocompatibility and biodegradability [197]. Additionally, the negative and neutral charge of CQDs surfaces are beneficial for therapeutic applications. The reason for this is because negatively charged groups can escape adsorption on proteins (due to electrostatic repulsion), which ensures their widespread circulation in blood, while neutral groups can avoid the immune system clearance [198–200].

Another reason for surface passivation is the protection of CQDs from the contaminants in the environment. CQDs are very sensitive to contaminants, which makes their surfaces easily affected, and changes their optical properties [201]. Surface passivation is usually achieved by the formation of a thin insulating layer, which contains polymeric materials such as oligomeric PEG, and PEG1500N [172]. Researchers have proved that surface passivation is a crucial step in the production of CQDs with high fluorescence (**Fig. 2.5**).

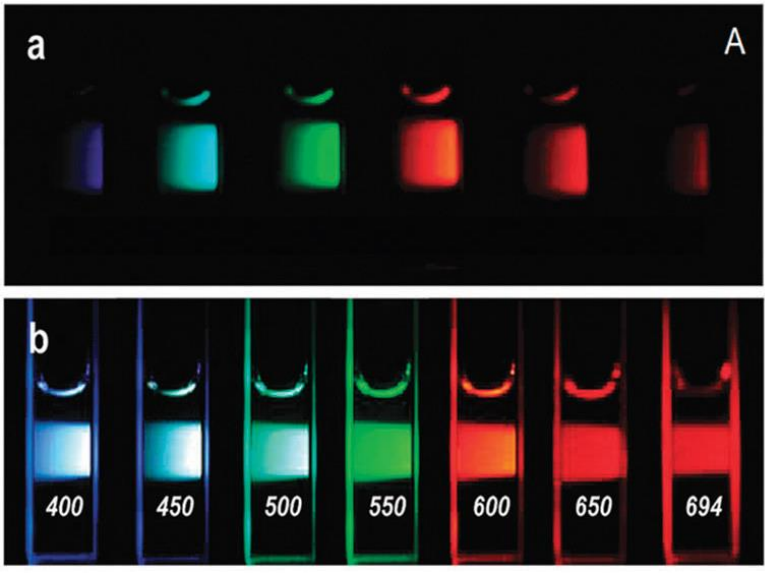

Figure 2.5. Aqueous solutions of PEG1500N-passivated CQDs (a) excited at 400 nm and (b) excited at the indicated wavelengths. Reproduced from ref. [172]

2.2.4 Applications of CQDs

Carbon quantum dots have various applications, such as sensing (biological and chemical), bioimaging, biomedicine (diagnostics, therapy and drug delivery), as antibacterial agents, in photocatalysis and electrocatalysis. Due to their water solubility, biocompatibility, resistance to photobleaching, and superior chemical stability, they have replaced semiconductor quantum dots in many fields.

2.2.4.1 Sensing

In the chemical sensing field, the detection of heavy metals such as Hg^{2+} is very important. Heavy metals are toxic and can be very dangerous for the environment and human health. The first time CQDs were used in chemical sensing was a selective detection of Hg^{2+} in water and live cells [202–204]. Additionally, CQDs were used for the selective detection of Cu^{2+}, Fe^{3+}, Pb^{2+}, Ag^{+}, and usually, the sensing was based on the fluorescence quenching by the metal ions [165]. Biosensing is another aspect of sensing application of CQDs, which exploits their photoluminescence. Posthuma-Trumpie et al. [205] showed the sensitivity at a picomolar range of CQDs. Moreover, apart from higher sensitivity, they are cheaper than gold or latex, easier to prepare and very stable. In the work of Li et al., CQDs were used for the detection of nucleic acids, where sensitivity was so high, that even a single-base mismatch could be identified [206]. Also, CQDs could be applied for the detection of dopamine [207], ascorbic acid [208] and glucose [209].

2.2.4.2 Bioimaging

When it comes to bioimaging, apart from photoluminescence, the most important property of CQDs is their biocompatibility, which makes them suitable for both *in vitro* and *in vivo* visualization. However, even though CQDs themselves are not toxic, different surface passivating agents could be, therefore, for *in vivo* applications only the surface passivating agents with low cytotoxicity could be taken into account [210]. Researchers measured cell viability after the treatment with different amounts of CQDs. It was found that the average cell viability is higher than 95%, at the concentrations up to 1.8 mg mL^{-1}, which confirms that CQDs are much more biocompatible than semiconductor quantum dots [165,167,211]. In the work of Hsu et al. [212], carbon dots derived from the green tea were used for the imaging of MCF-10A, MCF-7 and MDA-MB-231 cells. It was demonstrated that the CQDs were mostly localized on the cell membranes and cytoplasm. However, Fowley et al. [213] prepared water-soluble and biocompatible CQDs which were encapsulated in an amphiphilic polymer. These CQDs were found to cross the cell membrane and concentrate in the cytosol. This implies the localization of CQDs in the cells can vary, depending on the surface passivating agents, and mode of passivation.

Another advantageous feature of CQDs that makes them more attractive than other labeling agents is their ability to exhibit multicolor emission. This property allows researchers to choose exactly the excitation and emission wavelength [214]. In **Figure 2.6**, we can see the fluorescence images of cells treated with CQDs, upon excitation with the light of different wavelengths [212]. Achieving the emission in the NIR region is very advantageous. This is because NIR can penetrate the tissue without harming the surrounding cells, therefore, CQDs could be used for *in vivo* fluorescence tracking studies [215]. Yang et al. [215] were the first to report the study in which PEG_{1500N}-passivated CQDs were used as a contrasting agent in live mice. A solution of CQDs was intravenously injected into mice, for the whole-body circulation. However, emissions were detected only in the bladder region. Around 3h after the injection the fluorescence was observed in urine, suggesting that it is the main elimination pathway of intravenously injected CQDs [215]. Their results demonstrated that CQDs injected into mice in different ways retain strong fluorescence *in vivo*. Taking into account the biocompatibility and nontoxicity of CQDs, this study confirmed the great potential of CQDs for bioimaging, which was later confirmed by other research groups [216–218]. However, before moving to human studies, there is still an urge to define the ideal passivating

agent and an optimal concentration of CQDs in cell cultures and animals, particularly apropos long-term effects.

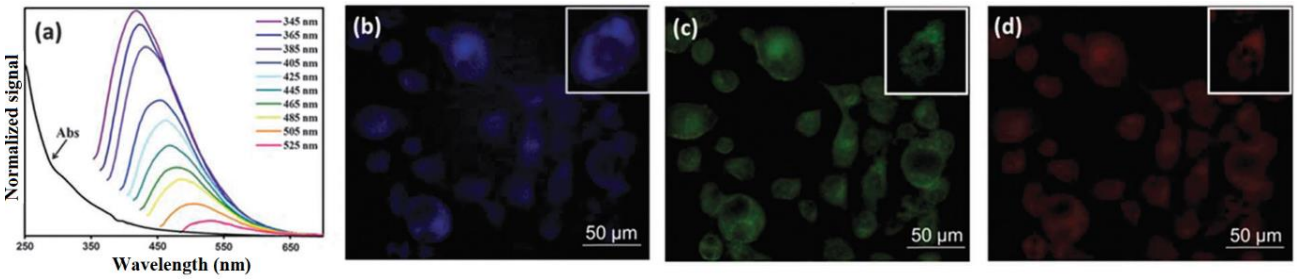

Figure 2.6. a) Emission spectra of CQDs at different excitation wavelengths; fluorescence images of MCF-10A cells treated with CQDs upon excitation with a) UV; c) blue and d) green light. Reproduced from ref. [212].

2.2.4.3 Nanomedicine

- Diagnostics

Carbon quantum dots have great potential in diagnostics. Semiconductor quantum dots have been used for *in vivo* diagnostics of various diseases. However, since CQDs have proved to have lower toxicity than traditional semiconductor QDs, they became the preferred choice for *in vivo* labeling [218]. Recently, Li et al. [219] developed a new chemical method for the early detection of colorectal cancer. They used CQDs which were functionalized with -COCl and formed Cl-CQDs. Cl-CQDs were then conjugated with anti-desmin, in order to detect protein desmin. Desmin is found in high concentrations on the serum of colorectal cancer patients [219]. Since the detection limit was below 1ng/mL, this work highlights a promising strategy for the evaluation of colorectal cancer risk with low cost and high sensitivity. Zheng et al. [220] developed a strategy for diagnostics of brain cancer cells. They synthesized a new type of CQDs (CD-Asp) by pyrolysis route, by using D-glucose and L-aspartic acid. These CD-Asp could efficiently target C6 glioma cells without any extra targeting molecules. Additionally, they were biocompatible and exhibited tunable full-color emission. *In vivo* fluorescence images showed much stronger fluorescence in glioma site, than in the normal brain, indicating their precise targeting of glioma tissue [220]. This research points out a potential application of CQDs for creating an intelligent biomedical platform which will integrate diagnostics, targeted delivery, and therapeutic functions. Additionally, many authors have confirmed a great potential of CQDs for the development of low-cost, efficient and sensitive diagnostic nanoprobes and point of care (POC) devices [198]. Anjana et al. have used CQDs for the design of microfluidic paper-stripe for the detection of bilirubin [221]. Kurdekar et al. developed a CQD-based paper immunoassay for rapid detection of HIV-1 p24 antigen, which could enable early diagnostics of HIV infected individuals where nucleic-acid based tests are not practical or attainable [222]. This kind of POC diagnostic device is not only practical and low-cost, but is extremely important because it could provide the accessibility of healthcare in rural areas of developing countries [198].

- Therapy

CQDs are able to generate ROS upon photo-excitation, which makes them great candidates for photodynamic therapy [167,223]. As it was already discussed in the Chapter 1, compared to other conventional cancer and antibacterial therapies, PDT is less invasive, localized, and can be used repeatedly. However, PDT is not completely developed, and scientists are still in the search of perfectly efficient and safe photosensitizers, and this is where CQDs show a huge potential. Juzenas et al. [224] investigated CQDs coated with a poly(propionylethylenimine-*co*-ethylenimine) in a human prostate adenocarcinoma cell lines (Du145 and PC3) *in vitro*. This research proposed that

upon external light irradiation, produced CQDs could generate ROS, which could photodynamically kill cancer cells [198]. The most important advantage of CQDs in photodynamic therapy compared to other PSs is their tunable bandgap and low toxicity. This means that their bandgap could be made smaller so that CQDs could be triggered by the light of longer wavelengths, especially NIR, which is the most desirable wavelength.

Additionally, CQDs have been used in radiotherapy. In the work of Tao et al. [218], PEG-coated CQDs were functionalized with silver, and used as a radiosensitizer in cancer cells, *in vitro*. These CQDs could selectively enter cancer cells, without showing cytotoxicity towards healthy cells. Upon irradiation by X rays, they produced ROS and destroyed the membrane of cancer cells.

- Drug and gene delivery

Conventional methods of treating cancer could be improved by the targeted delivery of drugs, which could improve their efficacy and reduce the side effects. CQDs have been considered as very promising targeting agents, due to their ease of functionalization and biocompatibility. Additionally, due to their strong photoluminescence, CQDs exhibited dual functionality, as bio-imaging and drug delivery agents, with minimal cytotoxicity. Wang et al. [225] prepared hollow luminescent CQDs which were used as a vehicle for the drug doxorubicin. They exhibited pH-controlled release in a tumor microenvironment, fast uptake, and no cytotoxicity effects. In this work, they exhibited potential for both, cell imaging and drug delivery applications. Treating brain diseases, such as brain tumor and neurodegenerative disorders is very challenging. CQDs have a potential in this field because they could be functionalized with brain penetrating peptides (such as RGERPPR), which allows them to penetrate tumor vascular wall, and target tumor cells [226]. Additionally, CQDs have been used for gene delivery. Liu et al. [214] synthesized CQDs with PEI, which brought a positive charge on their surfaces. The presence of PEI facilitated the electrostatic interactions with negatively charged DNA.

Although CQDs have remarkable properties and potential for many applications, there are still some issues that need to be overcome. Firstly, it is difficult to synthesize CQDs with uniform sizes, and the size has a great influence on their properties. Secondly, CQDs obtained from different batches often show different sizes, quantum yield or PL properties. This issue prevents their commercialization. And thirdly, the application of CQDs in the field of biomedicine still needs more profound *in vivo* studies.

2.2.4.4 Carbon quantum dots as antibacterial agents

The mechanism of antibacterial action of CQDs is their interaction with the bacterial cell wall and more importantly, the production of ROS when irradiated by visible light. It depends on their size, surface charge, functional groups etc. Bing et al. [227] explored the antibacterial activity of carbon dots with different surface charges. Their results showed that positively and negatively charged CQDs had a bactericidal effect on *E. coli*, while uncharged dots had no effect. Their results demonstrated that bacterial cell death by CQDs was followed by DNA fragmentation, chromosomal condensation, extracellular exposure of PS, and loss of structural integrity [227], suggesting that *E. coli* possessed the biochemical mechanism which supported their own termination, once the cell death had been triggered by CQDs. Travlou et al. [228] compared the antibacterial activity of sulfur-doped S-CQDs and nitrogen-doped N-CQDs. Their results proved that N-CQDs exhibited much higher antibacterial efficiency, which was connected to their positively charged amine and amide groups, and to the formation of ROS. However, S-doped CQDs exhibited much lower antibacterial activity. They were mostly negatively charged, due to the dissociation of sulfonic/carboxylic groups and sulfates, and exhibited size-dependent rather than surface charge-dependent inhibition of growth of Gram-positive bacteria. Meziani et al. reported very good antibacterial properties of CQDs, due to the high ROS production under visible light illumination; additionally, the inhibition effect was

observed even under ambient light conditions [229]. Li et al. investigated the antibacterial activity of spermidine-capped fluorescent CQD (Spd-CQDs) toward *E. coli, S. aureus, B. subtilis* and *P. aeruginosa* strains and also against MRSA. They proved very promising antibacterial characteristics and high biocompatibility of Spd-CQDs [230]. Apart from having an antibacterial effect in the solution, CQDs can be used as fillers in antibacterial nanocomposite membranes [231]. **Table 2.2** displays an overview of some of the present research concerning CQDs as antibacterial agents, both in colloid form, or as fillers of nanocomposites.

Table 2.2 CQDs as antibacterial agents

Material	Toxicity	Antibacterial mechanism	Observations	Ref.
Positively charged (spermine – SC-dots), negatively charged (candle-soot – CC-dots), and uncharged glucose GC-dots	*E. coli* activity after treatment with: GC-dots: 100%, CC-dots ~80% SC-dots ~15%	ROS production was the major factor of inhibiting bacterial growth. Moreover, positively charged SC-dots could disrupt cytoplasmic membrane.	CC-dots exhibited the bacteriostatic ability toward *E. coli*, and SC-dots exhibited the bactericidal activity, while GC-dots treatment had almost no effect.	[227]
CQD-EDA	*E. coli:* around 95% viability loss in the light conditions after 6 h	ROS production	The dots were highly effective in bacteria killing under visible light illumination; the inhibition effect was observed even under ambient room lighting conditions.	[229]
Graphene quantum dots - GQDs	*E. coli:* 80 % MRSA: 90 % viability loss;	ROS production under the blue light exposure (470 nm).	Fast antibacterial action, after only 15 min of exposure.	[232]
Comparison of GO, GQD, CQDCA and CQDNH	*E. coli, E. aerogenes, P. aeruginosa, Klebsiella pneumoniae, Bacillus subtilis* For GO: MIC in the range of 500–4000 µg/mL For all the tested quantum dots: MIC: 3.905 – 250 µg/mL	Singlet oxygen formation under blue light for all the samples except GO.	Compared to other tested nanoparticles, GO has a poor antibacterial activity. The effects of the GQD and CQDCA on these bacteria strains are very effective. N-CQDs have shown the best antibacterial properties	[45]
Polyacrylonitrile (PAN) nanofibers containing different concentrations of CQDs.	99.99+%, 6log units inactivation for all strains*: E. coli B. subtilis Pseudomonas aeruginosa;* And more modest inactivation for *S. aureus*: (98.3%, 1.8log units)	Singlet oxygen production by CQDs upon illumination with visible light (420 nm).	PAN nanofibers without CQDs showed no bacterial toxicity effect, as well as both PAN-CQDs-0.6% and PAN-CQDs-2.5% in dark.	[233]

ZnO/CQDs antibacterial coating	*Streptococcus mutans* 96.13%, *S. aureus* 90.28% and *E. coli* 92.35%) under natural light	The natural light antibacterial mechanism was explored, which could be ascribed to the up-conversion fluorescence of the CQDs and the interaction between CQDs and ZnO.	CQDs significantly improved the antibacterial activity of the coating. The antibacterial activity of ZnO coating alone against *E. coli*, *S. mutans* and *S. aureus* was 57.14%, 45.31%, and 42.4% respectively.	[234]
Hydrophobic CQDs-polydimethylsiloxane nanocomposites	Complete eradication (5log units) of *S. aureus* *E. coli* *Klebsiella pneumoniae*, after 15 min of exposure to blue light.	Singlet oxygen production under the blue visible light (470 nm) illumination	BL irradiated polymer serves as a reservoir of singlet oxygen with relatively high lifetime. Large surface roughness of 86.2 nm significantly promoted fast singlet oxygen diffusion to the surface.	[235]
Graphitic carbon nitride quantum dots: g-CNQDs	Inhibition of ~99% of *E. coli* and ~90% of *S. aureus* at a concentration of 0.1mg/mL.	Superoxide and hydroxy radical formation, under the visible light formation.	The antibacterial activity of g-CNQDs was equivalent to that of the silver nanoparticles.	[236]

Chapter 3. Polymers

A polymer is a large molecule or macromolecule, composed of many repeated chemical subunits called monomers [237]. Polymers can be synthetic and natural, and due to their broad range of properties, they play an essential role in everyday life. They are not limited to monomers of the same chemical composition or molecular weight and structure. Certain natural polymers are composed of one kind of monomer, but the majority of natural and synthetic polymers consist of two or more different types of monomers, and these are called copolymers [237].

Natural polymers such as nucleic acids, amino acids or proteins, are crucial for all living organisms. Solid parts of all plants are also made of polymers, and they include cellulose, lignin, and resins [237]. For example, cellulose is a polysaccharide, a polymer composed of sugar molecules. Wood resins are a simple hydrocarbon, isoprene. Many inorganic polymers also are found in nature, including diamond and graphite, both composed of carbon.

3.1 Synthetic methods

Both synthetic and natural polymers are created *via* polymerization reactions, which include the covalent bonding of many small monomers into chains or networks. Some simple hydrocarbons, such as ethylene can be transformed into a polymer by adding one monomer after another. Polyethylene is composed of many repeating ethylene monomers, up to 10 000 monomers in a long chain [237]. Another type of reaction that happens in polymers' formation, is when one atom of a polymer is replaced by another. For example, if one hydrogen atom in ethylene is replaced by a chlorine atom, vinyl chloride is produced, and further, it polymerizes to polyvinyl chloride (PVC) [237]. During polymerization, some chemical groups can also be lost from each monomer. This happens to the polymerization of polyethylene terephthalate (PET).

Generally, there are two categories of the laboratory methods of polymerization, and those are step-growth and chain-growth polymerization [238]. The main difference between them is that in chain-growth polymerization monomers are added to the chain one at a time, the example for this is polyethylene. In the step-growth polymerization chains of monomers may be combined one with another, and the example for this is polyester. Additionally, there is another approach called plasma polymerization, which does not belong to any of the mentioned two methods [239].

The field of polymer science is truly vast, and there are many families of both synthetic and natural polymers, but here we will mention only the ones that we will use in further experiments, in the formation of carbon nanomaterials/polymer nanocomposites.

3.2 Polyurethane (PU)

Polyurethane (PU) is formed by a linear repetition of organic units joined by urethane (carbamate) links. PU is most commonly formed by reacting di- or tri-isocyanate with polyol. Since they contain two types of monomers, one after the other, they are classified as alternating copolymers [238].

Polyurethanes are employed in making elastomeric fibers known as spandex, in the production of coating bases and surface sealants, hard plastic parts for electronic instruments, durable elastomeric wheels and tires, soft and rigid foams, etc. [237].

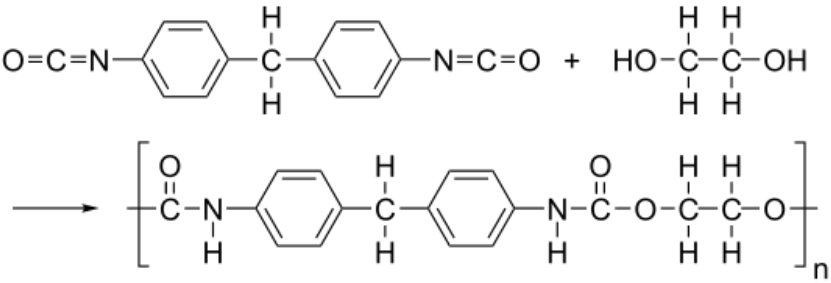

Figure 3.1. Polyurethane synthesis, wherein urethane groups −NH−(C=O)−O− link the molecular units. Reproduced from [240].

3.3 Polyethyleneimine (PEI)

Polyethyleneimine (PEI) is a polymer with a repeating unit composed of an amine group and two carbon aliphatic CH_2CH_2 spacers [241]. Three different forms of PEI have been reported: linear - that contain secondary amines, branched PEIs which contain primary, secondary and tertiary amino groups and finally the dendrimeric, totally branched forms (**Fig. 3.2**) [242]. PEI is produced on an industrial scale and finds many applications usually derived from its polycationic character.

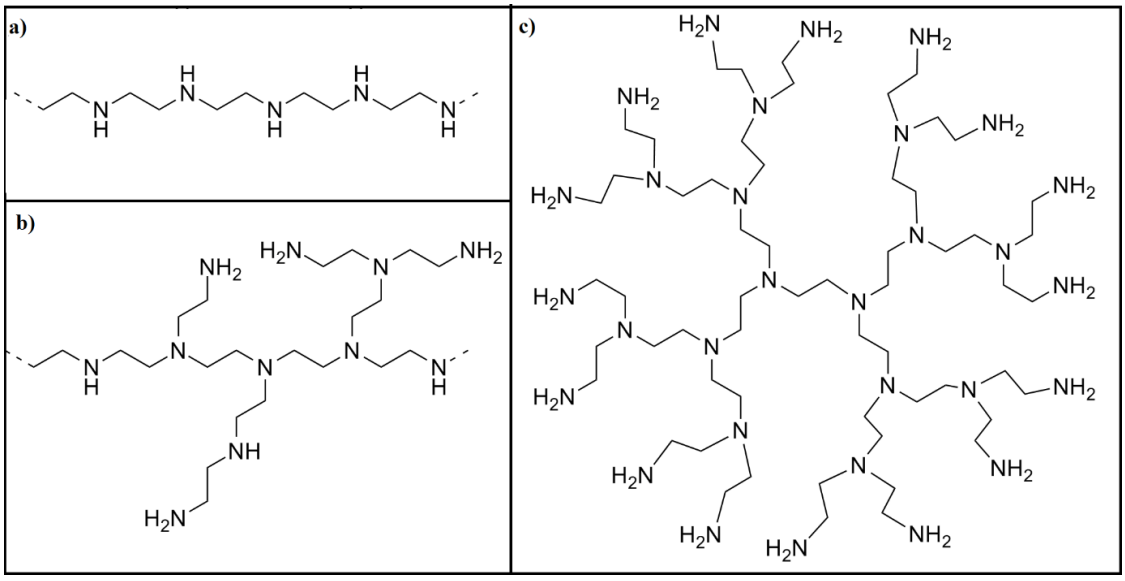

Figure 3.2. a) Linear PEI fragment; b) Typical branched PEI; c) PEI dendrimer generation. Reproduced from [243].

PEI finds many applications in products such as detergents, adhesives, water treatment agents, and cosmetics. It also has an important role in the papermaking process, as a wet-strength agent [244]. In biology, PEI has also various applications, especially in tissue culture and gene delivery [245]. However, in larger quantities, PEI is toxic to cells [246]. There are two mechanisms of PEIs toxicity, the disruption of the cell membrane that leads to necrosis, and the disruption of the mitochondrial membrane, leading to apoptosis. Due to its cationic properties, polyethyleneimine is used in cell culture to help weakly anchoring cells to attach to a plate [247]. PEI is efficient as a permeabilizer of the outer membrane of Gram-negative bacteria [248].

Chapter 4. Gamma radiation

Gamma radiation is a form of electromagnetic radiation of the shortest wavelength and highest photon energy (**Fig. 4.1**) [249]. Such high energy (> 10^5 eV) is sufficient to produce electron disruptions (ionization) in any material that it encounters. In living cells, these disruptions result in damaging the DNA and other cellular structures [250].
Gamma rays were discovered in 1900 by Paul Villard, a French chemist and physicist who detected them while studying radiation emitted by radium.

There are numerous applications of gamma radiation. Firstly, due to its ionizing property, it can destroy microbes, therefore it is used for sterilization of medical devices, food and cosmetics. Also, it is used as a diagnostic tool in nuclear medicine – in imaging techniques, and for cancer treatment by gamma knife surgery. It also has an application in industry, because it allows detection of objects and changes that cannot be seen otherwise (for example internal cracks in airplane wings).

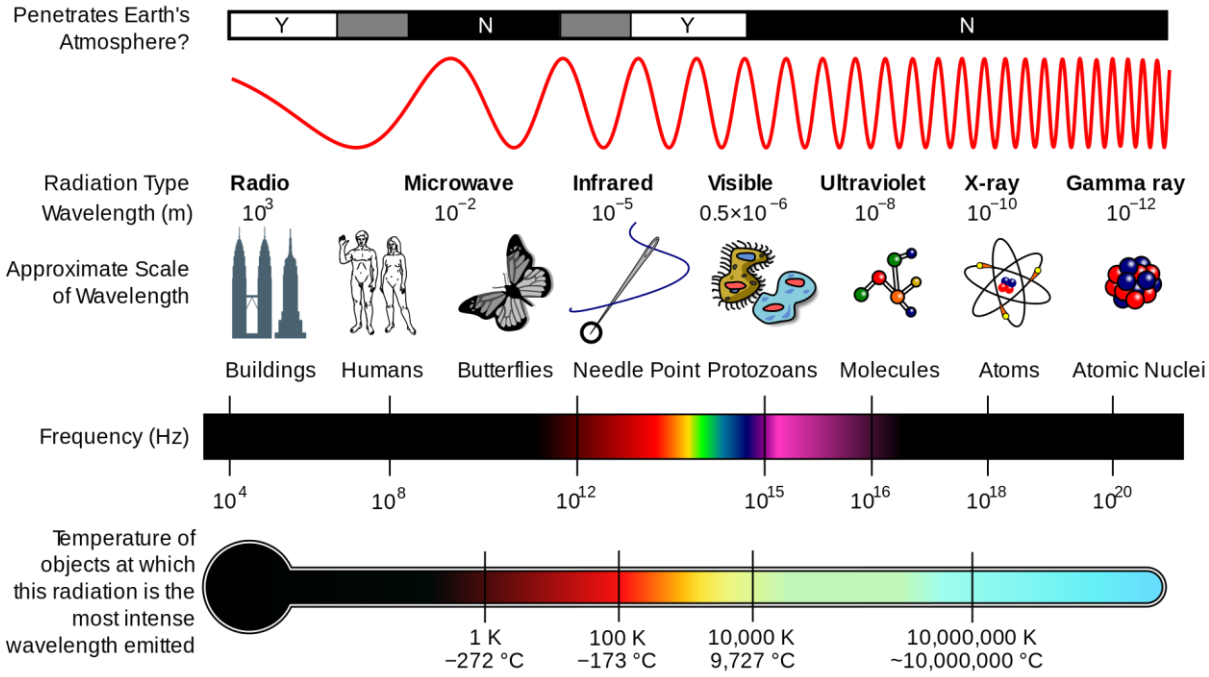

Figure 4.1. Electromagnetic radiation spectrum [251].

4.1 Interaction of gamma rays with matter

When gamma radiation passes through matter, several types of radiation interactions with atoms occur. These interactions are described by the following effects: Compton scattering, photoelectric effect, production of electron-positron pairs, coherent scattering and photonuclear reactions. These effects are responsible for lowering the number of photons and loss of photon energy while passing through the matter.

The photoelectric effect describes the case in which a gamma photon transfers all the energy to an electron, usually from an inner shell. Photons are absorbed by the atom and the electrons are ejected (**Fig. 4.2a**). The photoelectric effect cannot occur if the electron binding energy is greater than

photon energy. This is the dominant energy transfer mechanism for low-energy gamma-ray photons (energies < 50 keV) [252].

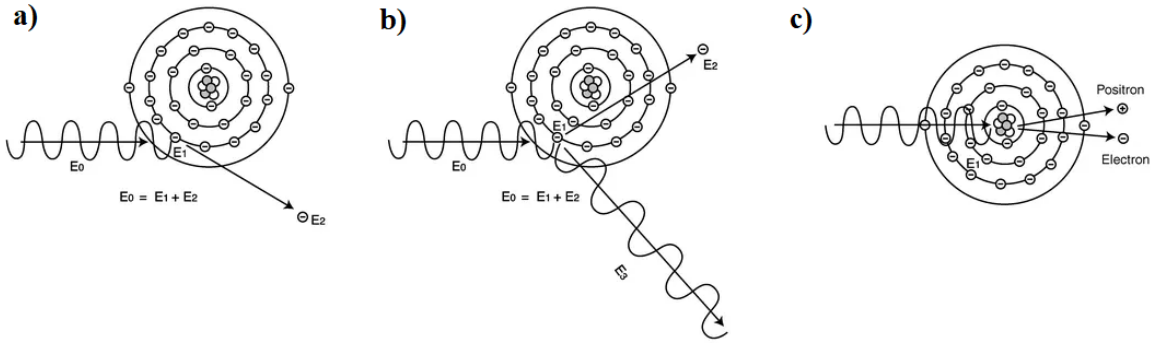

Figure 4.2 a) Photoelectric effect; b) Compton scattering; c) Pair production. Reproduced from [253].

Compton scattering is an inelastic scattering in which the incident gamma photon interacts with an outer electron in the atom. In this process, photon is scattered, while electron, which received enough energy from the photon, is leaving the atom (**Fig. 4.2b**). Compton scattering happens when photon energy is significantly higher than the binding energy of an electron. This is the main absorption mechanism for gamma rays in the intermediate energy range from 100 keV to 10 MeV [252].

Pair production occurs when a gamma photon of very high energy (>1.02 MeV) interacts with the electric field of the nucleus [252]. The energy of the incident photon is converted into the mass of an electron-positron pair (**Fig. 4.2c**).

Probability that one of the three interactions happens, depends on photon energy and the atomic number of the material (Z). The energy absorbed by the material during irradiation is expressed by the absorbed dose which has the unit of gray (Gy). Gray is defined as an energy of one joule imparted per kilogram of matter (1 Gy = 1 J/kg = 1 m^2/s^2).

4.2 Effects of gamma irradiation on different materials

Gamma-irradiation causes ionization of fluids and gases that generally takes place through a series of complex free-radical reactions. Due to the high penetrating power of gamma rays and the exceptional reactivity of free radicals, gamma irradiation is a useful method of chemical modification of various materials. By using gamma rays, it is possible to make changes in the chemical structure of different compounds, avoiding numerous chemical reactions that take time and require significant consumption of reagents and organic solvents.

During interactions of high-energy photons and different materials such as polymers or carbon nanomaterials, many complex processes occur, such as structural modifications (oxidation, reduction, cutting), bond breaking, free radical formation, crosslinking, chain scissions, etc. [254]. Gamma irradiation can cause a reduction of organic compounds (such as dioxin [255]) or even metals. Satoshi et al. performed the synthesis of composite gold/iron-oxide nanoparticles by gamma irradiation [256]. Another interesting example is the removal of lead from aqueous solution by gamma-irradiation [257]. It is also used for functionalization of materials in order to avoid the use of aggressive or toxic chemicals. Wu et al. reported an easy strategy of using gamma irradiation to functionalize multiwalled

carbon nanotubes in a single step [258]. They decorated MWCNTs with Ag nanoparticles relying on covalently bonded polymers. They simultaneously performed one-step covalent grafting of the polymer on a surface of MWCNTs and a reduction of Ag^+ ions to Ag, which were then efficiently anchored on MWCNTs.

Gamma irradiation can cause modification of polymers, by polymerizing monomers, an example of this being glucose polymerization [259]. Also, radiation processing offers a clean and additive-free method for the preparation of novel materials based on renewable, non-toxic, and biodegradable natural polymers [260]. Natural polysaccharides, for example, could be either degraded or cross-linked by radiation, depending on the irradiation conditions. Cross-linked natural polymers can be used as hydrogel wound dressings, face cleaning cosmetic masks, adsorbents of toxins, and non-bedsore mats; while low molecular weight products show antibiotic, antioxidant, and plant-growth promoting properties [260].

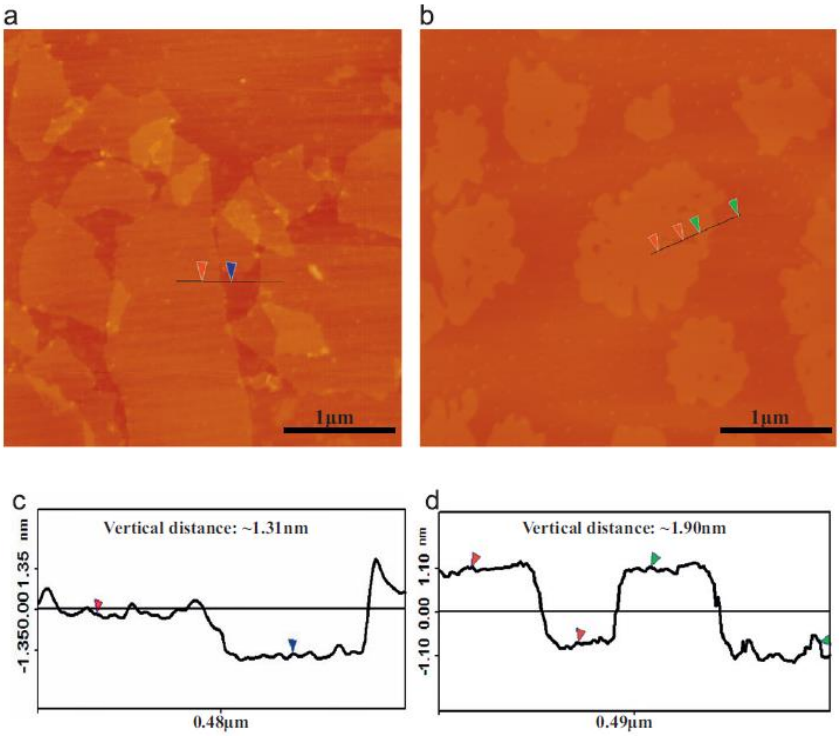

Figure 4.3. (a and c) AFM topographic images and height profiles of graphene from the sonicated GO; (b and d) AFM topographic images and height profiles of graphene from the irradiated GO. Reproduced from [261].

Gamma irradiation significantly affects carbon nanomaterials. Ansón-Casaos et al. explored its effect on the structure and composition of fully oxidized graphene oxide and graphene nanoribbons, as well as their reduced forms [262]. Their results showed small variations in graphene sheet stacking and overall chemical composition. By contrast, the significant changes caused by gamma irradiation were detected in carbon lattice, in which the displacement of carbon atoms was confirmed [262]. Generally, gamma irradiation of carbon nanostructures follows two directions. Firstly, carbon nanomaterials are incorporated in polymer matrixes under gamma irradiation, in order to improve the properties of nanocomposites. And secondly, they are used for tuning the physicochemical properties of carbon nanomaterials [262]. For example, in case of using graphene as a nano-filler in a nanocomposite material, it is necessary to improve its interaction with the polymer matrix, which is difficult to achieve due to graphene's sharp edges. Therefore, Zhang et al. presented the use of gamma irradiation to smoothen the edges of graphene [261] (**Fig. 4.3**). The effects of gamma rays on carbon nanomaterials are highly dependent on irradiation conditions, type of material and the surrounding medium. Many examples showed different and even contradictory results after

applying irradiation under different conditions [263]. For example, the specific surface area of activated carbons prepared from lignite increased during irradiation [264]. On the other hand, it decreased for an activated carbon cloth prepared from the viscose rayon [265]. In some reports, gamma irradiation in different liquid media was used for both the reduction of graphene oxide, and the formation of composites. The mechanism of this reaction is based on the formation of a generation of active radicals through the solvent radiolysis. Therefore, GO was reduced during irradiation in ethanol/water and inert atmosphere, while the reduction did not occur in pure water and oxygen atmosphere [266]. Interesting effects were also noticed after gamma irradiation of SWCNTs and MWCNTs [267,268]. A group of researchers showed that the irradiation dose of 100 kGy improved the graphitization of MWCNTs and surface properties, while at the dose of 150 kGy, it induced damage in sp^3 bonds [268]. Tosic et al. introduced a simple method of synthesizing oligographene nanoribbons by gamma irradiation [269]. Recently, our group investigated the influence of gamma-irradiation of graphene quantum dots (GQDs) in two different media, water and isopropyl alcohol [270]. Changing the medium caused a shift in the position of the emission band in photoluminescence spectra. Additionally, it was confirmed that the photoluminescence properties were improved after gamma pre-treatment of GQDs in both media.

From the experimental results of various research groups, it can be concluded that gamma irradiation has a great potential in simple synthesis or in varying the properties of different materials, including polymers and carbon nanomaterials. By using gamma rays, it is possible to improve certain material characteristics, by a simple and environmentally friendly approach. In the experimental part of this thesis, the changes in a nanocomposite of polyurethane and carbon quantum dots caused by gamma irradiation pre-treatment, are presented.

PART II: EXPERIMENTS

Chapter 5: Reduced graphene oxide/ polyethylenimine flexible nanoheaters for efficient capture and photothermal ablation of bacteria and biofilms

In this chapter, a simple and efficient strategy for successful bacteria capture and their subsequent eradication through photothermal killing will be presented. The developed device consists of a flexible nanoheater, comprising a Kapton/Au nanoholes substrate, coated with reduced graphene oxide-polyethyleneimine (K/Au NH/rGO-PEI) thin films. The Au NH plasmonic structure was designed to feature strong absorption in the NIR region, where most of biological matter has limited absorption, while PEI was selected for its strong ability of binding with bacteria through electrostatic interactions. The K/Au NH/rGO-PEI device was demonstrated to capture and eliminate effectively both planktonic Gram-positive *S. aureus* and Gram-negative *E. coli* bacteria after 10 min of NIR (980 nm) irradiation and even more to destroy and eradicate *Staphylococcus epidermidis (S. epidermidis*) biofilms after 30 min irradiation. The developed technique is simple and rather universal with potential applications for extermination of different microorganisms.

5.1 Experimental

5.1.1 Chemicals

Hydrazine monohydrate, absolute ethanol and branched polyethyleneimine (PEI, M_W~25,000) were purchased from Sigma-Aldrich, and used as received. Graphene oxide was purchased from Graphenea. Kapton® HN polyimide foils with a thickness of 125 μm were obtained from DuPont™.

5.1.2 Synthesis of rGO

Reduced graphene oxide, prepared by GO reduction with hydrazine monohydrate [123], was used only as a reference for comparison with rGO-PEI nanocomposite. First, a dispersion of GO in water (3 mg mL^{-1}) was prepared by exfoliation through ultrasonication for 3 h to form a homogeneous brownish solution. Hydrazine monohydrate was added immediately to the GO suspension (1 μL for every 3 mg of GO). Further, the suspension was heated in an oil bath at 80 °C. After 12 h, the reduced GO precipitated out of the solution. The solid material was isolated by filtration over anodisc membrane with a pore size of 0.1 μm and was washed (2-3 times) with water, until the pH was between 6 and 7. After washing, the resulting black powder was collected and dried under vacuum using a mechanical pump.

5.1.3 Preparation of reduced graphene oxide/polyethyleneimine (rGO-PEI) nanocomposite

First, a dispersion of GO in water (2 mg mL^{-1}) was prepared by exfoliation through ultrasonication for 3 h. A dispersion of PEI in water at a concentration of 10 mg mL^{-1} was prepared separately. The aqueous suspensions were mixed in a round bottom flask (1:1 weight ratio), and heated in an oil bath under stirring at 80 °C for 12 h. After 12 h, the color of the suspension changed from brown to dark grey, suggesting that GO was partially reduced by PEI. The obtained suspension was centrifuged for 15 min at 13500 rpm, in order to separate rGO-PEI nanocomposite from supernatant, and then washed several times with deionized water. After drying, the product was re-dispersed in ethanol.

We also prepared rGO-PEI composites with different weight ratios (1/2, 2/1 and 1/1), but 1/1 ratio turned out to have the best stability and dispersibility in ethanol.

5.1.4 Preparation of gold nanoholes modified Kapton (K/Au NH)

Kapton is a polyimide film, which is known for its great thermal conductivity and high flexibility. Kapton foil was cut into pieces (10×10 mm^2) and then cleaned with acetone in an ultrasonic water bath for 30 min, followed with isopropanol for 10 min and then dried under a nitrogen flow. The cleaned Kapton foils were modified with gold nanoholes (K/Au NH). Briefly, a monolayer of 980 nm polystyrene beads was first deposited on the surface of Kapton by self-assembly. To reduce the size of the particles and isolate them, SF_6 and oxygen plasma etching for 11 min was employed (5 mTorr). The samples were coated with 2 nm Ti followed by 40 nm Au at a constant deposition rate of 2 Å s^{-1} using physical vapor deposition. The beads on top of the Kapton were removed by dissolution in chloroform (overnight). The arrays display holes of an average size of 630 nm and center-to-center spacing of 980 nm [271] (**Fig. 5.4** and **Fig. 5.5b**).

5.1.5 Preparation of reduced graphene oxide-polyethyleneimine coated K/Au NH (K/Au NH/rGO-PEI)

K/Au NH foils (10 x 10 mm^2) were cleaned in ethanol in an ultrasonic water bath for 10 min, and then dried under nitrogen flow. The K/Au NH foils were modified with rGO-PEI by drop-casting (50µL, 2 mg mL^{-1}) four times, each time followed by drying at room temperature (**Fig. 5.5b)**.

5.1.6 Measurement of the photothermal effect

Photothermal experiments were performed by using a continuous wave laser (Gbox model, Fournier Medical Solution) with an output light at 980 nm and power density of 2 W cm^{-2} for 10 min. This laser was injected into a 400 µm-core fiber and placed around 3 cm away from the bottom of the wells. Each sample was placed in a well of 12-well plate with 1 mL of deionized water. The temperature changes were captured by an Infrared Camera (Thermovision A40) and treated using ThermaCam Researcher Pro 2.9 software.

5.1.7 Cell culture and cytotoxicity assay

NG108-15 cells were cultured in Dulbecco's Modified Eagle's medium (DMEM, Gibco®) containing 10% fetal-bovine serum (FBS, Gibco®) and 1% penicillin/streptomycin mix (Gibco®) at 37 °C in a 5% CO_2 incubator.

Direct cytotoxicity testing. Cells were seeded onto 1 cm^2 square glass, Kapton and K/Au NH/rGO-PEI matrix. Each well was loaded with approximately 1×10^5 NG108-15 cells in 1 mL of medium and cultured for 24 h.

Indirect cytotoxicity testing. NG108-15 cells were seeded into 96-well plates (5×10^3 cells/100 µL media per well) 24 h before experiment. Then, the medium was replaced with 100 µL of DMEM/10% FBS in which K/Au NH/rGO-PEI matrix was previously immersed for 24 h.

Cytotoxicity assay. The cell viability was assessed by using resazurin cell viability assay. Briefly, for direct cytotoxicity testing, after 24 h of incubation in a 5% CO_2 atmosphere at 37 °C, the medium was aspired and the cells were washed with 500 µL of PBS to remove the dead cell debris. The incubated surfaces were transferred into a new 24-well culture plate containing 500 µL of medium and the cells

were exposed to resazurin solution (11 μg mL^{-1}) in DMEM/10% FBS for 4 h at 37 °C. Afterwards, the fluorescence with excitation/emission at 554/593 nm (18-nm/20-nm bandwidth) was recorded by using a fluorescence microplate reader (BioTeK™ Cytation™ 5 Cell Imaging Multi-Mode Reader). The results were expressed as a percentage compared with controls. Each condition was replicated five times and data are presented as means ± standard deviation. For indirect cytotoxicity testing, the experimental procedure was similar to that of the previous one.

5.1.8 Bacteria culture and preparation

The bacteria used in this study were *S. aureus* and *S. epidermidis* (Gram positive bacteria) and *E. coli* K-12 MG1655 (Gram-negative) pathogenic strain. A single *E. coli* K-12 MG1655, *S. aureus and S. epidermidis* colony from LB/BHI agar plate was inoculated overnight in LB/BHI medium at 37 °C with moderate shaking. The pre-culture was diluted 50–fold and allowed to continue for another 3-4h, until the optical density at 600 nm (OD_{600}) had reached 0.6 – 1. The *E. coli* K-12 MG 1655 and *S. aureus* cells were re-suspended in sterile Milli-Q water and adjusted to the required concentration.

5.1.9 Antibacterial activity of the K/Au NH/rGO-PEI matrix

To assess the antibacterial properties of K/Au NH/rGO-PEI matrix, each substrate was immersed in the bacterial suspension at a concentration of 10^8 cfu mL^{-1} for 2 h at 37 °C. Both the bacteria cell viability and morphological changes in bacteria were investigated. After incubation, 200 μL of 10^3-fold diluted planktonic bacteria were spread onto LB/BHI agar plates and the plates were incubated at 37 °C overnight. Then, the samples were gently rinsed with Milli-Q water to remove the planktonic cells and prepared for scanning electron microscopy (SEM) measurements.

5.1.10 Photothermal antibacterial activity of the K/Au NH/rGO-PEI matrix

The interfaces were transferred to a new 12-well plate and irradiated with the laser set at 980 nm illumination for 10 min at 2 W cm^{-2} laser power density. Following this treatment, both the control and NIR exposed samples were prepared for SEM imaging.

5.1.11 Bacterial biofilm formation

S. epidermidis was grown on BHI agar plate, upon inoculation overnight in BHI broth at 37 °C with moderate shaking (150 rpm). Upon 50-fold dilution, incubation was prolonged until the OD_{600} had reached 0.5 – 1. Then 50 μL of bacteria culture was plated onto each sample and incubated at 37 °C. After 30 min, 1 mL of BHI medium was added to each 24-well microtiter plate and incubated at 37 °C without shaking for up to 30 h. After incubation, all samples were gently washed with Milli-Q water to remove any non-adherent bacteria.

5.1.12 Biofilm destruction by K/Au NH/rGO-PEI matrix under NIR irradiation

The *S. epidermidis* biofilms grown on glass slides (a control) and K/Au NH/rGO-PEI substrates were irradiated with a 980 nm-continuous wave laser for 10, 20 min or 30 min at 2 W cm^{-2} laser power density. The NIR-induced bacterial eradication by the flexible nanoheater was then studied via agar plate counting (for planktonic cells), by the OD600 method, contact plate assay and

SEM measurements (for biofilm). Briefly, the viability of *S. epidermidis* cells detached in aqueous media from the surface (planktonic cells) during the exposure to laser was estimated by comparing the colony forming units for the samples at different irradiation times, with the initial bacterial suspension. Then, the effects of K/Au NH/rGO-PEI substrates after NIR irradiation against *S. epidermidis* cells adherent on the surface (biofilm) were measured by cell growth measurements, performed by their direct contact with the surface of BHI agar plates and by SEM measurements. For OD600 method (based on measuring the absorbance at 600 nm), the samples with the control were transferred into a new 24-well culture plate containing 1 mL of BHI medium and incubated at 37 °C until the OD600 had reached 0.3. The results were expressed as percentage compared with the control. In addition, for each type of the surface, killing efficiency was calculated from visual images of bacterial colonies on BHI agar plates formed after the direct application of test surfaces and incubation at 37 °C for 20 h and from SEM images. Statistical analyses were performed using ImageJ open-source image treatment program. The results were estimated by comparing the colony forming units for the samples with the control.

5.2 Characterization

Contact angle measurements were performed by a remote-computer controlled goniometer system (DIGIDROP by GBX). The contact angle was measured using 2 μL of deionized water. The accuracy is ±2°, and all measurements were performed in ambient atmosphere at room temperature.

Fourier transform infrared (FTIR) spectra were recorded using a ThermoScientific FTIR instrument (Nicolet 8700) in the 650 - 4000 cm^{-1} range at a spectral resolution of 6 cm^{-1}. 1 mg of dried sample was mixed with 200 mg of KBr powder in an agar mortar. The mixture was pressed into a pellet under 7 tons of load for 2-4 min, and the spectrum was recorded immediately. A total of 64 accumulative scans were collected. The signal from a pure KBr pellet was subtracted as a background.

UV-Vis spectroscopic measurements were carried out using a Perkin Elmer Lambda UV/Vis 950 dual-beam spectrophotometer operating at a resolution of 1 nm. The UV-Vis spectra were recorded in quartz cuvettes of 1 cm path length between 200 and 1100 nm.

X-ray photoelectron spectroscopy (XPS) was recorded using ESCALAB 220 XL spectrometer from Vacuum Generators featuring a monochromatic Al Kα X-ray source (1486.6 eV) and a spherical energy analyzer operated in the CAE (constant analyzer energy) mode (CAE = 100 eV for survey spectra and CAE = 40 eV for high-resolution spectra), using the electromagnetic lens mode. The angle between the incident X-rays and the analyzer is 58° and the detection angle of the photoelectrons is 30°.

Raman spectroscopy measurements were performed on a LabRam HR Micro-Raman system (Horiba Jobin Yvon) using a 473-nm laser diode as excitation source. Visible light is focused by a 100× objective. The scattered light is collected by the same objective in backscattering configuration, dispersed by a1800 mm focal length monochromator and detected by a CCD camera.

Scanning Electron Microscopy (SEM) images of pathogens were recorded using a Zeiss Compat Merlin instrument with a secondary electron detector at 2 kV under high vacuum. The biological samples were fixed with 1% glutaraldehyde solution for 30 min in the dark at room temperature. Then the samples were dehydrated in a graded ethanol series of 25%, 50%, 75%, 95% and 100% (v/v) at 10 min intervals, followed by drying using a vacuum desiccator. Each sample was mounted on stubs and sputter-coated with 5 nm platinum layer.

5.3 Results and discussion

5.3.1 Preparation and characterization of reduced graphene oxide-polyethyleneimine (rGO-PEI)

In this study, we took advantage of the cationic properties of PEI along with the various other interactions (hydrogen, aromatic, electrostatic, hydrophobic) that rGO can form with different molecules and biological matter, to design a photothermal heating platform, capable of efficient capturing bacteria and their subsequent killing under NIR irradiation. To this aim, we prepared rGO-PEI nanocomposites at different ratios (1/1, 1/2, 2/1) by heating a mixture of GO and PEI at 80 °C for 12 h. The rGO-PEI composites were dispersed in ethanol by ultrasonication of 1 h at room temperature (**Fig. 5.1**). The 1/1 ratio displayed better dispersibility and stability in ethanol without compromising its photothermal properties. This composite was further characterized in this study to establish its chemical structure.

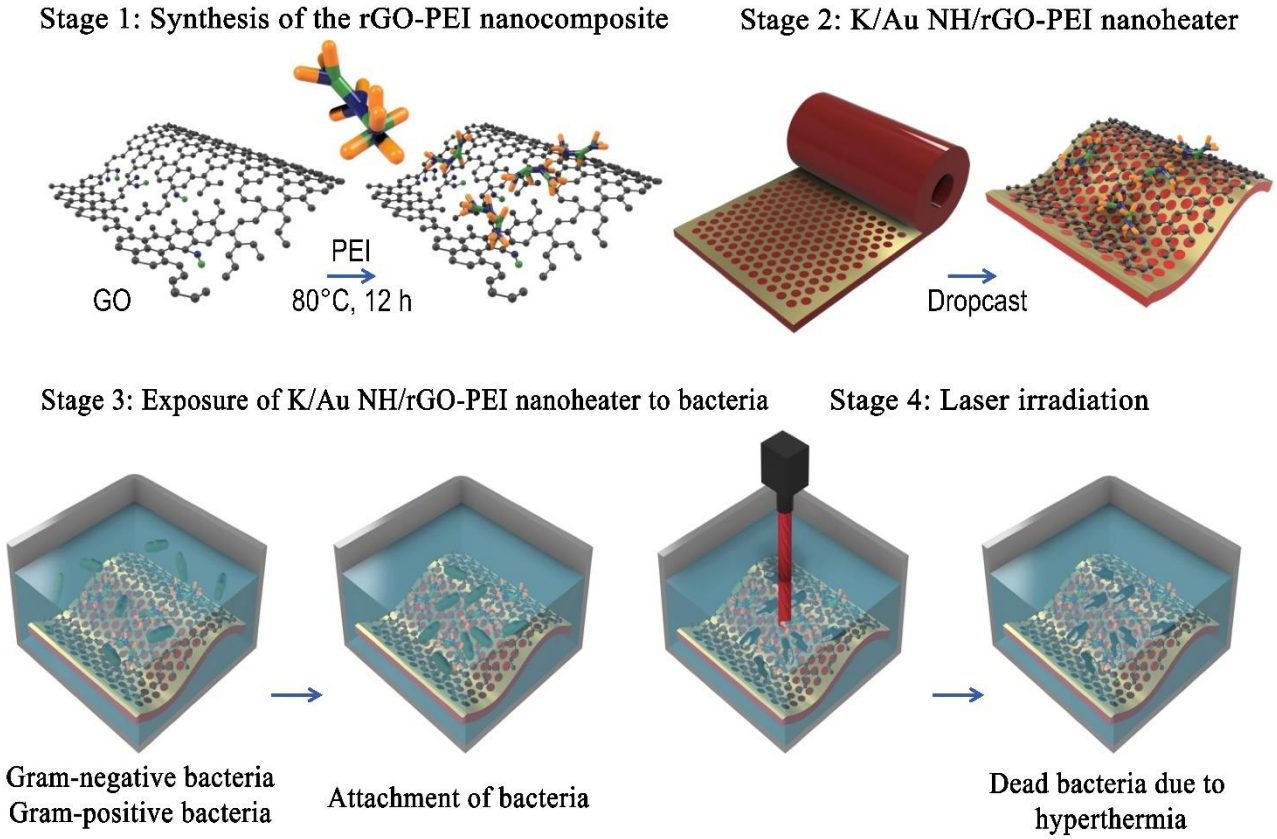

Figure 5.1. A sketch illustrating the formation of reduced graphene oxide-polyethyleneimine coated nanoheaters (K/Au NH/rGO-PEI) and their application in bacteria capture and photothermal killing (Reproduced from [272]).

FTIR is a useful tool to assess the presence of different functional groups in carbon-based nanomaterials (**Fig. 5.2a)**. The FTIR spectrum of GO includes a strong and broad absorption at 3264cm^{-1} attributed to O–H vibration mode, and the C=O stretching mode of COOH groups located at the edges of GO sheets at 1731 cm^{-1}. The peak at 1633 cm^{-1} is attributed to C=C stretching vibration as part of the ring breathing mode in the GO skeleton. The vibration mode at 1422 cm^{-1} is most likely

due to bending vibration of tertiary C–OH groups. The peaks at 1227 and 1057 cm^{-1} are assigned to O-H stretching vibration in carboxylic acid and C-O vibration in epoxy groups, respectively [273]. Compared to GO, the FTIR spectrum of rGO, obtained through hydrazine reduction, shows that most of oxygen-containing groups have disappeared, and C=C stretching vibration was shifted to 1568 cm^{-1}, revealing the higher reduction degree of GO and restoration of sp^2 network.

After reaction with PEI at 80 °C for 12 h, the FTIR spectrum of rGO-PEI clearly contains all the PEI absorption features. The peak at 1731 cm^{-1} completely disappeared, along with obvious weakening of the peak at 1057 cm^{-1} (**Fig. 5.2a**). The strong band at 1666 cm^{-1} in rGO-PEI is related to the formation of amide bonds [274], but could be also due to C=C stretching bonds. This band is a proof that covalent bonds are created between GO and PEI under described experimental conditions, suggesting that PEI was successfully grafted onto rGO nanosheets surface.

The absorption spectra of the prepared rGO-PEI and starting materials were analyzed using UV-vis spectrophotometry in the 200-1000 nm range (**Fig. 5.2b**). PEI absorbs below 230 nm as expected for a polymer without any aromatic structure in its backbone. The UV-vis spectrum of GO exhibits a peak at 237 nm and a shoulder at 290 nm, which can be attributed to π –π* transition due to C=C bonds and n-π* transition due to C=O bonds, respectively. On the contrary, the absorption spectrum of rGO shows a red shifted broad absorption band with a peak at 273 nm after 12 h of reduction with hydrazine. This red-shift is accompanied by an absorption tail at λ>400 nm, indicating that the conjugated structure (sp^2) was restored upon reduction of GO. The red shifted absorption band to 247 nm of rGO-PEI nanocomposite suggests that GO was partially reduced under our experimental conditions. The absorption of the rGO-PEI sample in the NIR region (700-1000 nm) slightly decreased compared to rGO due to the presence of PEI in the sample. However, this decrease in the absorption did not influence its photothermal properties, which were still excellent due to the underlying Au NH layer on Kapton (as discussed later).

Raman spectroscopy is a commonly used technique to provide a structural fingerprint by which molecules can be identified. The Raman spectrum of the rGO-PEI matrix (**Fig. 5.2c**) displays the main features of graphene-based materials with a D-band at 1360 cm^{-1} and a G-band at 1588 cm^{-1} [275]. The *G* peak appears due to the bond stretching of all pairs of sp^2 atoms in both rings and chains. The *D* peak is due to the breathing modes of sp^2 atoms in rings, and it is caused by disordered structure of graphene. The degree of the disorder of the sample can be determined based on the intensity ratio of D and G bands (I_D/I_G) [275]. The I_D/I_G ratio for rGO-PEI was determined to be 1.17, which is smaller than that of rGO obtained upon the reduction with hydrazine (I_D/I_G = 1.22), but higher than that of the initial used GO (I_D/I_G = 1.1). The increase in the I_D/I_G ratio could be ascribed to a decrease in the average size of the sp^2 domains [276].

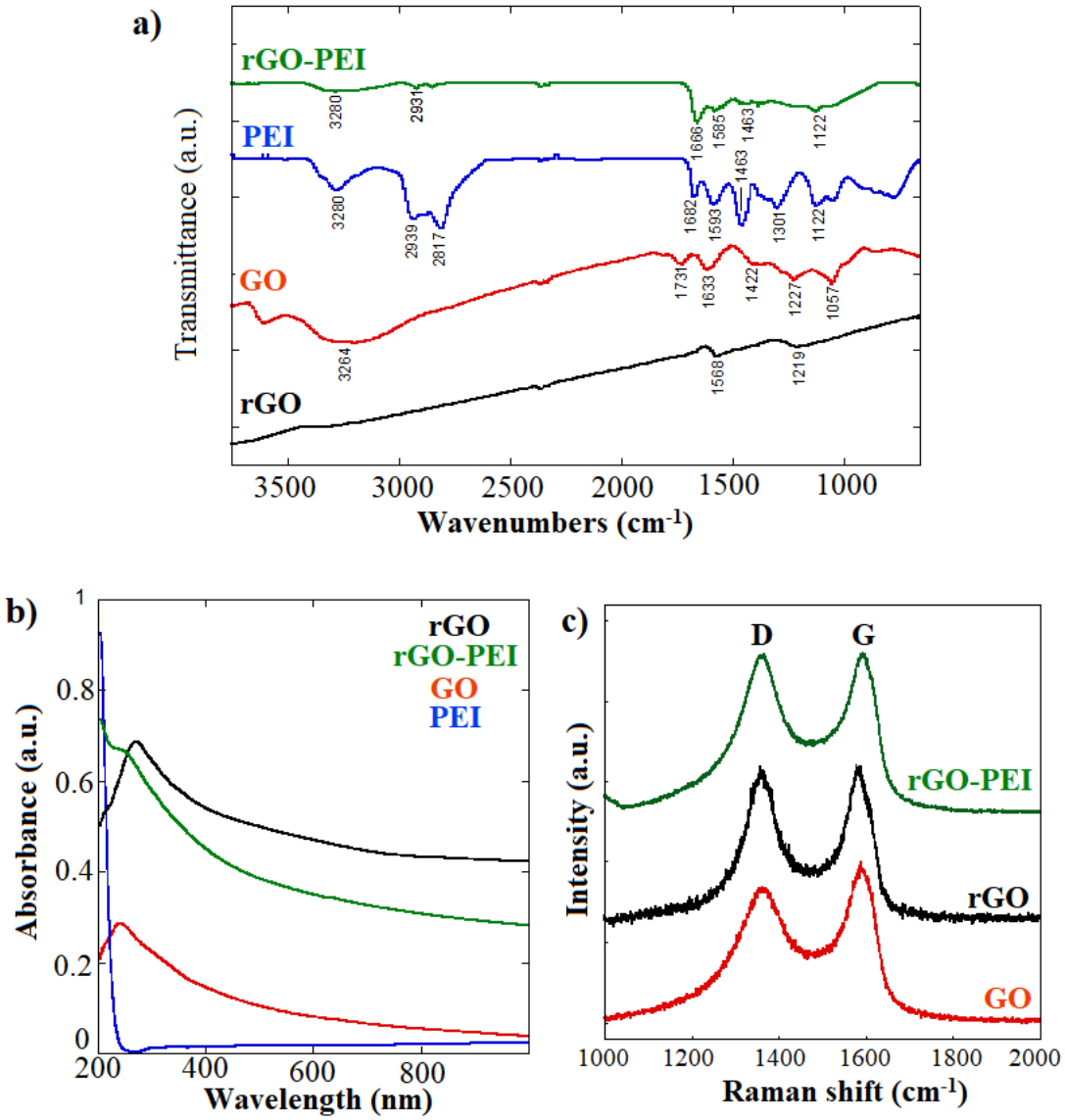

Figure 5.2. a) FTIR spectra of rGO (black), GO (red), PEI (blue) and rGO-PEI (green); b) UV/Vis absorption spectra of PEI (blue), GO (red), rGO-PEI (green) and rGO (black); c) Raman spectra of GO, rGO and rGO-PEI (reproduced from [272]).

XPS analysis was carried out to examine the surface elemental composition of rGO-PEI nanocomposite. The XPS elemental survey spectrum revealed that this nanocomposite was composed of the following elements: C, O, N. This result was confirmed by the specific characteristic signals at 530, 398 and 284 eV, which correspond to O_{1s}, N_{1s} and C_{1s}, respectively (**Fig. 5.3a**). The appearance of N_{1s} peak in the XPS survey spectrum for rGO-PEI indicates that PEI chains were adsorbed or grafted onto the rGO structure.

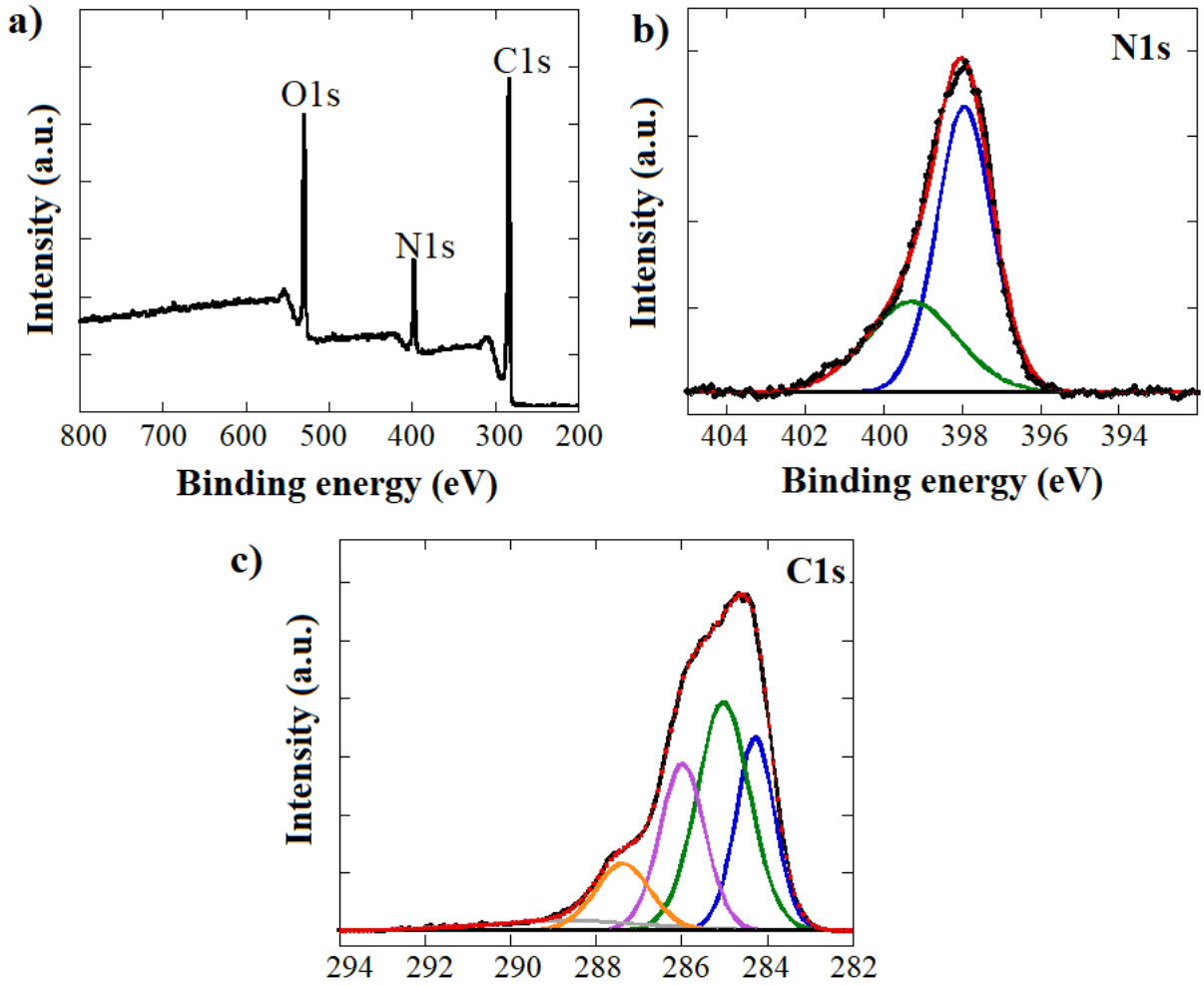

Figure 5.3. XPS analysis of rGO-PEI. Wide scan survey spectrum (a), high resolution spectra of the N_{1s} (b) and C_{1s} (c). Reproduced from [272].

The high resolution XPS spectrum of the N_{1s} (**Fig. 5.3b**) exhibits a dissymmetrical peak that can be fitted with two components at 399.5 and 400.8 eV attributed to -NH_2 and -NH-, respectively [277]. The high resolution spectrum of the C_{1s} (**Fig. 5.3c**) can be decomposed into several bands at 284.2, 285.0, 286.2, 287.4 and 288.8 eV due to Csp^2, C-H/C-C, C-O/C-N, C=O and OH-C=O, respectively, in accordance with the chemical composition of the material.

5.3.2 Preparation and characterization of Kapton/Au nanoholes (K/Au NH)

The development of electronic healthcare devices is made possible by nanostructuring, since no other combined bottom-up and top-down approaches offer so many degrees of freedom that allow man-made systems to fit the small structures of life. Here, we took advantage of colloidal lithography using polystyrene spheres of 980 nm in diameter to create large-area, self-assembled hexagonally-packed monolayers on Kapton substrates. The size of the self-assembled polystyrene beads can be easily tuned by conventional SF_6 and oxygen plasma etching. Then, physical vapor deposition grown electrical layers (40-nm thick Au) complete the devices for the concept of Kapton-based nanoheaters. Finally, upon the removal of polystyrene particles, a required K/Au NH configuration for PTT is obtained. **Figure 5.4a** illustrates representative SEM images of a homogeneous gold nanoholes array with an average diameter of 630±10 nm and a center-to-center spacing of 980 nm. The long-range ordered gold nanohole array supports both propagating and localized surface plasmon resonance

(LSPR) modes, with the hole diameter and periodicity being significant parameters in tuning the interface absorption band [278–282]. The absorption spectrum of the resulting K/Au NH array is between 500-1100 nm with a maximum absorption at around 950 nm (**Fig. 5.4b**). This is the reason we used the laser with the incident excitation wavelength of 980 nm for PTT.

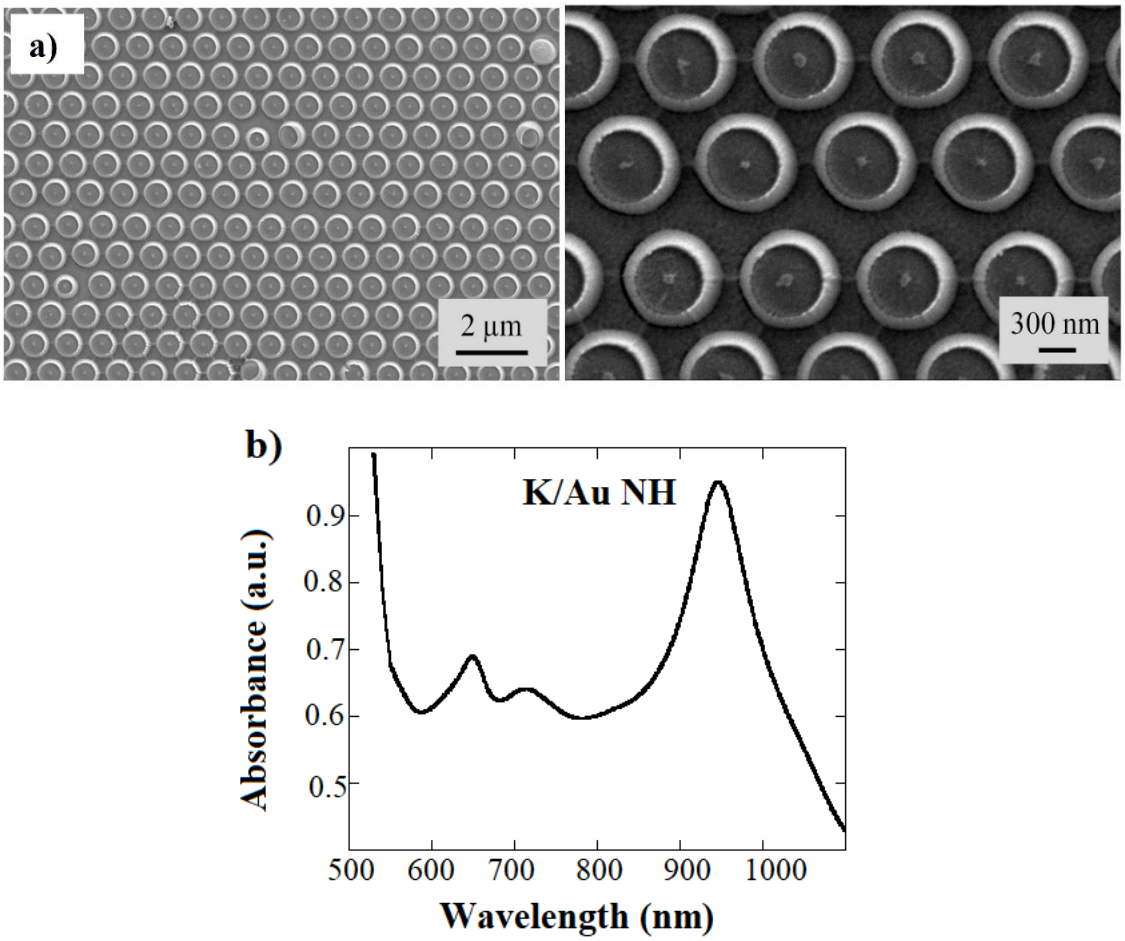

Figure 5.4. a) SEM images at low and high magnifications of K/Au NH formed by using colloidal lithography. b) Typical absorption spectrum for K/Au NH sample (Reproduced from [272]).

5.3.3 Preparation and characterization of reduced graphene oxide-polyethyleneimine coated nanoheaters (K/Au NH/rGO-PEI)

The schematic representation of the preparation of the K/Au NH/rGO-PEI nanoheater is displayed in **Fig. 5.1**. The K/Au NH interface was coated with rGO-PEI by drop casting 4 times 50 µL of an ethanolic solution of rGO-PEI (1/1, 2 mg mL^{-1}) (**stage 2**). The SEM of the K/Au NH/rGO-PEI shows a homogenous coating all over the surface (**Fig. 5.5A**).

The wetting properties of the prepared interfaces were studied by water contact angle (WCA) measurements. As it can be observed from **Figure 5.5C**, Kapton covered with a continuous layer of Au displayed a hydrophilic character with a WCA of 80°. This is very different from the K/Au NH interface, which exhibited a hydrophobic character with a WCA of 105°. The increase of the WCA upon nanohole deposition is most likely connected with an increase of surface roughness. Coating the K/Au NH interface with rGO-PEI led to a decrease of the WCA to 54°, conferring a hydrophilic character to the surface. This property is advantageous as it will enhance the contact between bacteria

and the nanoheater's surface. In the **Fig. 5.5B**, we can also observe a photograph of all the three surfaces: Kapton covered with a continuous layer of Au, K/Au NH interface and the K/Au NH/rGO-PEI, respectively.

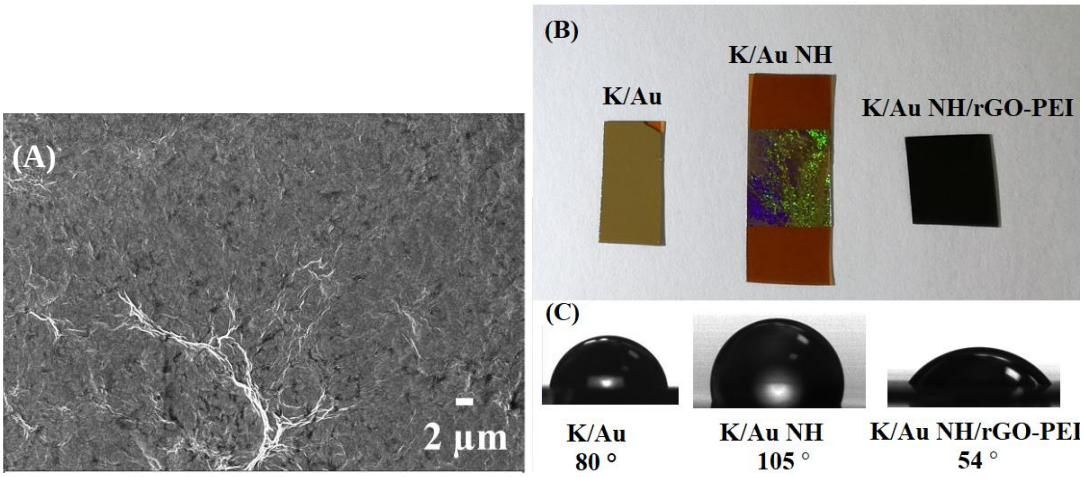

Figure 5.5. (**A)** SEM image of the K/Au NH/rGO-PEI coating; (**B**) a photograph of (a) Kapton covered with a continuous Au film (K/Au), (b) Kapton/Au nanoholes (K/Au NH), (c) Kapton/Au nanoholes coated with rGO-PEI (K/Au NH/rGO-PEI); and **(C)** water contact angle measurements on the same surfaces, respectively (Reproduced from [272]).

The photothermal properties of the different supports were assessed through irradiation with a 980nm - continuous wave laser, while the samples were placed in wells with 1 mL of water for 10 min; the diameter of the laser beam was adjusted directly to the well (**Fig. 5.6**). The heating properties of Kapton foil and Kapton coated with a continuous Au film are also evaluated for comparison. While Kapton and K/Au film did not show photothermal heating ability under our experimental conditions (600 s of irradiation at 980 nm), K/Au NH displayed a steady increase of the temperature up to 500 s to reach about 42±1 °C, after 600 s of irradiation. Upon coating with rGO-PEI, the temperature of the K/Au NH/rGO-PEI increased to 70 °C under the same photothermal irradiation conditions, indicating its enhanced photothermal heating ability.

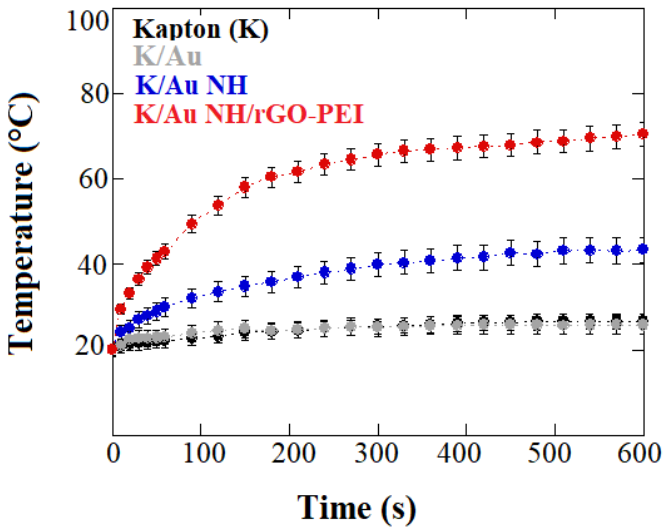

Figure 5.6. Temperature changes of different samples after 10 min of NIR irradiation (980 nm). Reproduced from [272].

5.3.4 Bacteria capture and photothermal killing

To assess the capture efficiency of K/Au NH/rGO-PEI surface, the following experiment was performed. Samples of Kapton, K/Au NH/rGO and K/Au NH/rGO-PEI were immersed in the bacterial suspension (1 mL), previously diluted to the desired concentration (10^3 cfu mL^{-1}). After 1h of incubation, an aliquot of 300 μL was taken from each well and used for plating on agar plates. After overnight incubation of the plates at 37°C, we performed counting and comparing colony forming units for the samples with the control, in order to calculate the percentage of the bacteria remaining in the solution and the bacteria attached to the surface. The capture efficiency of K/Au NH/rGO-PEI nanoheater towards *E. coli* bacteria was 42 % and towards *S. aureus* bacteria it was 47% (**Table 5.1**).

Table 5.1. Capture efficiency at 10^3 cfu mL^{-1} bacteria concentration. Reproduced from [272].

Sample	Incubation time	*E. coli* - Percentage of bacteria in the solution	Capture efficiency of *E. coli*	*S. aureus*- Percentage of bacteria in the solution	Capture efficiency of *S. aureus*
Kapton	1 h	100 %	0	100 %	0
K/Au NH/rGO	1 h	95 %	5 %	98 %	2 %
K/Au NH/rGO-PEI	1 h	58 %	42 %	53 %	47 %

The ability of the K/Au NH/rGO-PEI nanoheater to capture and kill bacteria was assessed for both Gram-positive *S. aureus* and Gram-negative *E. coli* bacteria under NIR (980 nm) laser continuous irradiation for 10 min. The morphology of the nanoheater immersed in a bacteria solution for 2 h before and after laser irradiation was visualized using SEM (**Fig. 5.7** and **5.8**).

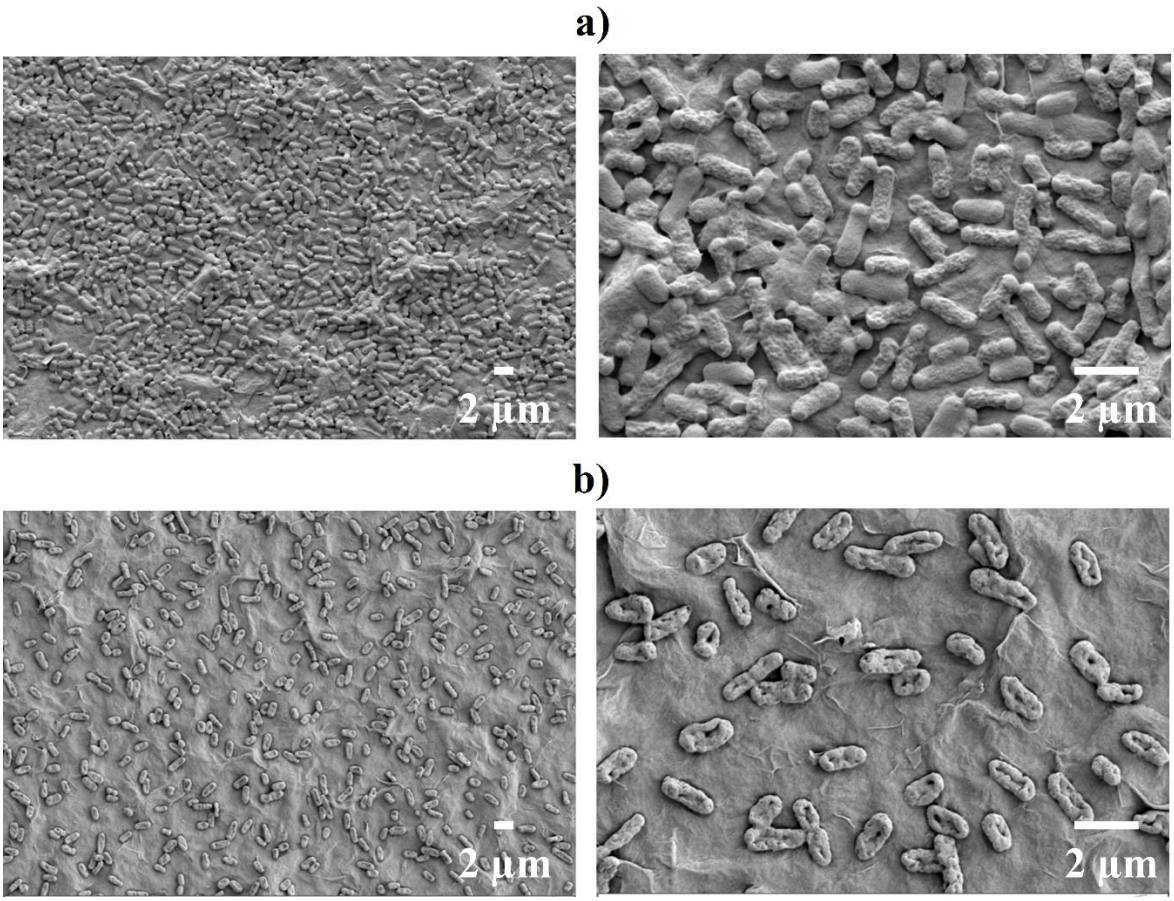

Figure 5.7. SEM images of *E. coli* K-12 MG1655 after 2 h of incubation a) before and b) after laser irradiation at 980 nm for 10 min (reproduced from [272]).

The SEM images of *E. coli* bacteria after 2 h of incubation before laser irradiation are shown in **Fig. 5.7a**. It can be easily observed that the nanoheater surface is covered with a dense and undamaged monolayer of bacteria with a rod–shaped morphology. On the contrary, after laser irradiation for 10 min, a decrease in the number of attached *E. coli* bacteria was obvious, but also the cells appeared to be damaged with the pronounced rupture of their outer membrane (**Fig. 5.7b**).

A similar observation can be made for *S. aureus* bacteria (**Fig. 5.8**). The typical near-spherical shape of cocci completely covered the surface of K/Au NH/rGO-PEI nanoheater after 2 h of incubation before laser irradiation (**Fig. 5.8a**). After 10 min of laser irradiation, the number of bacteria in a monolayer dramatically decreased, and cells showed different forms of damages on the cell surface (**Fig. 5.8b**).

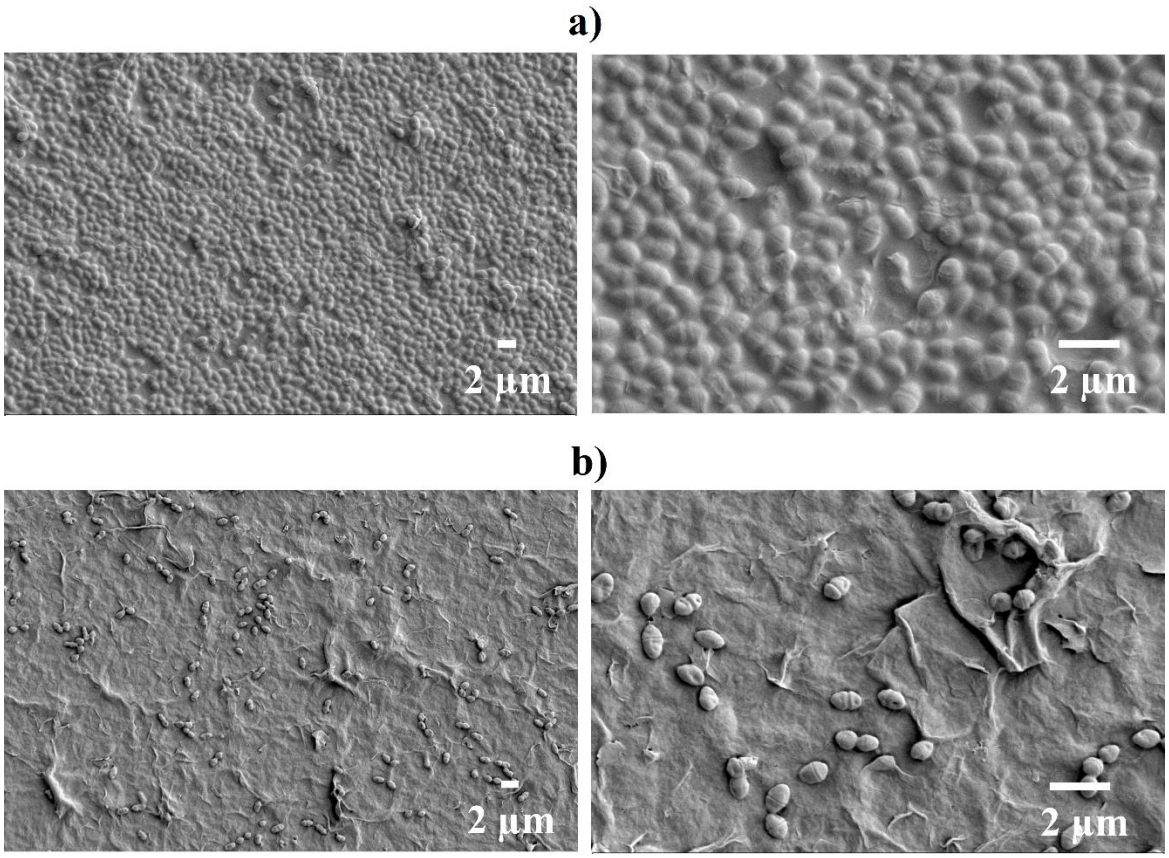

Figure 5.8. SEM images of *S. aureus* after 2 h of incubation a) before and b) after laser irradiation at 980 nm for 10 min (reproduced from [272]).

SEM images confirmed both *E. coli* and *S. aureus* adhesion to rGO-PEI surface, and bacteria killing caused by hyperthermia. Furthermore, SEM imaging and the cell viability evaluation (**Fig. 5.9**) confirmed that rGO-PEI coating itself was not toxic to bacteria without laser irradiation.

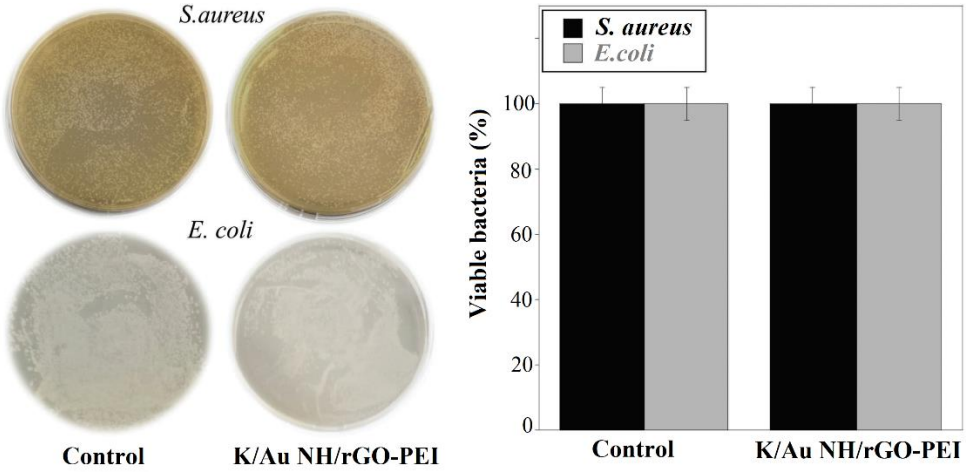

Figure 5.9. Typical photographs of *S. aureus* and *E. coli* colonies and the corresponding statistical histograms after 2 h of incubation with K/Au NH/rGO-PEI (reproduced from [272]).

As can be seen in **Fig. 5.9**, the volume of viable *E. coli* and *S. aureus* cells after 2 h of incubation on the nanoheater surface is almost the same as the control group. Another aspect of this research is the non-specificity of bacteria capture by PEI. Indeed, the presence of amino groups in the

PEI backbone confers an overall positive charge to the surface in water. Under these conditions, the surface is capable of interacting by electrostatic interactions with any chemical or biological matter that bears a negative charge. This property is of high importance for water cleaning applications.

5.3.5 Bacteria biofilm destruction

It is well known that the pathogenic bacteria grown on a surface in the form of biofilm are more difficult to eradicate, in comparison to their free-floating planktonic cell counterparts.

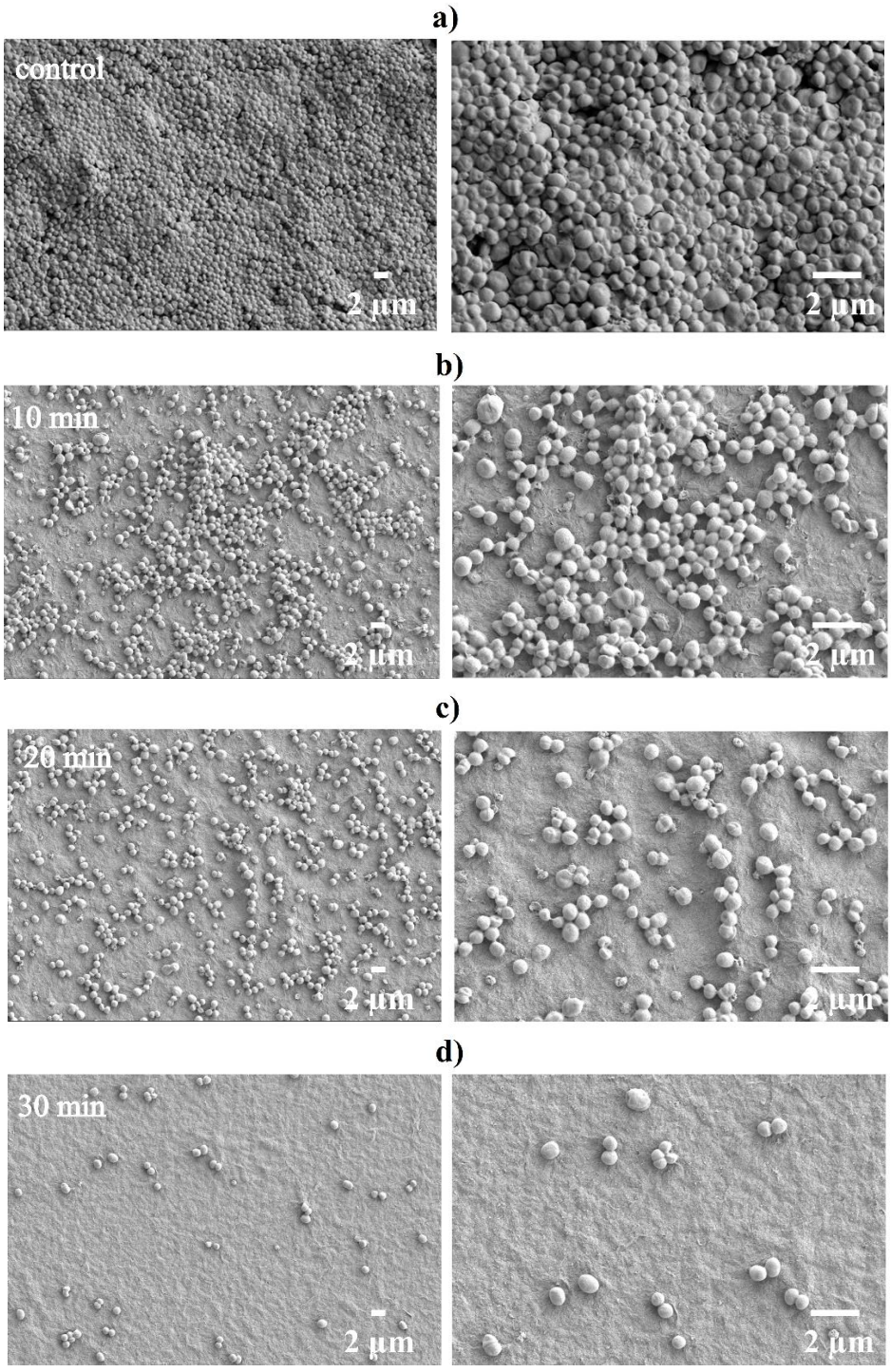

Figure 5.10. SEM images of *S. epidermidis* biofilm a) before and after laser irradiation at 980 nm for b)10 min, c) 20 min and d) 30 min**.** Reproduced from [272].

Living as a structured community of microbial cells, surrounded by their self-produced extracellular polymeric matrix, significantly increases their tolerance and resistance to the inhibitory effects of antibacterial agents [13]. In the present study, we investigated the capability of K/Au NH/rGO-PEI device to destroy *S. epidermidis* biofilms after NIR irradiation for a given time period, by SEM and by using a plate-counting method. Before laser irradiation, a uniform and thick biofilm structure consisting of multi-layered spherical microbial cells can be observed (**Fig. 5.10a)** on the surface of K/Au NH/rGO-PEI nanoheater. After 10 min of irradiation, the SEM images show obvious decrease in the biofilm mass, as well as morphological damage and a collapse of the bacterial cell membrane in the biofilm (**Fig. 5.10b**). After 20 min of irradiation, a noteworthy decrease in the biofilm mass can be observed (**Fig. 5.10c**) and finally, the biofilm was almost completely destroyed after 30 min of treatment (**Fig. 5.10d**).

It has to be highlighted that the NIR irradiation alone, in the absence of nanoheater, had no visible effects on the biofilm integrity. SEM image of *S. epidermidis* grown on a glass slide is presented in **Figure 5.11**. It can be observed that there is no change in the biofilm volume and structure before (**Fig. 5.11a)** and after (**Fig. 5.11b)** laser irradiation.

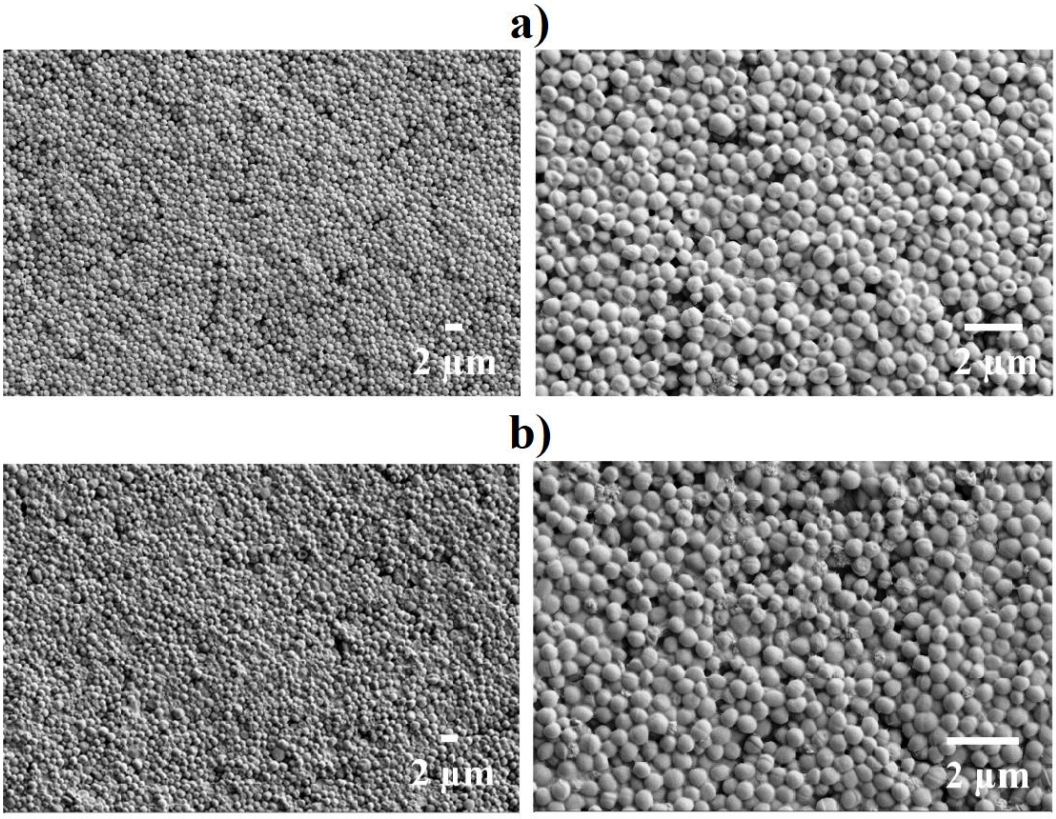

Figure 5.11. SEM images of *S. epidermidis* biofilm a) before and b) after laser irradiation at 980 nm for 10 min, following 30 h of incubation on the glass slide. Reproduced from [272].

As indicated by analysis of the survival rate and biofilm destruction, the mortality rate of the bacteria from the biofilm grown on the surface of nanoheater was increasing with the irradiation time, while the supernatant was sterile already after 10 min of irradiation (**Fig. 5.12**).

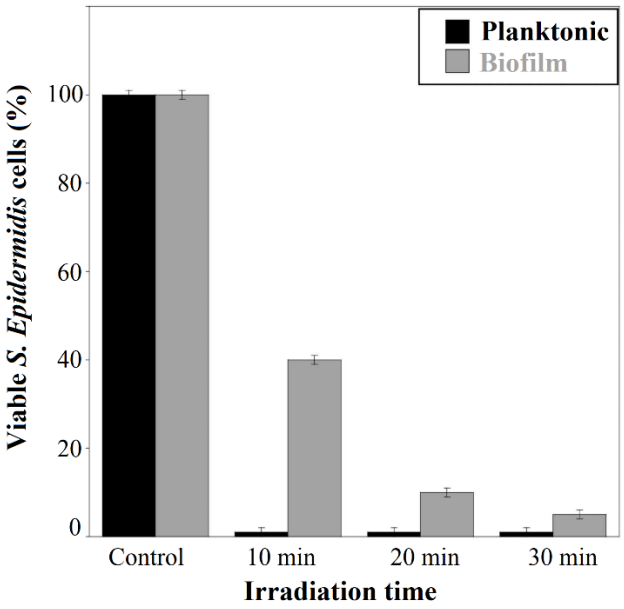

Figure 5.12. Planktonic and biofilm cell viability evaluation of *S. Epidermidis* at different laser irradiation times (reproduced from [272]).

5.3.6 Cytotoxicity assay

The indirect *in vitro* cytotoxicity test of K/Au NH/rGO-PEI nanoheater revealed the absence of release of cytotoxic components from the nanocomposite matrix during the 24 h of immersion in DMEM. As can be seen in **Fig. 5.13a**, the relative viability of NG108-15 cells remained above 95%. Our results indicate that the nanocomposite is stable. In contrast, the direct *in vitro* cytotoxicity demonstrated that the cells are not able to attach and grow on the sample. After 24h of incubation, compared with glass and Kapton, a significant decrease in cell viability was measured for K/Au NH/rGO-PEI nanoheater **(Fig. 5.13b).**

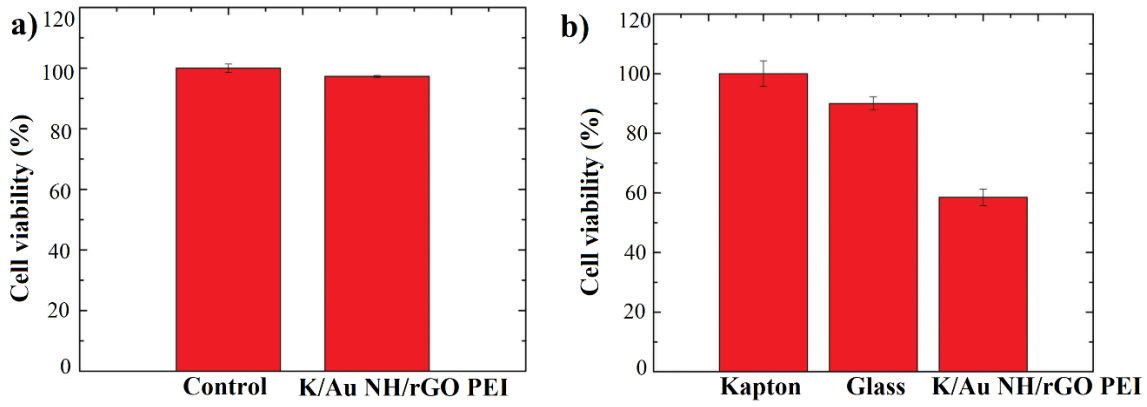

Figure 5.13. Relative cell viability of NG108-15 cells after 24 h of culture in DMEM (control) and DMEM in which K/Au NH/rGO-PEI matrix was previously immersed for 24 h (indirect cytotoxicity test) (a) and after 24 h of culture on 1 cm^2 Kapton, glass and K/Au NH/rGO-PEI substrates (direct cytotoxicity test) (b). Reproduced from [272].

5.3.7 Reuse of K/Au NH/rGO-PEI nanoheater

Apart from excellent antibacterial efficiency, an ideal antibacterial nanocomposite should allow the reuse, in order to lower the costs of the production. After the capture and heating experiments, the K/Au NH/rGO-PEI nanoheater was rinsed in ethanol and recovered by dropcasting 50 µL of previously prepared PEI solution (1 mg/mL). This change did not compromise the heating ability of K/Au NH/rGO-PEI nanoheater, nor did influence its cytotoxicity. After drying, the sample was rinsed and then immersed in MQ water for 3h to release excess PEI molecules and finally washed with ethanol again, before the experiment. The capture efficiency of the reused and recovered K/Au NH/rGO-PEI nanoheater was 95 % for the *S. aureus* bacteria, and 67 % for *E. coli*. The same sample allowed a reuse without additional drop of PEI and the capture rate after the second reutilization was was above 40 % for both strains.

5.4 Conclusion

In this study, we developed a Kapton/Au nanoholes/reduced graphene oxide-polyethyleneimine (K/Au NH/rGO-PEI) nanoheater by using a simple and straightforward approach for efficient capture and photothermal killing of bacteria under NIR irradiation. The nanoheater takes advantage of the enhanced photothermal properties of the Kapton/Au NH upon coating with rGO-PEI. Additionally, the presence of PEI, a branched polymer containing a large amount of electron-rich amino groups, enables efficient capture of both Gram-positive and Gram-negative bacteria through electrostatic interactions. We demonstrated that the K/Au NH/rGO-PEI nanoheater was an effective photothermal agent toward both Gram-positive *S. aureus* and Gram-negative *E. coli* bacteria, under low-power NIR (980 nm) laser irradiation with complete bacteria eradication within 10 min. Additionally, the nanoheater revealed to be very efficient for *S. epidermidis* biofilm destruction upon 30 min irradiation at 980 nm. Nanoheaters with efficient antibacterial properties, that are non-toxic for environment have the great potential for water purification systems, biomedical and industrial applications. The rapid and effective antibacterial activity as well as UV to NIR region absorption property might make K/Au NH/rGO-PEI antibacterial nanocomposite function even under normal solar light.

Chapter 6. Antibacterial activity of gamma-irradiation pre-treated carbon quantum dots/polyurethane nanocomposites

In this chapter, I will present an antibacterial hydrophobic carbon quantum dots/polyurethane nanocomposite (hCQD-PU), with improved antibacterial properties caused by gamma-irradiation pre-treatment. Here, the photodynamic treatment of bacteria was applied. The hydrophobic quantum dots (hCQDs), which are able to generate ROS upon irradiation with low power blue light (470 nm), were incorporated in the PU polymer matrix, to form a photoactive nanocomposite (**Fig. 6.1**). Different doses of gamma irradiation (1, 10 and 200 kGy) were applied to the formed nanocomposite in order to modify its physical and chemical properties and improve its antibacterial efficiency. The pre-treatment by gamma-irradiation significantly influenced the increase of the production of ROS. Therefore, our hCQD-PU nanocomposite exhibited antioxidative activity under the ambient conditions, and prooxidative activity when irradiated by blue light. The hCQD-PU nanocomposite irradiated with the dose of 200 kGy demonstrated the best antibacterial properties, with the complete eradication of Gram-positive *S. aureus* and Gram-negative *E. coli* bacteria after 15 min of exposure to the blue lamp.

.

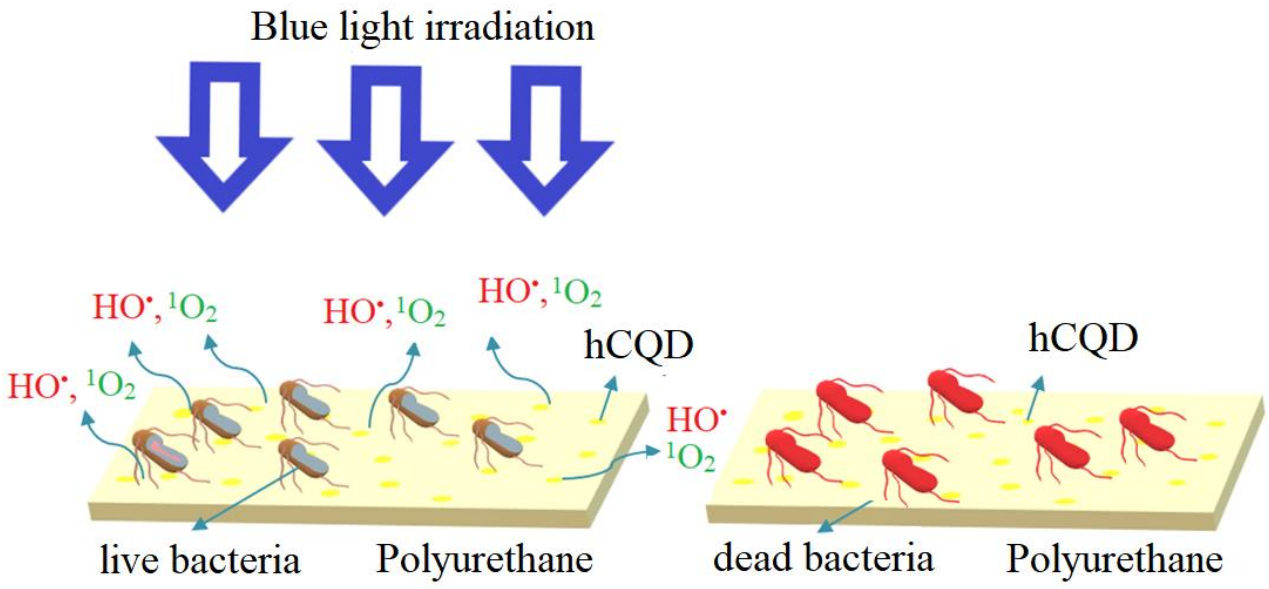

Figure 6.1. Schematic representation of the designed nanocomposite and the principle of destroying bacteria by PDT.

6.1 Experimental

6.1.1 Materials

Commercially available medical grade transparent polyurethane (PU) donated by American Polyfilm with a thickness of 1.0 mm was used. Polyoxyethylene-polyoxypropylene- polyoxyethylene Pluronic 68 was obtained from Interchim, France, and phosphoric acid and toluene were purchased from Sigma Aldrich, Germany and used as received.

6.1.2 Synthesis of hCQDs

Following the previously reported method, the synthesis of hCQDs was performed [283,284]. First, 1g of polyoxyethylene-polyoxypropylene-polyoxyethylene Pluronic 68 was dissolved in 100mL of water for about 15 min, in an ultrasonic water bath. Then 200 mL of phosphoric acid was added, and the mixture was stirred in order to produce a homogeneous reaction mixture. The reaction mixture was then heated on a magnetic stirrer at 250 °C for 145 min until the solution became brown. The mixture was cooled down to room temperature, and then 250 mL of water was added and stirred for another 2 h to produce a brownish-black colored precipitate. Finally, 300 mL of toluene were added to the solution. The reaction mixture was stirred overnight at room temperature until the solution turned yellow. Finally, the organic phase was decanted and then filtered using a vacuum pump, through hydrophobic filters with pore sizes of 0.2 and 0.1 μm. The obtained product was a colloid of hydrophobic carbon quantum dots – hCQDs. The reason we chose hydrophobic CQDs is the fact that the polyurethane which we have chosen as a matrix of nanocomposite swells in toluene, therefore, we needed CQDs which were soluble in toluene.

6.1.3 Preparation of hydrophobic carbon quantum dots/polyurethane nanocomposite (hCQD-PU)

A transparent PU was immersed in the solution of hCQDs (1 mg mL^{-1}) during 48 h. After, the obtained nanocomposite hCQD-PU was dried in a vacuum furnace for 12 h at 80 °C, in order to evaporate all the remaining toluene. The hCQDs were incorporated inside of the polymer matrix by the swell-encapsulation-shrink method. Then, the samples were exposed to gamma irradiation at 1, 10 and 200 kGy doses (throughout the manuscript samples are labeled as hCQD-PU-1, hCQD-PU-10, and hCQD-PU-200). As references (control samples) in some experiments, the hCQDs dispersion in toluene was also exposed to gamma irradiation at the same doses applied (hCQD-1, hCQD-10 and hCQD-200), as well as the pure polyurethane that was exposed to the highest irradiation dose (PU-200) and hCQD-PU before gamma-irradiation.

The samples were irradiated by gamma-ray flux from ^{60}Co nuclide with the photon energy of 1.3MeV (Centre of Irradiation, Vinca Institute of Nuclear Sciences) at a dose rate of 13 kGy h^{-1}.

6.2 Characterization of the hCQDs and gamma irradiated hCQD-PU nanocomposites

Dynamic mechanical analysis (DMA) of neat PU and gamma irradiated hCQD-PU samples was performed using a TA Instrument dynamic mechanical analyzer DMA Q800. The temperature range was from -100°C to 100°C. The samples of uniform shapes were measured in the module tensile multi-frequency strain at 10 Hz, strain amplitude of 5 μm and heating rate 2 °C·min^{-1}. All measurements were carried out without and with irradiation by blue light during 24 h.

Atomic force microscopy (AFM) was used to examine the surface morphology of the gamma-irradiated hCQD-PU nanocomposites. Measurements were performed using a Quesant microscope (Ambios Technology, USA), and its own software. The AFM measurements were performed in air, using silicone T-shaped cantilever with a spring constant of 40 N/m. All images were obtained with 512 × 512 image resolution over different square areas. Root-mean-square roughness-RMS of hCQDs-PU nanocomposites was determined by Gwyddion software [285].

Photoluminescence (PL) measurements of the gamma-irradiated hCQD-PU nanocomposites were performed on an RF-5301PC (Shimadzu, Japan) spectrofluorophotometer, at excitation wavelengths between 320 and 480 nm.

6.2.1 Determination of reactive oxygen species

6.2.1.1 Quenching of free radicals

For the investigation of radical scavenging activity (RSA) of composites, we used the DPPH assay [286]. This experiment is based on the feature of 2,2-diphenyl-1-picrylhydrazyl (DPPH) molecule to show strong absorption in the UV-Vis spectrum, located at 518 nm. In this form, DPPH is a stable free radical. In the presence of antioxidants, DPPH forms a yellow compound which can be observed by UV-vis as a lowering in the intensity of the band at 518 nm. To calculate the value of RSA, the fresh solution of DPPH (100 μM in methanol) was prepared and the different sizes of hCQD-PU nanocomposites were added: 0.5×0.5, 1.0×1.0, 1.5×1.5 cm^2. Nanocomposites were incubated with DPPH solution for 1 h, in dark and we measured the intensity of absorbance of the solution at 518 nm using a Spectrophotometer Shimadzu UV-Visible 2600 (Shimadzu Corporation, Tokyo, Japan). A methanol solution of ascorbic acid was used as a standard. The values of RSA for each composite were calculated using the formula RSA (%) = $(Ac\text{-}A_{PU\text{-}CQDs})/Ac \times 100$, where Ac is the intensity of absorption of control (DPPH in methanol) and $A_{PU\text{-}CQD}$ is the intensity of the absorption band of a solution in which composites were dipped. Ascorbic acid was used as a standard. Measurements were replicated three times.

Additionally, the ability of composites to adsorb DPPH was also investigated. In order to prevent false positive radical scavenging activity, which may be caused by physical adsorption of DPPH molecules by hCQD-PU, we soaked the composites (1.5 x 1.5 cm^2) into DPPH methanol solution (100 μM) and after 1 h of incubation in dark, we recorded absorption spectra of composites (without previous rinsing).

6.2.1.2 Production of hydroxyl radicals (•OH)

The fluorescence technique was used to analyze the formation of •OH radicals on the sample surface under UV irradiation, using terephthalic acid that reacts readily with •OH radicals, and produces highly fluorescent product, 2-hydroxyterephthalic acid [287]. The intensity of the peak attributed to 2-hydroxyterephthalic acid was known to be proportional to the amount of •OH radicals formed [287]. The selected concentration of terephthalic acid solution was 5×10^{-4} M in a diluted NaOH aqueous solution with a concentration of 2×10^{-3} M. It has been proved that under these experimental conditions (concentration of terephthalic acid < 10^{-3} M, room temperature), the hydroxylation reaction of terephthalic acid proceeds mainly by •OH radicals [287]. Gamma-irradiated hCDQ-PU samples were added to 200 mL of the 5×10^{-4} M terephthalic acid solution in 2×10^{-3} M NaOH and then exposed to the blue light (470 nm), with the power of the lamp of 15 W. Sampling was performed every 15 min. The solution was analyzed after filtration through 0.45 μm membrane filter, on a Hitachi F-4500 fluorescence spectrophotometer. Upon excitation at 315 nm, the product of terephthalic acid hydroxylation (2-hydroxyterephthalic acid) exhibited a peak at approximately 425 nm.

6.2.1.3 Singlet oxygen production and oxygen lifetime measurements

For the determination of singlet oxygen production, we used two different approaches, the first one includes the time-resolved near-infrared luminescence spectroscopy and the second one is based on the use of electron paramagnetic resonance (EPR) technique.

A piece of the hCQD/PU nanocomposite was inserted into a quartz cell in the oxygen or air atmosphere. For measurements in oxygen-free conditions, the samples were evacuated for at least 15 minutes. The total pressure in the cell was measured with capacitance manometers (MKS Baratron). The kinetics of singlet oxygen, $O_2(^1\Delta_g)$, after excitation of individual samples COMPEX 102 excimer laser (wavelength 308 nm, pulse width ~28 ns) was measured using time-resolved near-infrared luminescence spectroscopy. Luminescence of $O_2(^1\Delta_g)$ at 1270 nm was recorded in reflection mode using a Judson Ge diode and interference filters. The signal from the detector was collected in a 600MHz oscilloscope (Agilent Infiniium) and transferred to a computer for further analysis. The signal-to-noise ratio of the signals was improved by averaging of 1000 individual traces. The initial part (up to 2 μs) failed due to a large scattering of the laser pulse and luminescence of hCQDs and other compounds, and it was not used for evaluation.
The transient absorption spectra in the visible part of spectra (400-720 nm) and kinetics of transients at 520 nm were recorded with a 150 W Xe lamp (Phillips) equipped with a pulse unit and an R928 photomultiplier (Hamamatsu) using a laser kinetic spectrometer LKS 20 (Applied Photophysics, UK).

Electron paramagnetic resonance (EPR) is a technique used to study chemical species with unpaired electrons. EPR was used to determine the singlet oxygen generation of different hCQD-PU nanocomposites. With $^1O_2$, 2,2,6,6-tetramethylpiperidine (TEMP) molecules quickly react and form a stable EPR active product, TEMP-$^1O_2$ (TEMPO). The concentration of TEMP was 2 wt%. The EPR experiments were performed at ambient temperature using a Varian E-line spectrometer operated at a frequency of 9.5 GHz. The gamma irradiated hCQD-PU nanocomposites and PU control were dipped in TEMP solution. All samples were treated in the following conditions: dark and exposed to BL, for 12h, respectively. The wavelength of BL was 470 nm (3W, V-TAC, Bulgaria).

6.2.2 Bacteria culture and preparation

The bacteria used in this study were *S. aureus* CCM 4516 (Gram-positive) and *E. coli* CCM 4517 (Gram-negative) pathogenic strains. The bacterial strains were purchased from CCM (Czech Collection of Microorganisms). Antibacterial activity was performed according to ISO 22196 standard – Measurement of antibacterial activity on plastics and other non-porous surfaces [288]. The dimensions of the tested samples were 2.5 × 2.5 cm^2. Blue light (470 nm) was used for the activation of hCQDs, the lamp power was 15 W, and the distance between samples and the lamp was 50 cm. The tested samples were irradiated for 15 and 5 min.

6.2.3 Biocompatibility studies

- Cytotoxicity study of released extracts

Cytotoxicity of extracts prepared in the presence of gamma-pretreated hCQD-PU nanocomposites, was determined. Before the experiments, samples (1×1 cm^2) were sterilized in ethanol and dried. Sterilized samples were then incubated in 1 mL of Dulbecco's Modified Eagle's medium (DMEM, Gibco®) supplemented with 10% fetal bovine serum (FBS, Gibco®) and 1% penicillin-streptomycin (Gibco®) during 24 h at 37 °C and 5% CO_2. After incubation, the released medium was diluted with fresh medium in different concentrations (from 1 % to 100 %) and tested in contact with cells for 24h. U-87 MG derived from a malignant glioma from a female patient by explant technique [ECACC 89081402, Sigma Aldrich, Saint-Quentin Fallavier, France] and HeLa cell line derived from cervical carcinoma from a 31 year old female [ECACC 93021013, Sigma

Aldrich, Saint-Quentin Fallavier, France] were used as model cell lines. Cells were maintained in DMEM supplemented with 10% FBS and 1% penicillin-streptomycin in a humidified incubator at 37°C and 5% CO_2. Briefly, cells were seeded at a density of 10^4 cells/well in a 96-well plate for 24 h before assay. The culture medium was then replaced with extracts. After 24 h, cells were washed with PBS and the cell viability was evaluated using resazurin cell viability assay. 100 mL of the resazurin solution (11 µg mL^{-1}) in DMEM/10% FBS were added to each well and the plate was incubated for 4 h in the humidified incubator. The fluorescence emission of each well was measured at 593 nm (20-nm bandwidth) with an excitation at 554 nm (18-nm bandwidth) using a Cytation™ 5 Cell Imaging Multi-Mode Reader (BioTek Instruments SAS, France). Each condition was replicated three times and the mean fluorescence value of non-exposed cells was taken as 100% cellular viability.

- **Cell proliferation**

U-87 MG [ECACC 89081402, Sigma Aldrich, Saint-Quentin Fallavier, France] and HeLa cell line [ECACC 93021013, Sigma Aldrich, Saint-Quentin Fallavier, France] were maintained in DMEM supplemented with 10% FBS and 1% penicillin-streptomycin in a humidified incubator at 37 °C and 5% CO_2.

Determination of cell morphology: Determination of cell morphology was performed by Hoechst 33258 (Invitrogen, USA) for staining the DNA. First, the concentration of 80000 cells mL^{-1} in volume 100 µL was seeded directly onto samples, and after 1 h, 1 mL of complete culture medium was added. It was cultivated for 48 h. Cells were then fixed, stained and finally observed by fluorescence microscopy

Cell fixation: To fix cells, 4 % paraformaldehyde (PFA) was added to cells for 15 min. After, the cells were washed 3 times by PBS (Invitrogen, USA) and 1 ml of PBS containing Hoechst 33258 (5µg/mL) were added to samples and left to incubate in the dark. After 10 min, cells were washed again and ready for microscopic observation.

Microscopic observation: Fluorescence images (DAPI exc. 377/50 nm and em. 447/60 nm) were captured using a Cytation™ 5 Cell Imaging Multi-Mode Reader (BioTek Instruments SAS, France) and analysed by Gen5iPlus 3.04 Imaging Software.

6.3 Results and discussion

6.3.1 Fourier Transform Infrared - FTIR

FTIR spectroscopy was used to assess the presence of different functional groups (**Fig. 6.2a)**. FTIR spectra suggested that all the observed gamma irradiated hCQD-PU nanocomposites comprised an absorption peak at 3300 cm^{-1} attributed to O–H vibration mode. The peaks at 2919, 2852 and 2797 cm^{-1} belong to C-H stretching vibrations. The peaks at 1729, 1698 and 1635 cm^{-1} are ascribed to C=O bonds, while the peak at 1417 cm^{-1} is due to aromatic C=C bonds which are connected with the presence of sp^2 – hybridized graphitic cores [289]. The strong peaks at 1220 and 1080 cm^{-1} are attributed to C-O-C and C–O bonds, respectively. By analyzing the FTIR results, it was concluded that the same bands were identified in hCQD-PU nanocomposites for all the different doses of gamma irradiation. Also, comparing the FTIR results of hCQD-PU sample without gamma irradiation, from the reference [284], we can conclude that the same bands can be identified. Therefore, from this point of view, we can deduce that gamma irradiation, at any examined irradiation dose, had no influence on the overall presence of functional groups of hCQD-PU nanocomposites.

6.3.2 X-ray photoelectron spectroscopy (XPS)

XPS analysis was carried out to explore and compare the elemental composition of gamma-irradiated hCQD-PU nanocomposites (**Fig. 6.2 b, c, d**). The XPS elemental survey spectrum revealed that these nanocomposites were composed of the following elements: C, O and N (**Table 6.1**). By fitting C1s and O1s the content of the characteristic bonds in hCQD-PU-1, hCQD-PU-10 and hCQD-PU-200 were detected and compared.

Table 6.1. Elemental composition of gamma-irradiated hCQD-PU samples.

Name	hCQD-PU-1 (atomic %)	hCQD-PU-10 (atomic %)	hCQD-PU-200 (atomic%)
N1s	5.8	4.7	4.1
C1s	85.2	90.4	87.1
O1s	6.5	4.8	8.7

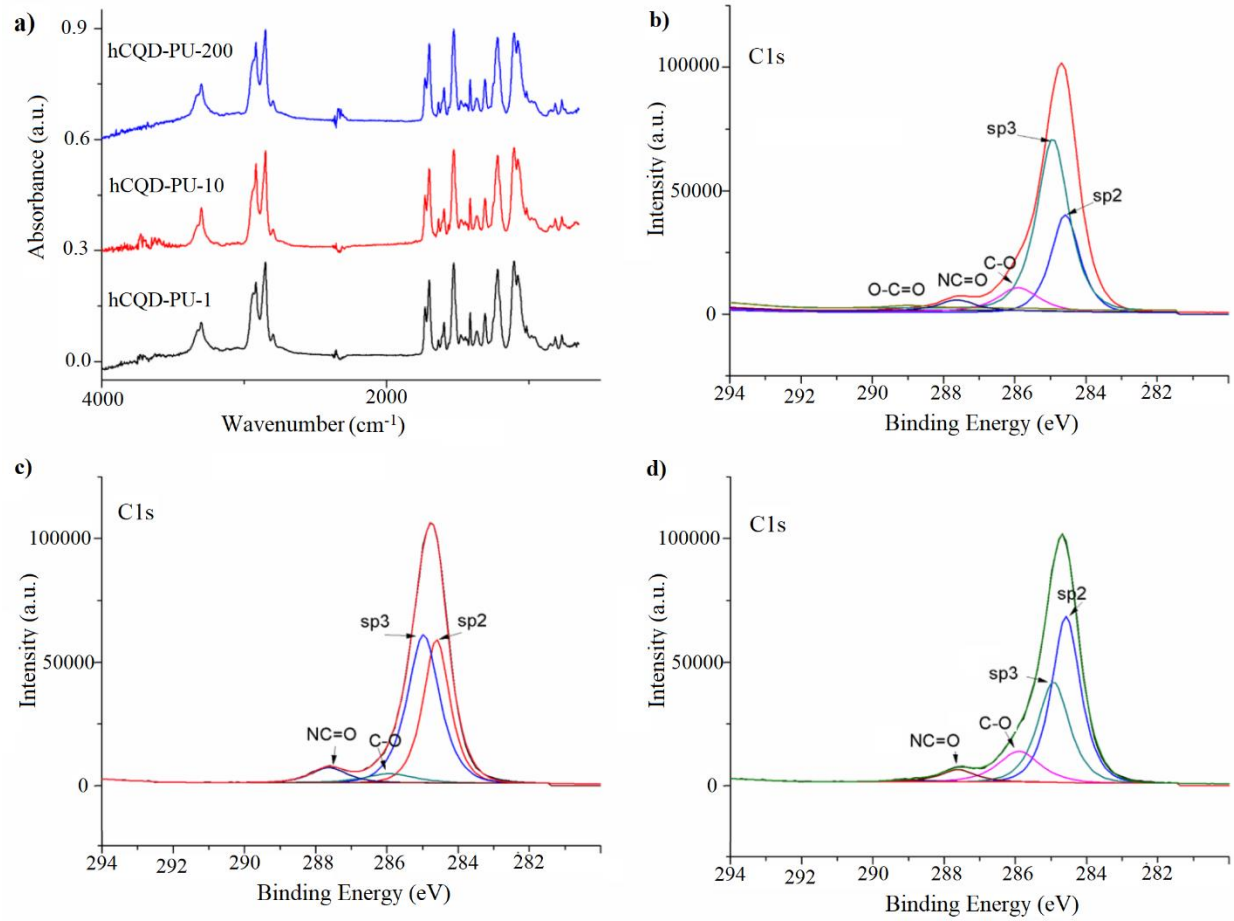

Figure 6.2. a) FTIR spectra of hCQD-PU-1, hCQD-PU-10 and hCQD-PU-200 samples; XPS C1 spectra of b) hCQD-PU-1; c) hCQD-PU-10 and d) hCQD-PU-200 nanocomposites. Reproduced from [290].

The XPS analysis showed that the content of oxygen is almost doubled in the sample hCQD-PU-200, compared to the sample hCQD-PU-10 (**Table 6.1**). According to the XPS results presented in **Fig. 6.2**, the percentage of sp^2 bonds increased with the increase of the dose of gamma irradiation (from 28.9% for hCQD-PU-1 to 49.2% for hCQD-PU-200). On the contrary, the percentage of sp^3 bonds decreased with the increase of the gamma irradiation dose (from 55.2 % for hCQD-PU-1 to 32.8 % for hCQD-PU-200), implying that the structure of hCQD inside the PU polymer matrix was becoming more arranged [291]. Obtained results are in accordance with the PL results, which demonstrated that the hCQD-PU-200 sample had the highest photoluminescence (section 6.3.7). However, the content of oxygenated bonds was the lowest for the hCQD-PU-10 sample. The contribution of C-O bonds first decreased from 10.2% for hCQD-PU-1 to 4.4% for the hCQD-PU-10 sample and then increased again to 13% for the hCQD-PU-200 sample. The presence of C=O bonds in the FTIR spectrum and the absence of the same bonds in XPS spectrum suggest that hCQDs are not formed on the surface of the polymer matrix but incorporated inside.

6.3.3 Leaching experiments

To exclude the existence of leaching from the gamma-irradiated hCQD-PU nanocomposites, samples (1×1 cm^2) were dipped in 20 mL of Milli-Q water for 24 h. Recorded UV-Vis spectra of water aliquots in which hCQD-PU nanocomposites were immersed, were compared with the UV-Vis absorbance spectra of gamma-irradiated toluene dispersions of hCQD (hCQD-1, hCQD-10 and hCQD-200). UV-vis spectrophotometry was used to explore the existence of leaching of the hCQD-PU nanocomposites. From **Fig. 6.3a,** the absorbance spectra of the gamma-irradiated hCQD dispersions can be observed, together with the absorbance spectra of the aliquots of water in which hCQD-PU-1, hCQD-PU-10 and hCQD-PU-200 nanocomposites were immersed for 24 h. The specific peak value of hCQD cannot be found in the spectra of water aliquots, indicating that there was no leaching of hCQD in water. **Fig. 6.3b** presents an absorbance spectrum of hCQD-PU-1, hCQD-PU-10 and hCQD-PU-200 nanocomposites before and after 24 h immersion in water. The spectra prove that there is no difference between the nanocomposites before and after dipping the samples in water. Therefore, it can be concluded that leaching of the hCQD from polymer matrix does not occur, when the samples are immersed in water.

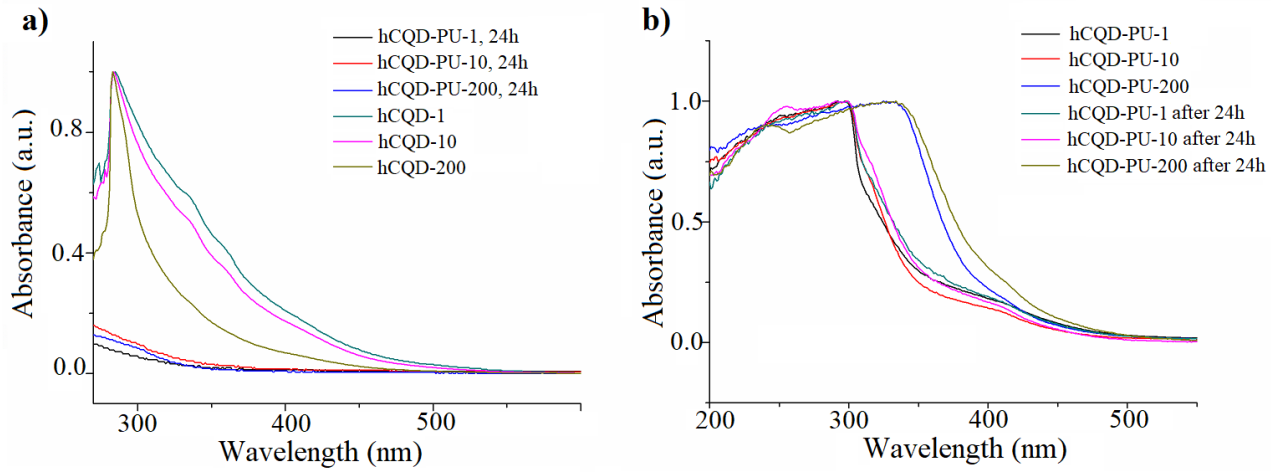

Figure 6.3. a) UV-Vis spectra of gamma-irradiated hCQDs dissolved in toluene and aliquots of water in which hCQD-PU-1, hCQD-PU-10 and hCQD-PU-200 nanocomposites were dipped for 24h; b) Absorbance spectra of hCQD-PU-1, hCQD-PU-10 and hCQD-PU-200 before and after immersion in water for 24h. Reproduced from [290].

6.3.4 Wetting properties

Water contact angle (WCA) measurements were performed in order to explore the hydrophobicity/hydrophilicity of the prepared samples. The results show that the contact angle was decreasing with the increase of the dose of gamma irradiation, as compared to the contact angle before gamma pre-treatment [290] (**Table 6.2**). Lowering of contact angle is beneficial as it can improve the adhesion of bacterial cells. Some research results demonstrated that the adhesion is optimal when the contact angle is around 70°, while higher and lower contact angles reduce bacteria adhesion [292,293]. Differences in contact angle can be a consequence of different chemical composition or different surface structure [294], and in our samples, both effects are present.

Table 6.2 Surface roughness and contact angle.

Sample	Contact angle (°)	RMS roughness (nm)
hCQD-PU	112 ± 2	18 ± 1
hCQD-PU-1	96 ± 2	21 ± 1
hCQD-PU-10	84 ± 2	36 ± 1
hCQD-PU-200	73 ± 2	62 ± 1

6.3.5 Atomic force microscopy (AFM)

The morphology and surface roughness of hCQD-PU samples before and after gamma-irradiation were analyzed by AFM. We can easily detect the difference in the surface morphology of different samples from the AFM images (**Fig. 6.4**). This was confirmed by the study of the average surface roughness of each sample, obtained from several AFM images (**Table 6.2**). The surface roughness significantly increased with the increase of the gamma irradiation dose. This is not completely in accordance with the contact angle measurements, because generally when a hydrophobic material becomes rougher it reaches super-hydrophobicity [295]. However, after gamma-pretreatment, there was a significant change in the chemical composition of materials, which also influenced the surface roughness. These results are in accordance with the results of Gorna et al. which also showed the increase of surface roughness after gamma-irradiation of polyurethane samples [296].

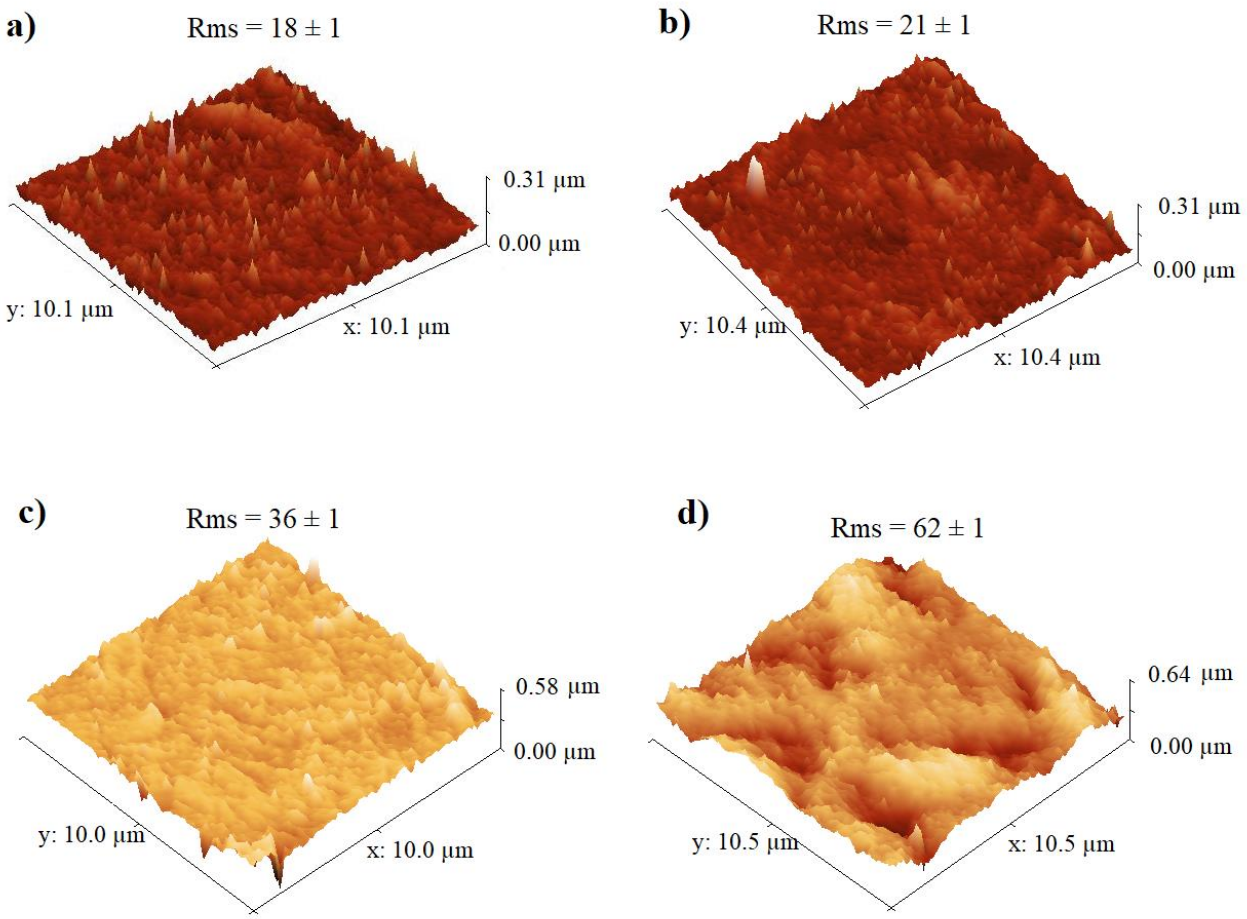

Figure 6.4. 3D AFM images of hCQD-PU sample before (a) and after gamma pre-treatment: b) hCQD-PU-1, c) hCQD-PU-10, and d) hCQD-PU-200, scan size in each image is 10×10 µm^2.

6.3.6 Dynamic mechanical analysis (DMA)

The dynamic mechanical analysis (DMA) was carried out to determine the effect of gamma irradiation on the integrity of the polymer matrix. As a control sample, we used pure polyurethane (PU). The DMA results for neat PU matrix and gamma irradiated samples at different doses (1, 10 and 200 kGy) are presented in **Fig. 6.5 (a–c)**. As can be seen from **Fig. 6.5 (a and b),** gamma irradiation did not significantly affect the structure of the polymer matrix with encapsulated hCQDs. The values of T_g temperatures for neat PU and gamma irradiated samples (hCQD-PU-1, hCQD-PU-10 and hCQD-PU-200) are presented in **Table 6.3**. As can be seen from **Table 6.3**, gamma irradiation contributes to the small decrease of T_g from 0.5 to 1.5^{o}C compared to neat PU. According to the results presented in **Fig. 6.5 (a-c)**, the peak of tan δ curves for all the samples corresponds to a molecular motion of the amorphous region in the semicrystalline hard-segment phase of PU samples. We were not able to detect T_g temperature of soft-segment of PU samples due to the lack of the peaks at low temperatures.

Table 6.3 Values of T_g temperatures for all the samples.

Sample	**PU**	**hCQD-PU-1**	**hCQD-PU-10**	**hCQD-PU-200**
T_g (^{o}C)	-21.52	-22.59	-22.04	-22.85

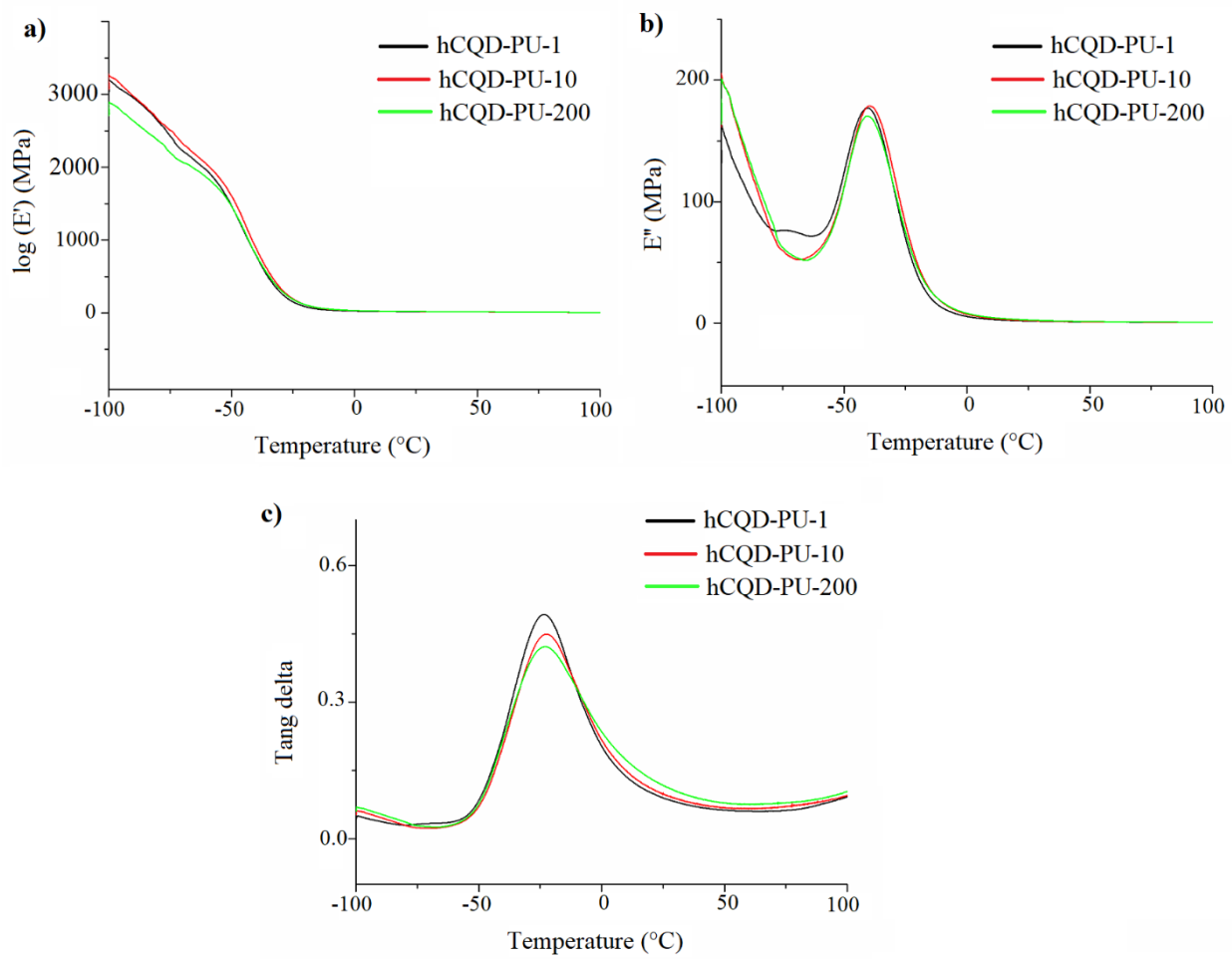

Figure 6.5. The dynamic mechanical analysis graphs: a) Storage modules; b) Loss modules; c) Tang delta. Reproduced form [290]. Temperature (°C)

6.3.7 Photoluminescence (PL) measurements

Photoluminescence (PL) of gamma-irradiated hCQD-PU was investigated at different laser excitation wavelengths: from 320 to 480 nm (**Fig. 6.6**). According to Mitra et al. [297], the hCQD are probably formed by fragmentation of PF-68 forming the carbon core. Remaining hydroxyl and carbonyl groups on the surface of the hCQD result in the formation of defect sites [182] and emissive traps [172], which contribute to its PL properties. Radiative recombination of excitons trapped within the defects [25,26] produces the most intense PL band [23]. Therefore, the PL of gamma modified nanocomposites originates from hCQDs incorporated inside the polymer matrix [284,297].

The highest intensities of emission bands were detected at the excitation wavelength of 360 nm for both hCQD-PU-1 and hCQD-PU-10 samples, while for hCQD-PU-200 sample the highest intensity was measured at 400 nm excitation wavelength. However, for further examination, we used the excitation wavelength of 360 nm, in order to compare the spectra. As excitation wavelength was increasing, red-shifted emission was noticed, for all the samples. According to some authors, the dominant role in the mechanism of PL emission stems from small sp^2 isolated within the sp^3 carbon network clusters, while the surface states that are oxygen-containing functional groups and defects localized on the edge of sp^2 clusters play a supplementary role in the CQDs emission [298,299].

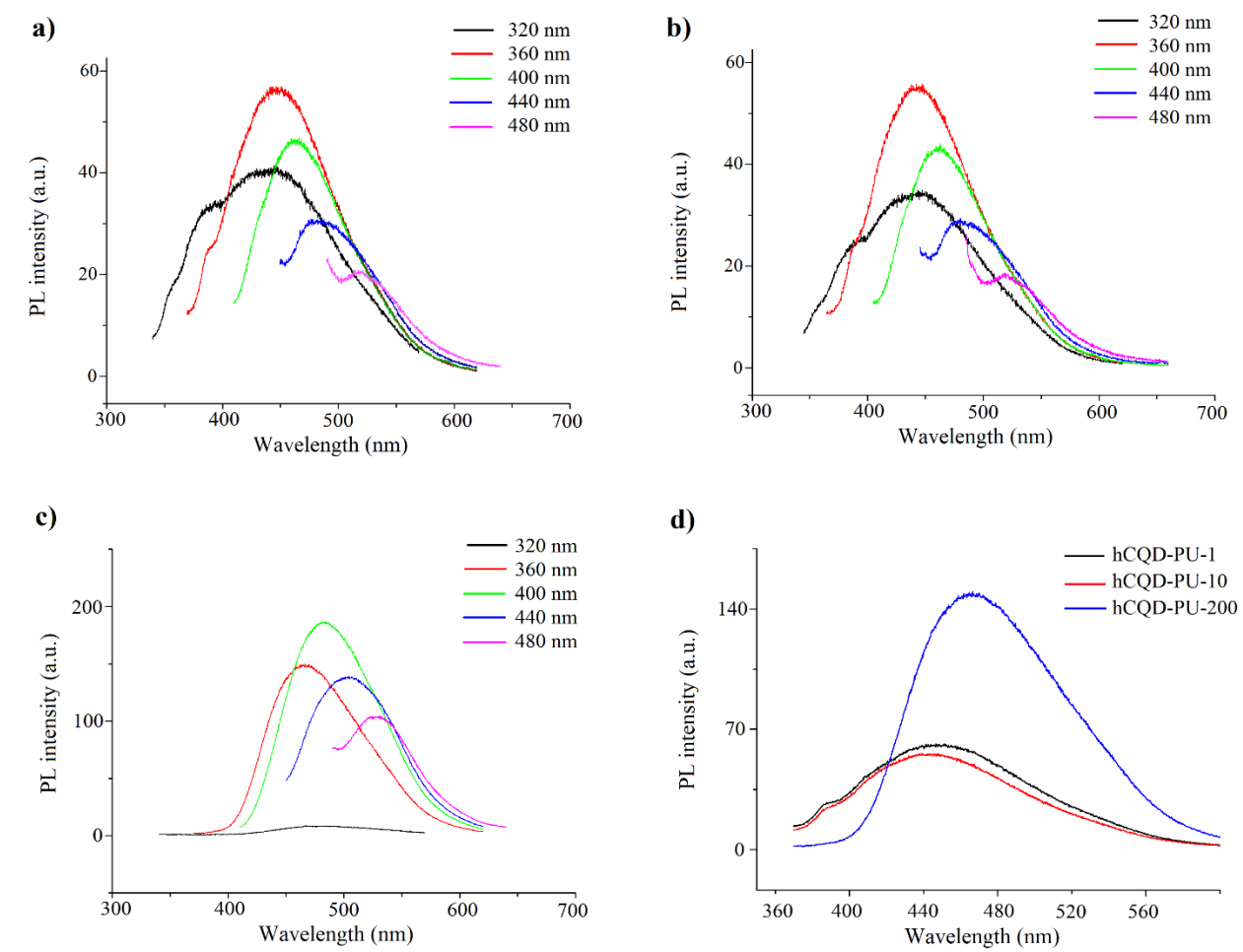

Figure 6.6. Photoluminescence spectra of samples: a) hCQD-PU-1, b) hCQD-PU-10, c) hCQD-PU-200 at different laser excitation wavelengths and d) PL spectra of three samples measured at pulsed laser excitation at 360 nm. Reproduced from [290].

As can be observed on **Fig. 6.6d**, the irradiation dose of 200 kGy has caused significant changes in the PL intensity, which is almost two times more intensive compared to the emission of hCQD-PU-1 and hCQD-PU-10 samples. This result is in accordance with the XPS results which proved that the percentage of sp^2 bonds is by 10% higher in hCQD-PU-200 than in hCQD-PU-10 sample. Also, the number of C-O groups increased in the hCQD-PU-200 sample. From these results, we can conclude that the content of sp^2 bonds and oxygen-containing functional groups play an important role in the mechanism of photoluminescence of these samples. Therefore, the role of gamma irradiation was very important here in enhancing the photoluminescence. We can also observe (**Fig. 6.6d**) that the emission band of hCQD-PU-200 sample is red-shifted compared to hCQD-PU-1 and hCQD-PU-10 samples. The shifts of the emissions spectra of CQD could be the result of changes in the defect structure, edge configuration, size or shape [300–302]. This may be explained by the decreasing percentage of sp^3 and increasing of sp^2 bonds, implying the more arranged structure of hCQD inside the polymer after gamma pre-treatment [291].

6.4 ROS determination

6.4.1 DPPH radical scavenging assay

The intensity of the absorption at around 520 nm was measured, after 1 h of incubation of DPPH$^{\bullet}$ with nanocomposites, in the dark, in order to assess the radical scavenging activity - RSA (**Fig. 6.7**). In **Figure 6.7a**, UV-vis spectra of DPPH incubated with hCQD-PU-1 are presented. As we can see, the intensity of the DPPH band is lowered after incubation with both nanocomposite and bare PU. As the size of the nanocomposite increases, the intensity of the band at 520 nm decreases. The lowest observed intensity is when the size of the nanocomposite was the highest (1.5×1.5 cm^2). Thus, it can be concluded that the intensity of DPPH absorption band is proportional to the size of the nanocomposite. Similar behavior was observed for the other two nanocomposites, where the intensity of DPPH band is decreasing with the size of nanocomposite dipped in DPPH solution (**Fig. 6.7b and c**). Given that the antioxidative activity arises from gamma pre-treated hCQDs, increasing the nanocomposite's size leads to higher amount of hCQDs incorporated inside of the polymer matrix, and consequently to enhanced antioxidative activity of the gamma pre-treated hCQD-PU samples.

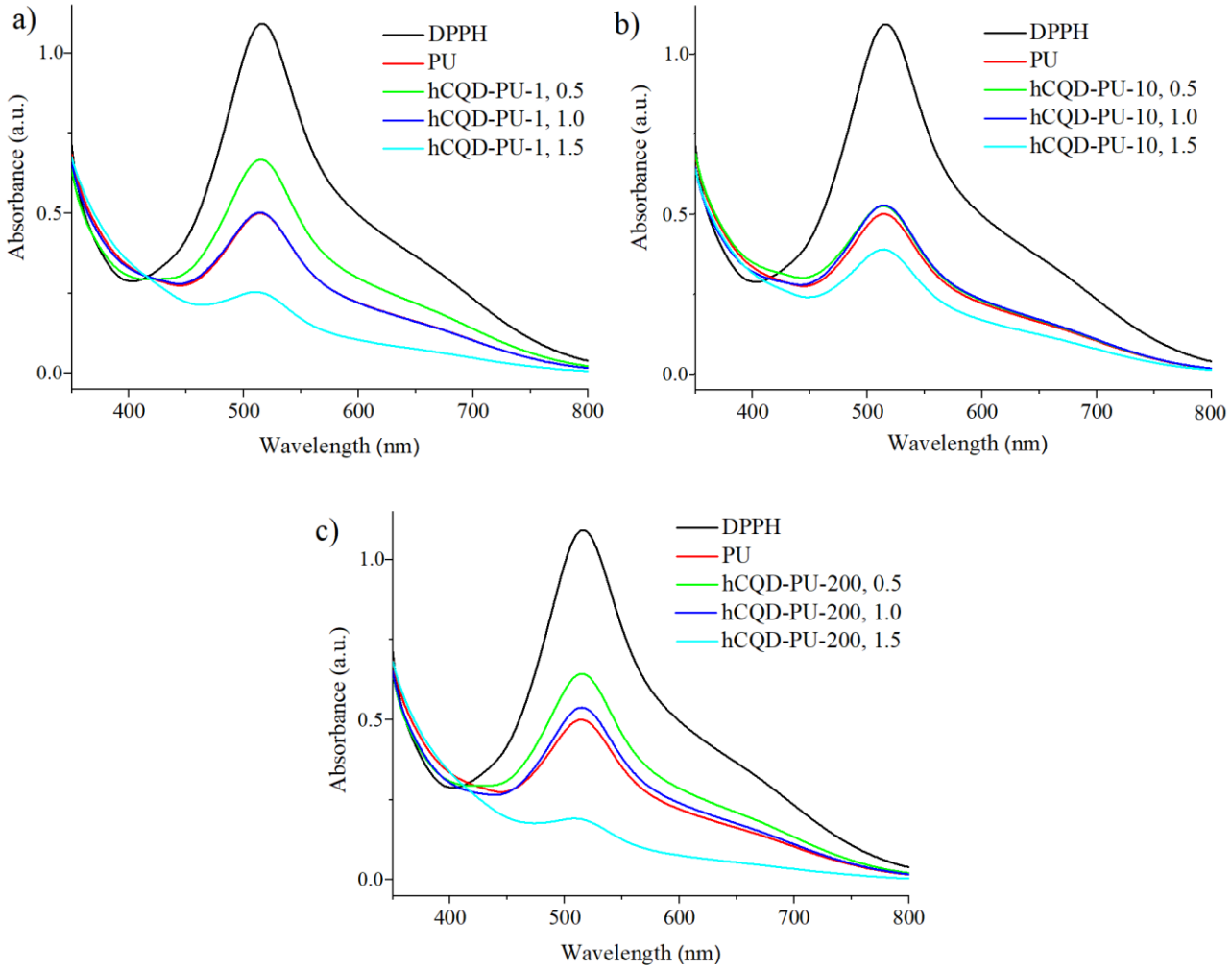

Figure 6.7. UV-vis spectra of DPPH before and after incubation with different sizes of samples: a) hCQD-PU-1, b) hCQD-PU-10, and c) hCQD-PU-200.

To exclude any contribution from DPPH adsorption on hCQD-PU composites in the decrease of UV-vis absorption intensity, we measured UV-vis spectra of the nanocomposites after incubation with DPPH for 1h, and all other conditions remained the same (**Fig. 6.8**). It can be observed that there is no significant absorption at ~520 nm where the main absorption band of DPPH was observed. These results indicate that DPPH adsorption on the hCQD-PU composites is unlikely under our experimental conditions. Thus, it can be concluded that the lowering of this band intensity is due to the conversion of DPPH• into DPPH molecule caused by the antioxidative activity of the nanocomposites.

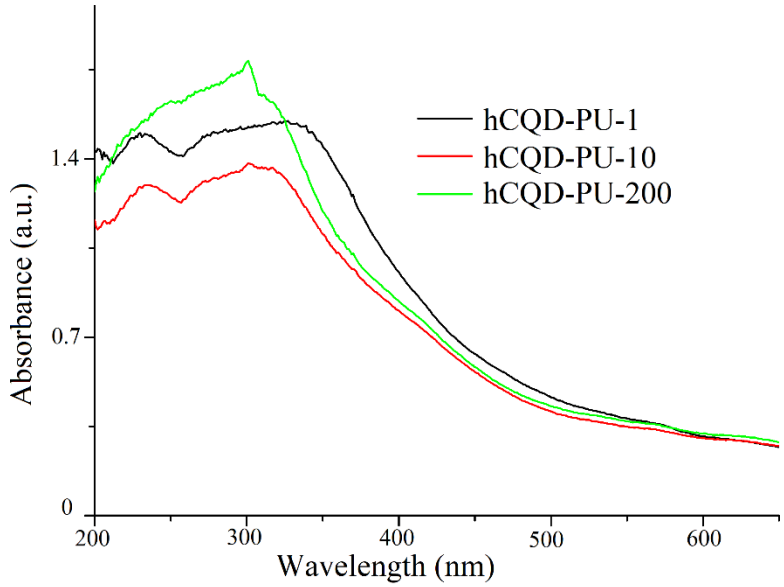

Figure 6.8. UV-vis spectra of hCQD-PU-1 (black curve), hCQD-PU-10 (red curve), hCQD-PU-200 (green curve).

Comparing the nanocomposites of the same size, we can notice that hCQD-PU-200 exhibited the highest ability to convert purple DPPH$^{\bullet}$ into a yellow DPPH molecule. This is in accordance with XPS results, which showed that the content of oxygenated bonds was the highest in hCQD-PU-200 sample and the lowest in hCQD-PU-10 sample. We also calculated the RSA values and these results are summarized in **Table 6.4**.

Table 6.4 Calculated RSA values for irradiated hCQD-PU samples of surface size 1.5 × 1.5 cm^2.

Sample	RSA (%)
hCQD-PU-1	78.77
hCQD-PU-10	66.22
hCQD-PU-200	84.81

Significantly high, dose-depended scavenging activity was registered for all nanocomposites. The highest RSA activity was observed for hCQD-PU-200 at the size of 1.5 × 1.5 cm^2. The lowest RSA activity was detected for hCQD-PU-10 (around 66.22 %).

6.4.2 Production of ˙OH radicals

The results of measurements of photoluminescence in the presence of terephthalic acid are presented in **Fig. 6.9a**. The intensity of the peak attributed to 2-hydroxyterephthalic acid (around 425nm) is known to be proportional to the amount of ˙OH radicals formed. Therefore, we can conclude that the hCQD-PU-200 sample had the highest production of ˙OH radicals, and sample hCQD-PU-10 the lowest (**Fig. 6.9a**).

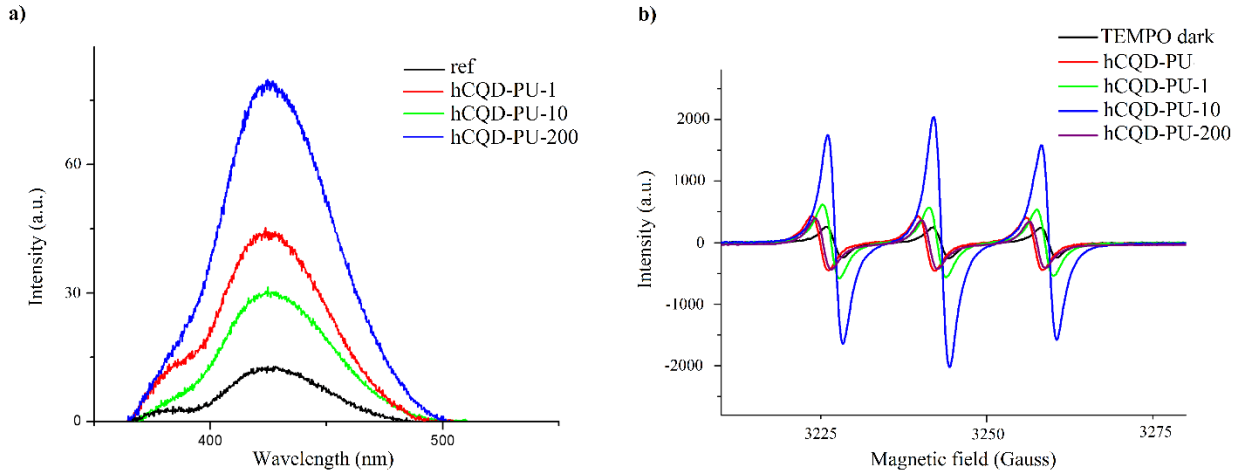

Figure 6.9. a) Production of ˙OH radicals, measured by photoluminescence, for γ-irradiated hCQD-PU nanocomposites, and b) Production of singlet oxygen measured by EPR method of hCQD-PU (red), hCQD-PU-1 (green) and hCQD-PU-10 (blue) and hCQD-PU-200 (purple curve) . Reproduced with permission from [290].

6.4.3 Singlet oxygen production

Previously, in Chapter 1, we described the mechanism of generation of singlet oxygen in typical photosensitizers. However, a group of researchers recently discovered that the mechanism of generation of $^1O_2$ is different in graphene quantum dots (GQDs), from the mechanism present in the conventional photosensitizers. They confirmed that the GQDs can generate much higher quantum yield. According to Ge et al., this process is called a multistate sensitization mechanism [300]. It means that $^1O_2$ can be generated in two pathways: the conventional pathway, which includes the energy transfer from the excited triplet state to the ground state, and the second pathway is the energy transfer from the excited singlet state to the ground state, which also leads to $^1O_2$ generation during the intersystem transitions. Therefore, the overall quantum yield is much higher in GQDs, and it is speculated that it is generated by both, energy transfer and electron transfer pathways [303]. In the recent paper published by our group, it was shown that the mechanism of singlet oxygen production is the same in CQDs like the mechanism of the GQDs presented by Ge et al. [45].

As we mentioned already, we will use two different approaches to determine the singlet oxygen production – Electron paramagnetic resonance and NIR luminescent spectroscopy.

- **Electron paramagnetic resonance – EPR**

EPR analysis was performed in the purpose of examining the ability of hCQD-PU nanocomposites to produce singlet oxygen and to understand the role of gamma irradiation in this process. The samples of gamma-irradiated hCQD-PU nanocomposites were recorded with EPR in the presence of 2,2,6,6-tetramethylpiperidine (TEMP), which is used as a spin trap agent. The

molecules of TEMP selectively react with singlet oxygen ($^1O_2$) and form the stable product 2,2,6,6-tetramethylpiperidine-1-oxyl (TEMPO), which shows a characteristic signal [304,305]. The EPR spectrum of TEMP in the dark does not show any signal. With the addition of hCQD-PU in the TEMP solution, even in dark conditions, a very week signal can be noticed, indicating that TEMPO was formed in a small concentration. However, after illumination for 12 h with blue light, significant changes in the EPR spectra can be noticed. The EPR spectra of gamma-irradiated hCQD-PU samples (**Fig. 6.9b**) consist of three symmetrical signals of Lorentzian shape, from which we can confirm the formation of TEMPO in hCQD-PU nanocomposites. This also confirms their ability to be used as photosensitizers. From the spectra, it can easily be concluded that the sample hCQD-PU-10 has the highest production of singlet oxygen, almost five times stronger than the other two samples. The samples hCQD-PU-200 and hCQD-PU-1 are generating less singlet oxygen, due to the stronger presence of hydroxyl groups, which is confirmed by XPS results.

- **Time-resolved near-infrared luminescence spectroscopy**

Due to the short optical path and increased absorption of hCQDs in the UV region, we used excimer laser (308 nm) for excitation in order to obtain acceptable signal to noise ratio. At this wavelength, also PU matrix partially absorbed UV radiation and therefore, it was used as a blank sample.

The broad transient absorption spectra in **Fig. 6.10a** after excitation correspond to those measured for polyaromatic hydrocarbons [306]. Taking into account the conventional pathway of $O_2(^1\Delta_g)$ formation by energy transfer from the first excited hCQD triplet to the oxygen ground state [300], we searched for transients quenched by oxygen. Our experimental data revealed that the kinetics of transients was complicated and depended on oxygen concentration (**Fig. 6.10b**). The multi-exponential character of the decay kinetics suggests different access pathways of oxygen to the triplet states of hCQD.

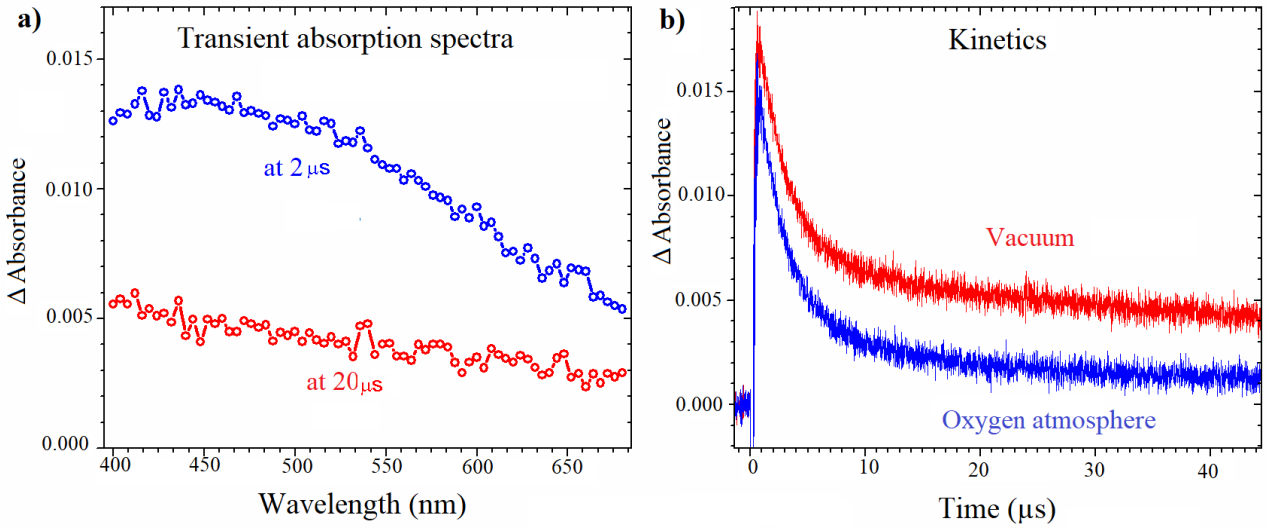

Figure 6.10. Transient absorption spectra at 2 and 20 μs after excitation (308 nm, pulse width of ~28 ns) of non-irradiated hCQD-PU nanocomposite (a) and influence of oxygen on transient kinetics (b).

To separate the influence of the hCQD triplet states quenched by oxygen that are responsible for the formation of $O_2(^1\Delta_g)$, we calculated the difference between transient absorption in vacuum and in the oxygen atmosphere (**Fig. 6.11b**). The difference in kinetics indicates strong quenching of some triplets by oxygen with lifetime τ_T^{oxy} of a few μs (increasing part of the trace) followed by the decay of the hCQD triplet states, which correspond to the lifetime in vacuum (τ_T^{vac}) of several hundred

μs (decreasing part). Simple calculations show that the fraction F_T of the triplet states trapped by oxygen ($F_T = 1- \tau_T^{oxy}/\tau_T^{vac}$) was very high (> 99 %) and indicated effective formation of $O_2(^1\Delta_g)$. The location of such hCQDs is probably nearby the surface of the film. Note that transients formed by irradiation of pure polyurethane film were not quenched by oxygen (**Fig. 6.12**).

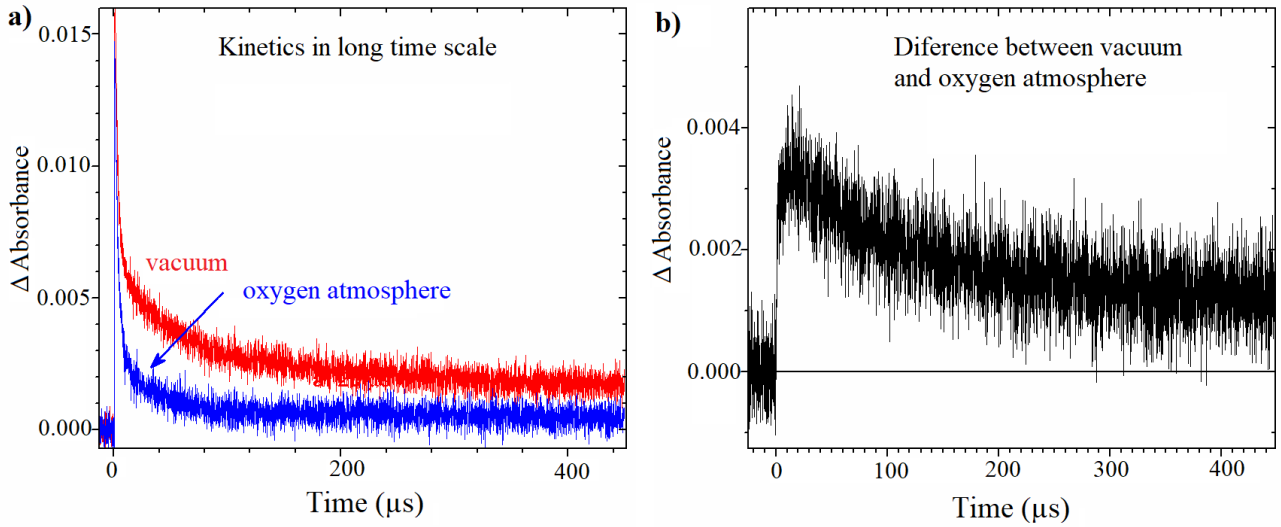

Figure 6.11. The influence of oxygen on transient kinetics (a), and difference between transient absorption in vacuum and oxygen atmosphere (b).

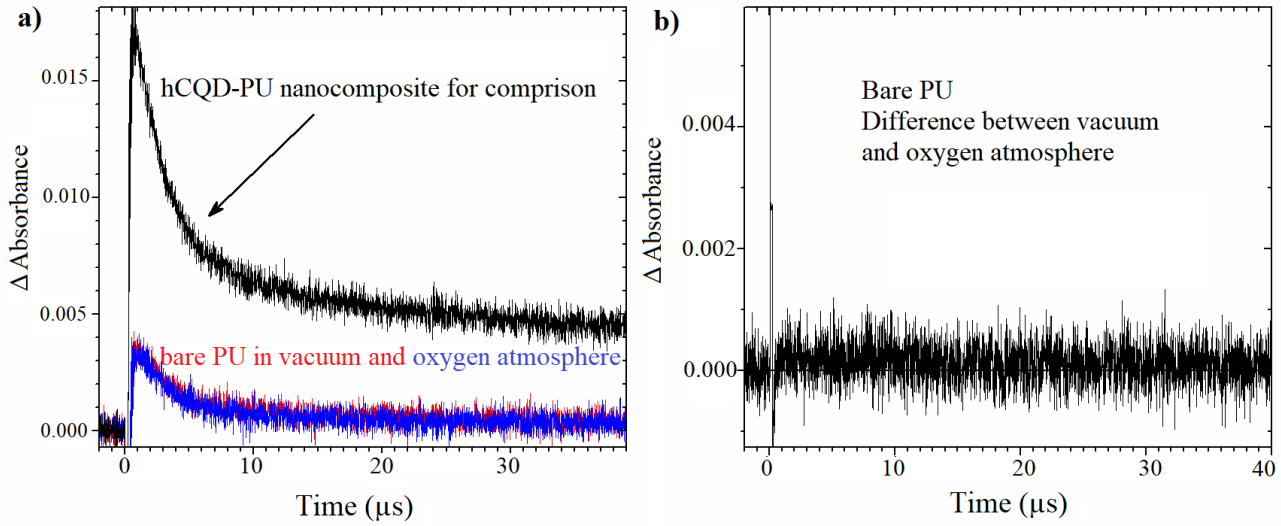

Figure 6.12. Blank experiment: Influence of oxygen on transient kinetics of polyurethane film compared with hCQD-PU nanocomposite (a), and difference between transient absorption of bare PU film in vacuum and oxygen atmosphere (b).

The formation of $O_2(^1\Delta_g)$ was proved by its characteristic NIR luminescence in the oxygen atmosphere. All samples pretreated by γ radiation were compared with original non-irradiated PU with hCQDs (**Fig. 6.13**). The values of τ_Δ (singlet oxygen lifetime) were calculated as single-exponential fits to the exponential data after 5 μs after excitation, where all relevant hCQDs were quenched by oxygen. The calculated lifetimes (τ_Δ ~ 10-11 μs), were not changed with pretreating by different doses of γ radiation within estimated experimental error (~10 %), which is due to inhomogeneities of the film. This value is about 3 times longer than that in H_2O (τ_Δ~3.5 μs) [307].

Thus, the polyurethane matrix is "a reservoir" of $O_2(^1\Delta_g)$, from which $O_2(^1\Delta_g)$ gradually releases for a few tens of microseconds to the environment, where it is deactivated quickly by interaction with H_2O or biological targets (bacteria).

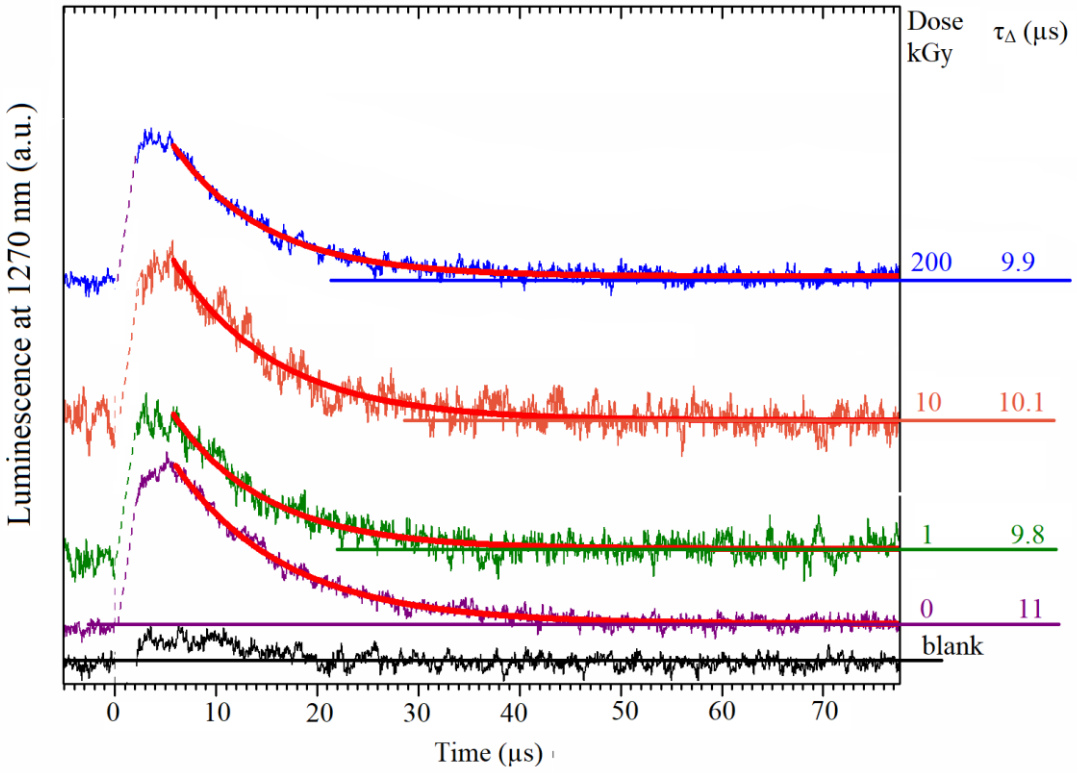

Figure 6.13. Luminescence of $O_2(^1\Delta_g)$ photogenerated by pulse irradiation of γ-irradiated hCQD-PU nanocomposites, calculated as a difference in oxygen atmosphere and in vacuum. Bare PU (black line); hCQD-PU sample (purple); hCQD-PU-1 (green); hCQD-PU-10 (orange); hCQD-PU-200 (blue). Data are offset, the region between 0 - 2 μs is omitted due to strong fluorescence and scattering of hCQDs. Red lines are single exponential fits into experimental data with calculated lifetime τ_Δ of $O_2(^1\Delta_g)$.

The diffusion of $O_2(^1\Delta_g)$ photogenerated inside polyurethane film towards bacteria placed in their aqueous environment controls the antibacterial properties. The mean radial diffusion length of $O_2(^1\Delta_g)$ during time t can be calculated as $l_r = (6\,D(O_2)t)^{1/2}$, where $D(O_2)$ is the coefficient for oxygen diffusion. The distance l_r traveled by $O_2(^1\Delta_g)$ during its lifetime, $\tau_\Delta \sim 10$ μs, and for $D(O_2) = 3.2 \times 10^{-7}$ cm^2/cm^2s^{-1} was only 44 nm in the polyurethane film [308]. This value indicates that only hCQDs in the close proximity of polyurethane surface (several tens of nm) can release $O_2(^1\Delta_g)$, which is able to oxidize biological targets outside the polyurethane film.

For comparison, the length l_r traveled by $O_2(^1\Delta_g)$ in aqueous medium is 205 nm for typical values of $\tau_\Delta = 3.5$ μs and $D(O_2) = 2\times10^{-5}$ cm^2s^{-1} in H_2O. It shows that bacteria (or other biological/chemical species) should be in close contact with surfaces for efficient photooxidation. Some post-processing of hydrophobic surfaces of polymers that may prevent close contact between the surface and target structure may lead to an efficient photooxidation [309].

From the obtained results (**Fig. 6.13**), we can conclude that the singlet oxygen lifetime was nearly the same for all the samples. However, from EPR measurements we presented previously [290] (**Fig. 6.9b**), we could notice that the production of singlet oxygen was the highest for the hCQD-PU-10 sample. This is because these two techniques are quite different. EPR signal reflects only the singlet oxygen which diffused to nanocomposite environment and formed 2,2,6,6-tetramethylpiperidine-1-oxyl (TEMPO). In the method of singlet oxygen detection by NIR luminescence spectroscopy, we

could determine singlet oxygen production of hCQDs in polymer matrix and its decay in both polymer matrix and its environment [235].

6.5 Antimicrobial activity of γ-irradiated hCQD-PU samples under blue light irradiation

Antibacterial tests were performed on two microbe strains: *S. aureus* and *E. coli*, according to ISO 22196 standard. In the first experiment, when the irradiation time was 15 min, the starting concentration of bacteria was 10^6 CFU/cm^2 for *S. aureus* and 2 ×10^6 CFU/cm^2 for *E. coli*. In the second experiment, we lowered the irradiation time to 5 min and the starting concentration of bacteria was 9.4 × 10^6 CFU/cm^2 for *S. aureus* and 1.3 × 10^7 CFU/cm^2 for *E. coli*. Before the pre-treatment with γ irradiation, hCQD-PU exhibited significant antibacterial properties after 60 min of exposure to blue light [284]. However, in our experiment, the good antibacterial activity was exhibited after 15 min, already. The results of antibacterial testing are summarized in **Table 6.5** and presented in **Fig. 6.14** and **6.15**. The number of viable bacteria recovered per cm^2 per test specimen (N) and antibacterial activity (R) is presented in **Table 6.5** for each sample.

Data presented in **Fig. 6.14** and **Fig. 6.15** indicate that gamma-irradiated hCQD-PU nanocomposites have higher efficacy toward both types of tested bacteria strains compared to pure PU and hCQD-PU before gamma irradiation [284]. The PU or the blue light alone had no toxic effects on bacteria [284], which is in accordance with the results that Barneck et al. previously reported, claiming that the light of the wavelength longer than 405 nm has no toxic effect on bacteria [310].

From antibacterial tests, we can conclude that the hCQD-PU-200 had the highest antibacterial efficiency (100%) towards both strains, after only 15 min exposure to the blue light. This is due to the increased production of ROS after the high dose of gamma irradiation, but also due to the increase in surface roughness of the hCQD-PU-200 sample. ROS targets the genetic material of the microorganisms, such as DNA, which finally results in the microbial cell death [311]. Although the singlet oxygen generation was the same in all the samples, the production of •OH radicals, and the overall radical scavenging activity was the highest for the hCQD-PU-200 sample, which resulted in higher antibacterial efficiency. Cho et al. proved that the role of •OH radicals in the inactivation of *E. coli* was dominant among all the ROS [312]. However, the lifetime of •OH radicals is very short [313], so only those hCQDs in the close proximity to the surface of PU could participate in the antibacterial effect. This is in accordance with our antibacterial results showing (**Table 6.5**) that the inactivation of *E. coli* (R (hCQD-PU-200) > R (hCQD-PU-1) > R (hCQD-PU-10)) exhibited the same trend as the production of •OH radicals (**Fig. 6.9a**). Additionally, the antibacterial activity was higher towards Gram-negative bacteria, probably because *S. aureus* has the ability to adapt to oxidative stress by forming small colony variants that are resistant to ROS [314]. From the second experiment when the time was lowered to 5 min, we could notice the antibacterial efficiency only for the hCQD-PU-200 sample (38% for *S. aureus* and 59% for *E. coli*).

Table 6.5 Antibacterial activity and the number of viable bacteria recovered per cm^2 per test specimen.

Sample	**Time of exposure to the blue light (15 W) (min)**	***S. aureus***		***E. coli***	
		N (cfu/cm^2)	**$R = U_t - A_t$**	**N (cfu/cm^2)**	**$R = U_t - A_t$**
PU	15	8×10^5	**$U_t = 5.5$**	1.5×10^6	**$U_t = 6$**
hCQD-PU [284]	30	2.4×10^4	**1.1**	5.5×10^4	**1.4**
hCQD-PU-1	15	4.8×10^3	**1.8**	3.4	**5.5**
hCQD-PU-10	15	250	**3.1**	27.2	**4.6**
hCQD-PU-200	15	0	**≥ 5.5**	0	**≥ 6**
PU	5	3.4×10^5	**$U_t = 5.5$**	2.6×10^6	**$U_t = 6.4$**
hCQD-PU-1	5	2×10^5	**0.2**	2.4×10^6	**0.1**
hCQD-PU-10	5	6.7×10^5	**0**	2.4×10^6	**0.1**
hCQD-PU-200	5	2.9×10^3	**2.1**	4.9×10^2	**3.8**

$N = (100 \times C \times D \times V) / A$

$R = U_t - A_t$
R – the antibacterial activity
C – the average plate count for the duplicate plates
D – the dilution factor for the plates counted
V – the volume, in mL, of SCDLP added to the specimen (V = 2,5 ml)
A – the surface area, in mm^2, of the cover film (A= 400 mm^2)
N – the number of viable bacteria recovered per cm^2 per test specimen
U_t – the average of the common logarithm of the number of viable bacteria, in cells/cm^2, recovered from the untreated test specimens after 24 h
A_t – the average of the common logarithm of the number of viable bacteria (cells/cm2) recovered from the treated test specimens after 24 h

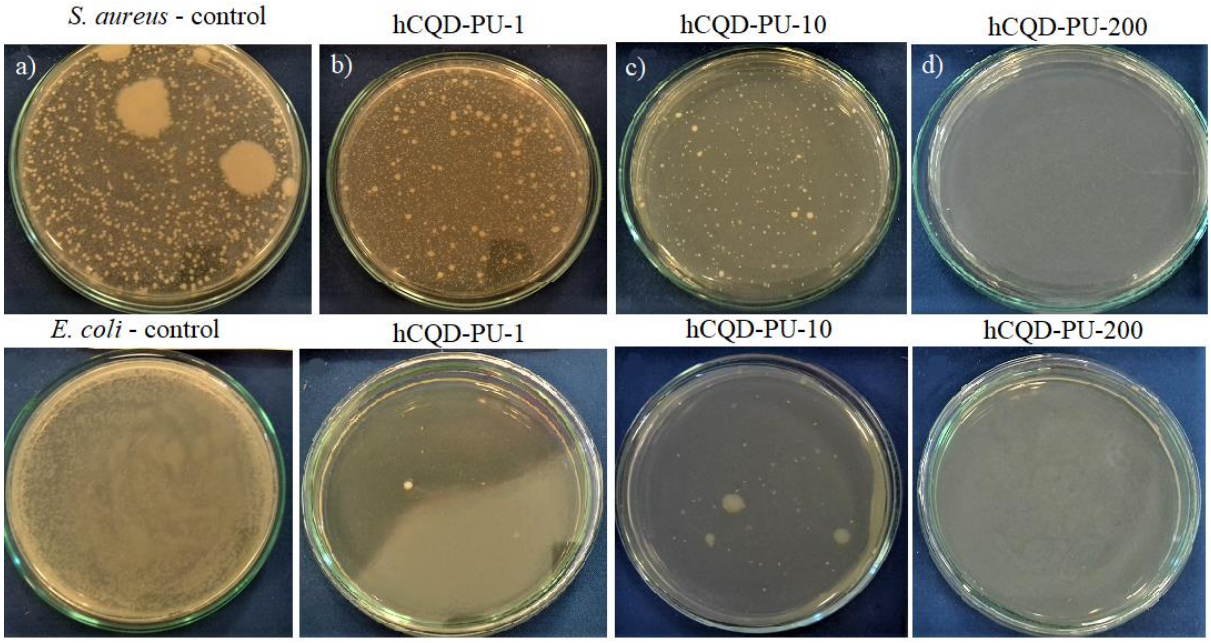

Figure 6.14. Optical images of *S. aureus* and *E. coli* collected from the surface of a) PU, b) hCQD-PU-1, c) hCQD-PU-10 and d) hCQD-PU-200 nanocomposites after 15 min of exposure to blue light.

Upon exposure to the blue light, the hCQDs encapsulated closer to the surface of the polymer matrix produce ROS, that are diffusing from the polymer matrix and destroying the bacteria cell membranes. After gamma irradiation, the production of ROS increased, but also the surface roughness and wetting properties of samples have changed. Samples with higher surface roughness exhibit also bigger diffusion channels [235]. We suppose that these changes allowed the increase of the diffusion of ROS through the polymer matrix and a closer exposure of microbes to ROS. Unlike other photosensitizers, which very often need to be triggered by UV light, hCQDs produce ROS whenever they are exposed to visible blue light, and additionally, they are resistant to photobleaching. These properties make gamma-irradiated hCQD-PU nanocomposites a very promising antibacterial material.

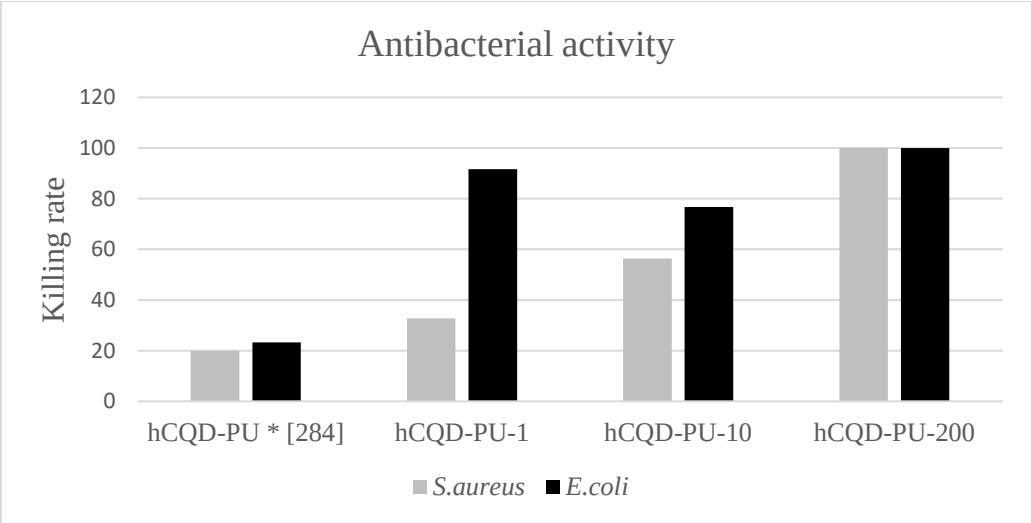

Figure 6.15. Antibacterial activity of gamma-irradiated samples after 15 min of exposure to the blue lamp (15 W). Values for the non-irradiated hCQD-PU sample was taken from the ref. [284], and it is the value of antibacterial activity after 30 min.

6.6 Biocompatibility study

6.6.1 Cytotoxicity study of released extracts

One of the most important requirements of any material with application in medicine or biotechnology is low toxicity. The viability studies of pure PU, gamma irradiated pure PU (PU-200) and gamma irradiated hCQD-PU samples, were conducted over two different cell lines HeLa and U87MG. **Figure 6.16** presents cell viability of individual samples in various extract concentrations. As can be seen from the figure, none of the tested samples did not show cytotoxicity toward HeLa cells, regardless to the extract concentration (**Fig. 6.16a)**. However, for U87MG cells, only the hCQD-PU-200 sample exhibited a mild or moderate toxicity, and only when extract concentrations were 75 and 100%, respectively (**Fig. 6.16b**). It should be noted that U87MG cells are generally more sensitive than HeLa cells. These results are in accordance with the previously published results by our group for polymer nanocomposites with incorporated hCQDs [235,284].

Additionally, these results indicate that the pure PU after gamma pre-treatment (PU-200) did not exhibit cytotoxicity to any type of cells, confirming that the toxicity towards bacteria comes from the photodynamic effect of the incorporated hCQDs.

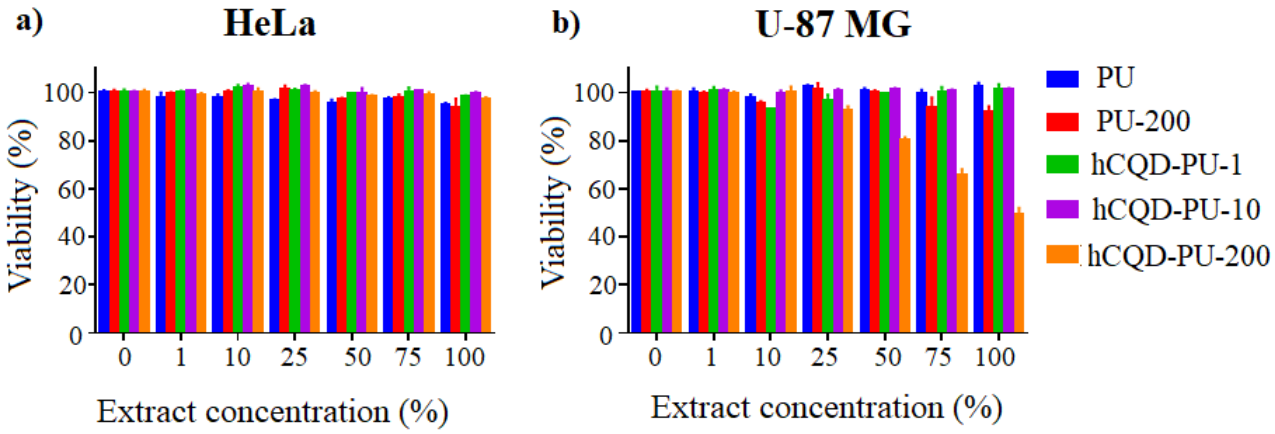

Figure 6.16. Cell viability of different samples in various extract concentrations towards a) HeLa cells, and b) U-87 MG cells.

6.6.2 Cell proliferation and growth

For any bio-interface, another important characteristic is the ability of cells to attach, grow and proliferate. The cell adhesion to a surface is a very complex process that includes three phases: the protein adsorption (it takes place after the material surface comes into contact with biological fluids), the attachment and the adhesion phase. Similarly as in the bacteria attachment, the surface roughness is also very important in the cell attachment mechanism [315].

Figure 6.17 presents the viable fraction of adherent cells that can grow directly on different surfaces. Treated polystyrene (PS) surfaces (Nunclon™ Delta) were used as a reference. The results show that both cell lines also grow similarly on glass slides under the same conditions. Besides that, only a fraction of cells is able to adhere and proliferate on pure polyurethane surfaces during 48 h (around 60% and 20% for HeLa and U-87 MG, respectively). For all other gamma-treated surfaces with or without hCQDs, only 30% and 20% of HeLa and U-87 MG cells are able to grow on these surfaces, respectively. In order to confirm these results, the experiments were repeated and the cells were fixed and visualized under fluorescence microscopy (**Fig. 6.18** and **6.19**). In a previous study

published by our group it was shown that hCQD-PU nanocomposites show resistivity against the attachment and proliferation of *eukaryotic* cells [284], and in this study we obtained similar results, regardless to the gamma pre-treatment.

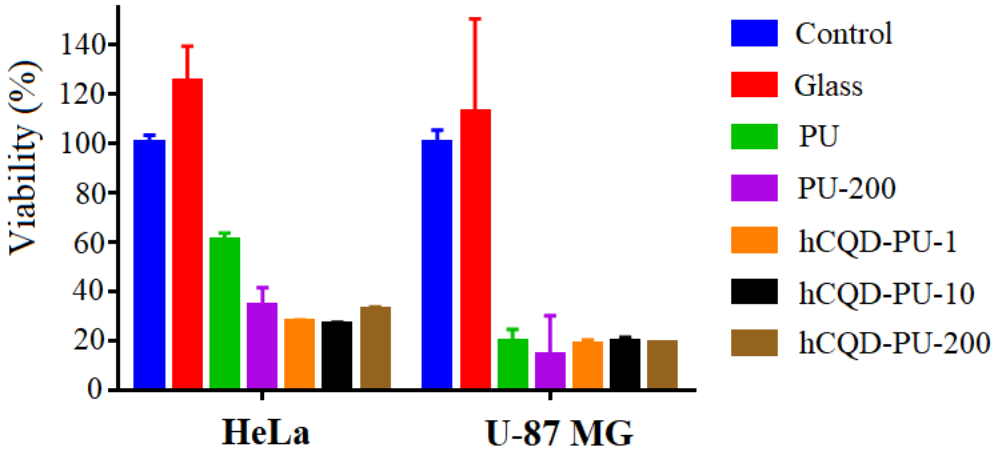

Figure 6.17. The viability after 48 h of HeLa and U-87 MG cells directly seeded on: Polystyrene (PS, control) as a reference; glass; pure polyurethane (PU); polyurethane irradiated by 200 kGy (PU-200), and samples hCQD-PU-1, hCQD-PU-10 and hCQD-PU-200, respectively.

The fluorescence microscopy images confirmed that even on the pure PU, cells were not able to grow homogenously, we can notice that they formed clusters and spheroids (**Fig. 6.18** and **6.19**).

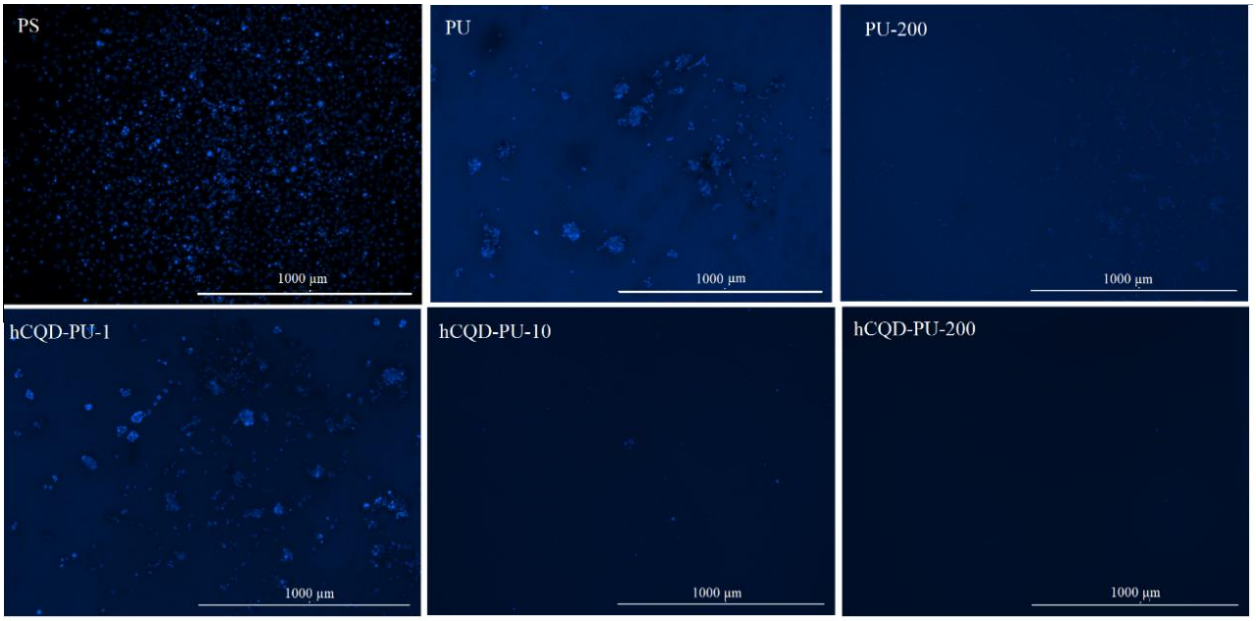

Figure 6.18 The growth of HeLa cells after 48 h on: Polystyrene (PS) as a reference; pure polyurethane - PU; polyurethane irradiated by 200 kGy (PU-200), and samples hCQD-PU-1, hCQD-PU-10 and hCQD-PU-200, respectively.

From these results we can conclude that gamma irradiation pre-treatment by increasing the production of ROS significantly improved material's toxicity towards *prokaryotic* cells, while it did not influence the toxicity towards *eukaryotic* cells.

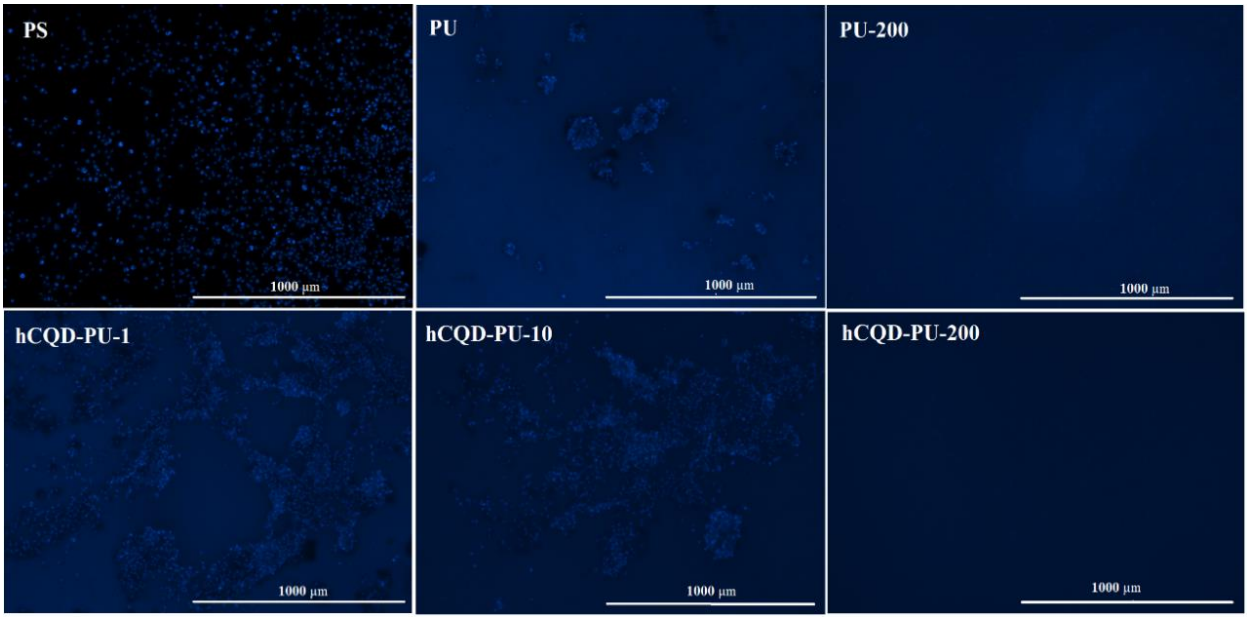

Figure 6.19 The growth of U87MG cells after 48 h on: Polystyrene (PS) as a reference; pure polyurethane - PU; polyurethane irradiated by 200kGy (PU-200), and samples hCQD-PU-1, hCQD-PU-10 and hCQD-PU-200, respectively.

Depending on the application of a bio-interface, the cell attachment can be either desirable or undesirable property. When designing bone implants, for example, it is desirable for cells to easily attach and grow on the surface of an implant. On the contrary, biomaterials that have to interact with blood are required not to be adherent to cells [316].

6.7 Conclusion

In this chapter, we demonstrated a successful and cost-effective preparation method of hCQD-PU nanocomposites and the influence of gamma irradiation pre-treatment on their physical, chemical, and antibacterial properties. The results showed that gamma-irradiation pre-treatment of hCQD-PU nanocomposites led to changes in the surface roughness and contact angle but the mechanical stability of nanocomposites was not significantly influenced by the gamma irradiation. Additionally, we concluded that all the samples exhibited photoluminescence (PL), but gamma irradiation had an influence on their PL properties; the PL intensity increased with the increase of the dose of gamma irradiation. Also, we proved that the radical scavenging activity and the production of $^{\bullet}OH$ radicals were the highest in hCQD-PU-200 sample and lowest for hCQD-PU-10 sample. Additionally, the percentage of sp^2 groups significantly increased with the increase of the irradiation dose. Therefore, we can conclude that gamma irradiation did have a significant influence on the chemical properties of nanocomposites. Consequently, it significantly improved the antibacterial activity of gamma-irradiated nanocomposites, compared to the same nanocomposite before the pre-treatment [284]. Our work demonstrated that gamma-irradiated hCQD-PU nanocomposites could efficiently scavenge free radicals under the ambient conditions, and therefore

display antioxidative properties, while under blue light irradiation the nanocomposites exhibited prooxidative behavior. The hCQD-PU-200 nanocomposite exhibited excellent antibacterial properties after 15 min of exposure to a blue lamp and significant antibacterial activity after only 5 min. This is due to enhanced ROS production and increased diffusion of ROS through the polymer matrix. From antibacterial tests on the other two irradiated samples (hCQD-PU-1 and hCQD-PU-10), we could conclude that the antibacterial activity was higher towards Gram-negative than Gram-positive bacteria. Additionally, the cell proliferation tests showed that all the samples had low cell proliferation or growing, regardless to the irradiation dose. This is an important property in the design of certain bio-interfaces where cell adhesion can induce pathological effects. Viability tests proved that only the hCQD-PU-200 sample exhibited mild cytotoxicity towards U87MG cell line, and only when the extract concentration was 75 and 100%, while none of the samples exhibited toxic effects towards HeLa cells. Fast and efficient antibacterial activity (that is triggered by visible light) and low toxicity, might make gamma-irradiated hCQD-PU nanocomposites excellent candidates for various antibacterial surfaces and bio-interfaces.

Chapter 7: Conclusion

In the era of increasing antimicrobial resistance and growing concerns of mortality rate due to bacterial infections, it is highly important to apply multidisciplinary approaches to reduce or inhibit bacterial infections. The application of nanotechnology principles to medicine combines two large cross-disciplinary areas with a groundbreaking potential.

The goal of this thesis was to design and synthesise novel and efficient antibacterial materials in the form of carbon-polymer nanocomposites (K/Au NH/rGO-PEI and hCQD-PU). Both nanocomposites were exposed to certain form of electromagnetic irradiation. In the first experiment, we used NIR laser irradiation to trigger the photothermal effect, and in the second experiment we used gamma irradiation to modify the hCQD-PU nanocomposites, and improve the photodynamic effect. By using these alternative antimicrobial approaches such as PDT and PTT, we can prevent bacteria from developing resistance, which is today the most important feature. Additionally, the ability of destroying a mature biofilm grown on a surface is a very desirable property of every antibacterial material, and we achieved this by K/Au NH/rGO-PEI nanocomposite.

The main contribution given by this doctoral thesis is the multidisciplinary approach to designing novel antibacterial materials, and methods of their modification with the purpose of changing and improving their properties. Here, we combined material engineering, chemistry, physics and microbiology, in order to obtain the desired results, successfully. There are still many improvements that could be done, of course, in terms of simplicity of design, lowering the cost and improving the efficiency, but the designed materials have potential in real-life applications.

References

[1] Hajipour MJ, Fromm KM, Akbar Ashkarran A, Jimenez de Aberasturi D, Larramendi IR de, Rojo T, et al. Antibacterial properties of nanoparticles. Trends Biotechnol 2012;30:499–511. doi:10.1016/J.TIBTECH.2012.06.004.

[2] Kashef N, Huang Y-Y, Hamblin MR. Advances in antimicrobial photodynamic inactivation at the nanoscale. Nanophotonics 2017;6:853–79. doi:10.1515/nanoph-2016-0189.

[3] Tuberculosis n.d. https://www.who.int/en/news-room/fact-sheets/detail/tuberculosis (accessed December 27, 2019).

[4] Davies J, Davies D. Origins and Evolution of Antibiotic Resistance. Microbiol Mol Biol Rev 2010;74.

[5] Liu B, Pop M. ARDB - Antibiotic resistance genes database. Nucleic Acids Res 2009;37. doi:10.1093/nar/gkn656.

[6] Bush K, Courvalin P, Dantas G, Davies J, Eisenstein B, Huovinen P, et al. Tackling antibiotic resistance. Nat Rev Microbiol 2011;9:894–6. doi:10.1038/nrmicro2693.

[7] Bartoloni A, Pallecchi L, Rodríguez H, Fernandez C, Mantella A, Bartalesi F, et al. Antibiotic resistance in a very remote Amazonas community. Int J Antimicrob Agents 2009;33:125–9. doi:10.1016/j.ijantimicag.2008.07.029.

[8] Pallecchi L, Bartoloni A, Paradisi F, Rossolini GM. Antibiotic resistance in the absence of antimicrobial use: Mechanisms and implications. Expert Rev Anti Infect Ther 2008;6:725–32. doi:10.1586/14787210.6.5.725.

[9] Montana State University. Biofilm basics: Section 1 - Center for Biofilm Engineering | Montana State University. CBE Resour 2003:2. http://www.biofilm.montana.edu/biofilm-basics/what_are_biofilms.html (accessed January 10, 2020).

[10] Armentano I, Arciola CR, Fortunati E, Ferrari D, Mattioli S, Amoroso CF, et al. The Interaction of Bacteria with Engineered Nanostructured Polymeric Materials: A Review 2014. doi:10.1155/2014/410423.

[11] Ribeiro M, Monteiro FJ, Ferraz MP. Infection of orthopedic implants with emphasis on bacterial adhesion process and techniques used in studying bacterial-material interactions. Biomatter 2012;2:176–94. doi:10.4161/biom.22905.

[12] Gottenbos B, Busscher HJ, Van Der Mei HC, Nieuwenhuis P. Pathogenesis and prevention of biomaterial centered infections. J Mater Sci Mater Med 2002;13:717–22. doi:10.1023/A:1016175502756.

[13] Costerton JW, Stewart PS, Greenberg EP. Bacterial biofilms: A common cause of persistent infections. Science 1999;284:1318–22. doi:10.1126/science.284.5418.1318.

[14] Lewis K. Persister cells: Molecular mechanisms related to antibiotic tolerance. Handb Exp Pharmacol 2012;211:121–33. doi:10.1007/978-3-642-28951-4-8.

[15] Zarb P, Coignard B, Griskeviciene J, Muller A, Vankerckhoven V, Weist K, et al. The european centre for disease prevention and control (ECDC) pilot point prevalence survey of healthcare-associated infections and antimicrobial use. Eurosurveillance 2012;17:1–16. doi:10.2807/ese.17.46.20316-en.

[16] Cloutier M, Mantovani D, Rosei F. Antibacterial Coatings: Challenges, Perspectives, and Opportunities. Trends Biotechnol 2015;33:637–52. doi:10.1016/j.tibtech.2015.09.002.

[17] Peleg AY, Hooper DC. Hospital-acquired infections due to gram-negative bacteria. N Engl J Med 2010;362:1804–13. doi:10.1056/NEJMra0904124.

[18] Allegranzi B, Nejad SB, Combescure C, Graafmans W, Attar H, Donaldson L, et al. Burden of endemic health-care-associated infection in developing countries: Systematic review and meta-analysis. Lancet 2011;377:228–41. doi:10.1016/S0140-6736(10)61458-4.

[19] Levy SB, Bonnie M. Antibacterial resistance worldwide: Causes, challenges and responses. Nat Med 2004;10:S122–9. doi:10.1038/nm1145.

[20] Hasan J, Crawford RJ, Ivanova EP. Antibacterial surfaces: The quest for a new generation of biomaterials. Trends Biotechnol 2013;31:295–304. doi:10.1016/j.tibtech.2013.01.017.

[21] Elbourne A, Crawford RJ, Ivanova EP. Nano-structured antimicrobial surfaces: From nature to synthetic analogues. J Colloid Interface Sci 2017;508:603–16. doi:10.1016/j.jcis.2017.07.021.

[22] Cotruvo JA. 2017 WHO Guidelines for Drinking Water Quality: First Addendum to the Fourth Edition. J Am Water Works Assoc 2017;109:44–51. doi:10.5942/jawwa.2017.109.0087.

[23] World Health Organization. Guidelines for Drinking-Water Quality: Fourth Edition Incorporating the First Addendum. 2014.

[24] Magill SS, O'Leary E, Janelle SJ, Thompson DL, Dumyati G, Nadle J, et al. Changes in prevalence of health care-associated infections in U.S. Hospitals. N Engl J Med 2018;379:1732–44. doi:10.1056/NEJMoa1801550.

[25] Xiu ZM, Ma J, Alvarez PJJ. Differential effect of common ligands and molecular oxygen on antimicrobial activity of silver nanoparticles versus silver ions. Environ Sci Technol 2011;45:9003–8. doi:10.1021/es201918f.

[26] Liau SY, Read DC, Pugh WJ, Furr JR, Russell AD. Interaction of silver nitrate with readily identifiable groups: relationship to the antibacterialaction of silver ions. Lett Appl Microbiol 1997;25:279–83. doi:10.1046/j.1472-765X.1997.00219.x.

[27] Q.L. Feng, J. Wu, G.Q. Chen, F.Z. Cui, T.M. Kim JOK. A mechanistic study of the antibacterial effect of silver ions on E. coli and S. aureus. J Biomed Mater Res 2000;52:662–8. doi:doi.org/10.1002/1097-4636(20001215)52:4<662::AID-JBM10>3.0.CO;2-3.

[28] Kim JS, Kuk E, Yu KN, Kim J-H, Park SJ, Lee HJ, et al. Antimicrobial effects of silver nanoparticles. Nanomedicine Nanotechnology, Biol Med 2007;3:95–101. doi:10.1016/j.nano.2006.12.001.

[29] Egger S, Lehmann RP, Height MJ, Loessner MJ, Schuppler M. Antimicrobial Properties of a Novel Silver-Silica Nanocomposite Material; ; Applied and environmental microbiology; Appl Environ Microbiol 2009;75:2973–6.

[30] Das SK, Das AR, Guha AK. Gold Nanoparticles: Microbial Synthesis and Application in Water Hygiene Management. Langmuir 2009;25:8192–9. doi:10.1021/la900585p.

[31] Ramdayal, Balasubramanian K. Antibacterial application of polyvinylalcohol-nanogold composite membranes. Colloids Surf A Physicochem Eng Asp 2014;455:174–8.

doi:10.1016/j.colsurfa.2014.04.050.

[32] Jiang W, Mashayekhi H, Xing B. Bacterial toxicity comparison between nano- and micro-scaled oxide particles. Environ Pollut 2009;157:1619–25. doi:10.1016/J.ENVPOL.2008.12.025.

[33] Adams LK, Lyon DY, Alvarez PJJ. Comparative eco-toxicity of nanoscale TiO2, SiO2, and ZnO water suspensions. Water Res 2006;40:3527–32. doi:10.1016/J.WATRES.2006.08.004.

[34] Shi L-E, Xing L, Hou B, Ge H, Guo X, Tang Z. Inorganic nano mental oxides used as anti-microorganism agents for pathogen control. Curr Res Technol Educ Top Appl Microbiol Microb Biotechnol 2010:361–8.

[35] Matsunaga T, Tomoda R, Nakajima T, Nakamura N, Komine T. Continuous-sterilization system that uses photosemiconductor powders. Appl Environ Microbiol 1988;54:1330–3.

[36] Kühn KP, Chaberny IF, Massholder K, Stickler M, Benz VW, Sonntag H-G, et al. Disinfection of surfaces by photocatalytic oxidation with titanium dioxide and UVA light. Chemosphere 2003;53:71–7. doi:10.1016/S0045-6535(03)00362-X.

[37] Coleman HM, Marquis CP, Scott JA, Chin S-S, Amal R. Bactericidal effects of titanium dioxide-based photocatalysts. Chem Eng J 2005;113:55–63. doi:10.1016/J.CEJ.2005.07.015.

[38] Fagan R, McCormack DE, Dionysiou DD, Pillai SC. A review of solar and visible light active TiO2 photocatalysis for treating bacteria, cyanotoxins and contaminants of emerging concern. Mater Sci Semicond Process 2016;42:2–14. doi:10.1016/J.MSSP.2015.07.052.

[39] Stoimenov PK, Klinger RL, Marchin GL, Klabunde KJ. Metal oxide nanoparticles as bactericidal agents. Langmuir 2002;18:6679–86. doi:10.1021/la0202374.

[40] Heinlaan M, Ivask A, Blinova I, Dubourguier H-C, Kahru A. Toxicity of nanosized and bulk ZnO, CuO and TiO2 to bacteria Vibrio fischeri and crustaceans Daphnia magna and Thamnocephalus platyurus. Chemosphere 2008;71:1308–16. doi:10.1016/J.CHEMOSPHERE.2007.11.047.

[41] Bogdanović U, Lazić V, Vodnik V, Budimir M, Marković Z, Dimitrijević S. Copper nanoparticles with high antimicrobial activity. Mater Lett 2014;128:75–8. doi:10.1016/j.matlet.2014.04.106.

[42] Qi L, Xu Z, Jiang X, Hu C, Zou X. Preparation and antibacterial activity of chitosan nanoparticles. Carbohydr Res 2004;339:2693–700. doi:10.1016/J.CARRES.2004.09.007.

[43] Szunerits S, Boukherroub R. Antibacterial activity of graphene-based materials. J Mater Chem B 2016;4:6892–912. doi:10.1039/c6tb01647b.

[44] Maas M. Carbon nanomaterials as antibacterial colloids. Materials (Basel) 2016;9. doi:10.3390/ma9080617.

[45] Marković ZM, Jovanović SP, Mašković PZ, Danko M, Mičušík M, Pavlović VB, et al. Photo-induced antibacterial activity of four graphene based nanomaterials on a wide range of bacteria. RSC Adv 2018;8:31337–47. doi:10.1039/C8RA04664F.

[46] Wang L, Hu C, Shao L. The antimicrobial activity of nanoparticles: Present situation and prospects for the future. Int J Nanomedicine 2017;12:1227–49. doi:10.2147/IJN.S121956.

[47] Johnston HJ, Hutchison G, Christensen FM, Peters S, Hankin S, Stone V. A review of the in

vivo and in vitro toxicity of silver and gold particulates: Particle attributes and biological mechanisms responsible for the observed toxicity. Crit Rev Toxicol 2010;40:328–46. doi:10.3109/10408440903453074.

[48] Li Q, Mahendra S, Lyon DY, Brunet L, Liga M V., Li D, et al. Antimicrobial nanomaterials for water disinfection and microbial control: Potential applications and implications. Water Res 2008;42:4591–602. doi:10.1016/j.watres.2008.08.015.

[49] Cho M, Chung H, Choi W, Yoon J, Marti E, Variatza E, et al. Silver nanoparticle-alginate composite beads for point-of-use drinking water disinfection. Trends Microbiol 2014;22:25–9. doi:10.1016/j.coche.2013.09.004.

[50] Anghel I, Grumezescu AM, Holban AM, Ficai A, Anghel AG, Chifiriuc MC. Biohybrid nanostructured iron oxide nanoparticles and Satureja hortensis to prevent fungal biofilm development. Int J Mol Sci 2013;14:18110–23. doi:10.3390/ijms140918110.

[51] De Gisi S, Lofrano G, Grassi M, Notarnicola M. Characteristics and adsorption capacities of low-cost sorbents for wastewater treatment: A review. Sustain Mater Technol 2016;9:10–40. doi:10.1016/j.susmat.2016.06.002.

[52] Dale AL, Casman EA, Lowry G V., Lead JR, Viparelli E, Baalousha M. Modeling Nanomaterial Environmental Fate in Aquatic Systems. Environ Sci Technol 2015;49:2587–93. doi:10.1021/es505076w.

[53] Zhang Y, Wu B, Xu H, Liu H, Wang M, He Y, et al. Nanomaterials-enabled water and wastewater treatment. NanoImpact 2016;3–4:22–39. doi:10.1016/j.impact.2016.09.004.

[54] Tesh SJ, Scott TB. Nano-Composites for Water Remediation: A Review. Adv Mater 2014;26:6056–68. doi:10.1002/adma.201401376.

[55] Sile-Yuksel M, Tas B, Koseoglu-Imer DY, Koyuncu I. Effect of silver nanoparticle (AgNP) location in nanocomposite membrane matrix fabricated with different polymer type on antibacterial mechanism. Desalination 2014;347:120–30. doi:10.1016/J.DESAL.2014.05.022.

[56] Sirelkhatim A, Mahmud S, Seeni A, Haida N, Kaus M, Chuo L, et al. Review on Zinc Oxide Nanoparticles: Antibacterial Activity and Toxicity Mechanism. Nano-Micro Lett 2015;7:219–42. doi:10.1007/s40820-015-0040-x.

[57] Carp O, Huisman CL, Reller A. Photoinduced reactivity of titanium dioxide. Prog Solid State Chem 2004;32:33–177. doi:10.1016/J.PROGSOLIDSTCHEM.2004.08.001.

[58] Cui Y, Zhao Y, Tian Y, Zhang W, Lü X, Jiang X. The molecular mechanism of action of bactericidal gold nanoparticles on Escherichia coli. Biomaterials 2012;33:2327–33. doi:10.1016/j.biomaterials.2011.11.057.

[59] Perni S, Piccirillo C, Pratten J, Prokopovich P, Chrzanowski W, Parkin IP, et al. The antimicrobial properties of light-activated polymers containing methylene blue and gold nanoparticles. Biomaterials 2009;30:89–93. doi:10.1016/j.biomaterials.2008.09.020.

[60] Tiller JC, Liao CJ, Lewis K, Klibanov AM. Designing surfaces that kill bacteria on contact. Proc Natl Acad Sci U S A 2001;98:5981–5. doi:10.1073/pnas.111143098.

[61] Song J, Jang J. Antimicrobial polymer nanostructures: Synthetic route, mechanism of action and perspective. Adv Colloid Interface Sci 2014;203:37–50. doi:10.1016/j.cis.2013.11.007.

[62] Norowski PA, Bumgardner JD. Biomaterial and antibiotic strategies for peri-implantitis. J Biomed Mater Res - Part B Appl Biomater 2009;88:530–43. doi:10.1002/jbm.b.31152.

[63] Gao G, Lange D, Hilpert K, Kindrachuk J, Zou Y, Cheng JTJ, et al. The biocompatibility and biofilm resistance of implant coatings based on hydrophilic polymer brushes conjugated with antimicrobial peptides. Biomaterials 2011;32:3899–909. doi:10.1016/j.biomaterials.2011.02.013.

[64] Moan J, Peng Q. An outline of the history of PDT. Photodyn. Ther., 2007, p. 1–18. doi:10.1039/9781847551658-00001.

[65] Abrahamse H, Hamblin MR. New photosensitizers for photodynamic therapy. Biochem J 2016;473:347–64. doi:10.1042/BJ20150942.

[66] Dougherty TJ, Grindey GB, Fiel R, Weishaupt KR, Boyle DG. Photoradiation Therapy. II. Cure of Animal Tumors With Hematoporphyrin and Light23. JNCI J Natl Cancer Inst 1975;55:115–21. doi:10.1093/jnci/55.1.115.

[67] US6835202B2 - Apparatus and method for high energy photodynamic therapy of acne vulgaris and seborrhea - Google Patents n.d. https://patents.google.com/patent/US6835202B2/en (accessed January 19, 2020).

[68] Nybaek H, Jemec GBE. Photodynamic Therapy in the Treatment of Rosacea. Dermatology 2005;211:135–8. doi:10.1159/000086443.

[69] Tandon YK, Yang MF, Baron ED. Role of photodynamic therapy in psoriasis: a brief review. Photodermatol Photoimmunol Photomed 2008;24:222–30. doi:10.1111/j.1600-0781.2008.00376.x.

[70] Polansky R, Haas M, Heschl A, Wimmer G. Clinical effectiveness of photodynamic therapy in the treatment of periodontitis. J Clin Periodontol 2009;36:575–80. doi:10.1111/j.1600-051X.2009.01412.x.

[71] Bressler NM, Bressler SB. Photodynamic therapy with verteporfin (Visudyne): Impact on ophthalmology and visual sciences. Investig Ophthalmol Vis Sci 2000;41:624–8.

[72] Hamblin MR, Viveiros J, Yang C, Ahmadi A, Ganz RA, Tolkoff MJ. Helicobacter pylori accumulates photoactive porphyrins and is killed by visible light. Antimicrob Agents Chemother 2005;49:2822–7. doi:10.1128/AAC.49.7.2822-2827.2005.

[73] Green B, Cobb ARM, Hopper C. Photodynamic therapy in the management of lesions of the head and neck. Br J Oral Maxillofac Surg 2013;51:283–7. doi:10.1016/j.bjoms.2012.11.011.

[74] Allison R, Moghissi K, Downie G, Dixon K. Photodynamic therapy (PDT) for lung cancer. Photodiagnosis Photodyn Ther 2011;8:231–9. doi:10.1016/j.pdpdt.2011.03.342.

[75] Zeitouni NC, Oseroff AR, Shieh S. Photodynamic therapy for nonmelanoma skin cancers: Current review and update. Mol. Immunol., vol. 39, Elsevier Ltd; 2003, p. 1133–6. doi:10.1016/S0161-5890(03)00083-X.

[76] Moore CM, Pendse D, Emberton M. Photodynamic therapy for prostate cancer - A review of current status and future promise. Nat Clin Pract Urol 2009;6:18–30. doi:10.1038/ncpuro1274.

[77] Athar M, Mukhtar H, Bickers DR. Differential role of reactive oxygen intermediates in photofrin-I- and photofrin-II-mediated photoenhancement of lipid peroxidation in epidermal

microsomal membranes. J Invest Dermatol 1988;90:652–7. doi:10.1111/1523-1747.ep12560814.

[78] Redmond RW, Gamlin JN. A compilation of singlet oxygen yields from biologically relevant molecules. Photochem Photobiol 1999;70:391–475. doi:10.1111/j.1751-1097.1999.tb08240.x.

[79] Lucky SS, Soo KC, Zhang Y. Nanoparticles in Photodynamic Therapy. Chem Rev 2015;115:1990–2042. doi:10.1021/cr5004198.

[80] Castano AP, Demidova TN, Hamblin MR. Mechanisms in photodynamic therapy: Part one - Photosensitizers, photochemistry and cellular localization. Photodiagnosis Photodyn Ther 2004;1:279–93. doi:10.1016/S1572-1000(05)00007-4.

[81] Jijie R. Synthesis and characterization of complex nano-structures at the interface with biological medium. Http://WwwThesesFr 2016.

[82] Vreeburg RAM, Fry SC. Reactive Oxygen Species in Cell Walls. Antioxidants React. Oxyg. Species Plants, vol. 279, 2007, p. 215–49. doi:10.1002/9780470988565.ch9.

[83] Halliwell B. Free radicals and antioxidants - Quo vadis? Trends Pharmacol Sci 2011;32:125–30. doi:10.1016/j.tips.2010.12.002.

[84] Lushchak VI. Free radicals, reactive oxygen species, oxidative stress and its classification. Chem Biol Interact 2014;224:164–75. doi:10.1016/j.cbi.2014.10.016.

[85] Jaque D, Martínez Maestro L, Del Rosal B, Haro-Gonzalez P, Benayas A, Plaza JL, et al. Nanoparticles for photothermal therapies. Nanoscale 2014;6:9494–530. doi:10.1039/c4nr00708e.

[86] Dysart JS, Patterson MS. Characterization of Photofrin photobleaching for singlet oxygen dose estimation during photodynamic therapy of MLL cells in vitro. Phys Med Biol 2005;50:2597–616. doi:10.1088/0031-9155/50/11/011.

[87] Moan J, Berg K, Kvam E, Western A, Malik Z, Rück A, et al. Intracellular localization of photosensitizers. Ciba Found Symp 1989;146:95–111. doi:10.2530/jslsm1980.18.supplement_207.

[88] Habash RWY, Bansal R, Krewski D, Alhafi HDT. Thermal Therapy, Part III: Ablation Techniques. vol. 35. 2007.

[89] Johannsen M, Gneveckow U, Eckelt L, Feussner A, Waldöfner N, Scholz R, et al. Clinical hyperthermia of prostate cancer using magnetic nanoparticles: Presentation of a new interstitial technique. Int J Hyperth 2005;21:637–47. doi:10.1080/02656730500158360.

[90] Longo UG, Ronga M, Maffulli N. Achilles Tendinopathy. Sports Med Arthrosc 2018;26:112–26. doi:10.1097/JSA.0000000000000185.

[91] Grinholc M, Szramka B, Kurlenda J, Graczyk A, Bielawski KP. Bactericidal effect of photodynamic inactivation against methicillin-resistant and methicillin-susceptible Staphylococcus aureus is strain-dependent. J Photochem Photobiol B Biol 2008;90:57–63. doi:10.1016/j.jphotobiol.2007.11.002.

[92] Kashef N, Ravaei Sharif Abadi G, Djavid GE. Phototoxicity of phenothiazinium dyes against methicillin-resistant Staphylococcus aureus and multi-drug resistant Escherichia coli. Photodiagnosis Photodyn Ther 2012;9:11–5. doi:10.1016/j.pdpdt.2011.11.004.

[93] Maaoui H, Jijie R, Pan G-HH, Drider D, Caly D, Bouckaert J, et al. A 980 nm driven photothermal ablation of virulent and antibiotic resistant Gram-positive and Gram-negative bacteria strains using Prussian blue nanoparticles. J Colloid Interface Sci 2016;480:63–8. doi:10.1016/j.jcis.2016.07.002.

[94] Pourhajibagher M, Chiniforush N, Ghorbanzadeh R, Bahador A. Photo-activated disinfection based on indocyanine green against cell viability and biofilm formation of Porphyromonas gingivalis. Photodiagnosis Photodyn Ther 2017;17:61–4. doi:10.1016/j.pdpdt.2016.10.003.

[95] Dahl TA, RobertMiddenand W, Hartman PE. Pure singlet oxygen cytotoxicity for bacteria. Photochem Photobiol 1987;46:345–52. doi:10.1111/j.1751-1097.1987.tb04779.x.

[96] Dahl TA, Midden WR, Hartman PE. Comparison of killing of gram-negative and gram-positive bacteria by pure singlet oxygen. J Bacteriol 1989;171:2188–94. doi:10.1128/jb.171.4.2188-2194.1989.

[97] Wang YW, Fu YY, Wu LJ, Li J, Yang HH, Chen GN. Targeted photothermal ablation of pathogenic bacterium, Staphylococcus aureus, with nanoscale reduced graphene oxide. J Mater Chem B 2013;1:2496–501. doi:10.1039/c3tb20144a.

[98] Turcheniuk K, Hage C-HH, Spadavecchia J, Serrano AY, Larroulet I, Pesquera A, et al. Plasmonic photothermal destruction of uropathogenic E. coli with reduced graphene oxide and core/shell nanocomposites of gold nanorods/reduced graphene oxide. J Mater Chem B 2015;3:375–86. doi:10.1039/C4TB01760A.

[99] Hui L, Auletta JT, Huang Z, Chen X, Xia F, Yang S, et al. Surface Disinfection Enabled by a Layer-by-Layer Thin Film of Polyelectrolyte-Stabilized Reduced Graphene Oxide upon Solar Near-Infrared Irradiation. ACS Appl Mater Interfaces 2015;7:10511–7. doi:10.1021/acsami.5b02008.

[100] Yang G, Li L, Lee WB, Ng MC. Structure of graphene and its disorders: a review. Sci Technol Adv Mater 2018;19:613–48. doi:10.1080/14686996.2018.1494493.

[101] Article Graphenea n.d. https://www.graphenea.com/pages/article-graphenea (accessed January 13, 2020).

[102] Demchenko AP, Dekaliuk MO. Novel fluorescent carbonic nanomaterials for sensing and imaging. Methods Appl Fluoresc 2013;1. doi:10.1088/2050-6120/1/4/042001.

[103] Wallace PR. The band theory of graphite. Phys Rev 1947;71:622–34. doi:10.1103/PhysRev.71.622.

[104] Novoselov KS, Geim AK, Morozov S V., Jiang D, Zhang Y, Dubonos S V., et al. Electric field in atomically thin carbon films. Science 2004;306:666–9. doi:10.1126/science.1102896.

[105] Jo G, Choe M, Lee S, Park W, Kahng YH, Lee T. The application of graphene as electrodes in electrical and optical devices. Nanotechnology 2012;23. doi:10.1088/0957-4484/23/11/112001.

[106] Liang M, Luo B, Zhi L. Application of graphene and graphene-based materials in clean energy-related devices. Int J Energy Res 2009;33:1161–70. doi:10.1002/er.1598.

[107] Palacios T. Graphene electronics: Thinking outside the silicon box. Nat Nanotechnol 2011;6:464–5. doi:10.1038/nnano.2011.125.

[108] Schwierz F. Graphene transistors. Nat Nanotechnol 2010;5:487–96. doi:10.1038/nnano.2010.89.

[109] Pumera M. Graphene in biosensing. Mater Today 2011;14:308–15. doi:10.1016/S1369-7021(11)70160-2.

[110] Pan Y, Sahoo NG, Li L. The application of graphene oxide in drug delivery. Expert Opin Drug Deliv 2012;9:1365–76. doi:10.1517/17425247.2012.729575.

[111] Shin SR, Li YC, Jang HL, Khoshakhlagh P, Akbari M, Nasajpour A, et al. Graphene-based materials for tissue engineering. Adv Drug Deliv Rev 2016;105:255–74. doi:10.1016/j.addr.2016.03.007.

[112] Novoselov KS, Jiang D, Schedin F, Booth TJ, Khotkevich V V., Morozov S V., et al. Two-dimensional atomic crystals. Proc Natl Acad Sci U S A 2005;102:10451–3. doi:10.1073/pnas.0502848102.

[113] Avouris P, Dimitrakopoulos C. Graphene: synthesis and applications. Mater Today 2012;15:86–97. doi:10.1016/S1369-7021(12)70044-5.

[114] Lu G, Yu K, Wen Z, Chen J. Semiconducting graphene: Converting graphene from semimetal to semiconductor. Nanoscale 2013;5:1353–68. doi:10.1039/c2nr32453a.

[115] Schniepp HC, Kudin KN, Li J-L, Prud'homme RK, Car R, Saville DA, et al. Bending Properties of Single Functionalized Graphene Sheets Probed by Atomic Force Microscopy. ACS Nano 2008;2:2577–84. doi:10.1021/nn800457s.

[116] Lee C, Wei X, Kysar JW, Hone J. Measurement of the elastic properties and intrinsic strength of monolayer graphene. Science 2008;321:385–8. doi:10.1126/science.1157996.

[117] Apell SP, Hanson GW, Hägglund C. High optical absorption in graphene 2012.

[118] Balandin AA, Ghosh S, Bao W, Calizo I, Teweldebrhan D, Miao F, et al. Superior Thermal Conductivity of Single-Layer Graphene. Nano Lett 2008;8:902–7. doi:10.1021/nl0731872.

[119] Hummers WS, Offeman RE. Preparation of Graphitic Oxide. J Am Chem Soc 1958;80:1339–1339. doi:10.1021/ja01539a017.

[120] Paredes JI, Villar-Rodil S, Martínez-Alonso A, Tascón JMD. Graphene Oxide Dispersions in Organic Solvents. Langmuir 2008;24:10560–4. doi:10.1021/la801744a.

[121] Gao X, Jang J, Nagase S. Hydrazine and Thermal Reduction of Graphene Oxide: Reaction Mechanisms, Product Structures, and Reaction Design. J Phys Chem C 2010;114:832–42. doi:10.1021/jp909284g.

[122] Stroyuk AL, Andryushina NS, Shcherban' ND, Il'in VG, Efanov VS, Yanchuk IB, et al. Photochemical reduction of graphene oxide in colloidal solution. Theor Exp Chem 2012;48:2–13. doi:10.1007/s11237-012-9235-0.

[123] Park S, An J, Potts JR, Velamakanni A, Murali S, Ruoff RS. Hydrazine-reduction of graphite- and graphene oxide. Carbon 2011;49:3019–23. doi:10.1016/j.carbon.2011.02.071.

[124] Li D, Müller MB, Gilje S, Kaner RB, Wallace GG. Processable aqueous dispersions of graphene nanosheets. Nat Nanotechnol 2008;3:101–5. doi:10.1038/nnano.2007.451.

[125] Szunerits S, Boukherroub R. Graphene-Microbial Interactions. Elsevier Inc.; 2016. doi:10.1016/B978-0-323-41625-2.00008-9.

[126] Zhang J, Yang H, Shen G, Cheng P, Zhang J, Guo S. Reduction of graphene oxide vial-ascorbic acid. Chem Commun 2010;46:1112–4. doi:10.1039/b917705a.

[127] Fernández-Merino MJ, Guardia L, Paredes JI, Villar-Rodil S, Solís-Fernández P, Martínez-Alonso A, et al. Vitamin C Is an Ideal Substitute for Hydrazine in the Reduction of Graphene Oxide Suspensions. J Phys Chem C 2010;114:6426–32. doi:10.1021/jp100603h.

[128] Thakur S, Karak N. Green reduction of graphene oxide by aqueous phytoextracts. Carbon 2012;50:5331–9. doi:10.1016/j.carbon.2012.07.023.

[129] Yang S, Lohe MR, Müllen K, Feng X. New-Generation Graphene from Electrochemical Approaches: Production and Applications. Adv Mater 2016;28:6213–21. doi:10.1002/adma.201505326.

[130] Marković ZM, Budimir MD, Kepić DP, Holclajtner-Antunović ID, Marinović-Cincović MT, Dramićanin MD, et al. Semi-transparent, conductive thin films of electrochemical exfoliated graphene. RSC Adv 2016;6. doi:10.1039/c6ra04250c.

[131] Yang S, Brü S, Wu Z-S, Liu Z, Parvez K, Dong R, et al. Organic Radical-Assisted Electrochemical Exfoliation for the Scalable Production of High-Quality Graphene 2015. doi:10.1021/jacs.5b09000.

[132] Wang X-Y, Narita A, Müllen K. Precision synthesis versus bulk-scale fabrication of graphenes. Nat Rev Chem 2018;2. doi:10.1038/s41570-017-0100.

[133] Berger C, Song Z, Li X, Wu X, Brown N, Naud C, et al. Electronic confinement and coherence in patterned epitaxial graphene. Science 2006;312:1191–6. doi:10.1126/science.1125925.

[134] Mishra N, Boeckl J, Motta N, Iacopi F. Graphene growth on silicon carbide: A review. Phys Status Solidi 2016;213:2277–89. doi:10.1002/pssa.201600091.

[135] Li X, Cai W, An J, Kim S, Nah J, Yang D, et al. Large-area synthesis of high-quality and uniform graphene films on copper foils. Science 2009;324:1312–4. doi:10.1126/science.1171245.

[136] Zagorodko O, Spadavecchia J, Serrano AY, Larroulet I, Pesquera A, Zurutuza A, et al. Highly Sensitive Detection of DNA Hybridization on Commercialized Graphene-Coated Surface Plasmon Resonance Interfaces. Anal Chem 2014;86:11211–6. doi:10.1021/ac502705n.

[137] Tielrooij KJ, Song JCW, Jensen SA, Centeno A, Pesquera A, Zurutuza Elorza A, et al. Photoexcitation cascade and multiple hot-carrier generation in graphene. Nat Phys 2013;9:248–52. doi:10.1038/nphys2564.

[138] Vivekchand SRC, Rout CS, Subrahmanyam KS, Govindaraj A, Rao CNR. Graphene-based electrochemical supercapacitors. J Chem Sci 2008;120:9–13. doi:10.1007/s12039-008-0002-7.

[139] Wang Y, Shi Z, Huang Y, Ma Y, Wang C, Chen M, et al. Supercapacitor Devices Based on Graphene Materials. J Phys Chem C 2009;113:13103–7. doi:10.1021/jp902214f.

[140] Aerospace | Graphene-Info n.d. https://www.graphene-info.com/tags/aerospace (accessed January 28, 2020).

[141] Huang H, Song Z, Wei N, Shi L, Mao Y, Ying Y, et al. Ultrafast viscous water flow through

nanostrand-channelled graphene oxide membranes. Nat Commun 2013;4. doi:10.1038/ncomms3979.

[142] Pinto AM, Gonçalves IC, Magalhães FD. Graphene-based materials biocompatibility: A review. Colloids Surf B Biointerfaces 2013;111:188–202. doi:10.1016/j.colsurfb.2013.05.022.

[143] Kiew SF, Kiew LV, Lee HB, Imae T, Chung LY. Assessing biocompatibility of graphene oxide-based nanocarriers: A review. J Control Release 2016;226:217–28. doi:10.1016/j.jconrel.2016.02.015.

[144] Syama S, Mohanan P V. Safety and biocompatibility of graphene: A new generation nanomaterial for biomedical application. Int J Biol Macromol 2016;86:546–55. doi:10.1016/j.ijbiomac.2016.01.116.

[145] Ruiz ON, Fernando KAS, Wang B, Brown NA, Luo PG, McNamara ND, et al. Graphene Oxide: A Nonspecific Enhancer of Cellular Growth. ACS Nano 2011;5:8100–7. doi:10.1021/nn202699t.

[146] Sreeprasad TS, Maliyekkal MS, Deepti K, Chaudhari K, Xavier PL, Pradeep T. Transparent, Luminescent, Antibacterial and Patternable Film Forming Composites of Graphene Oxide/Reduced Graphene Oxide. ACS Appl Mater Interfaces 2011;3:2643–54. doi:10.1021/am200447p.

[147] Perreault F, de Faria AF, Nejati S, Elimelech M. Antimicrobial Properties of Graphene Oxide Nanosheets: Why Size Matters. ACS Nano 2015;9:7226–36. doi:10.1021/acsnano.5b02067.

[148] Liu S, Hu M, Zeng TH, Wu R, Jiang R, Wei J, et al. Lateral Dimension-Dependent Antibacterial Activity of Graphene Oxide Sheets. Langmuir 2012;28:12364–72. doi:10.1021/la3023908.

[149] Akhavan O, Ghaderi E. Toxicity of Graphene and Graphene Oxide Nanowalls Against Bacteria. ACS Nano 2010;4:5731–6. doi:10.1021/nn101390x.

[150] Hu W, Peng C, Luo W, Lv M, Li X, Li D, et al. Graphene-Based Antibacterial Paper. ACS Nano 2010;4:4317–23. doi:10.1021/nn101097v.

[151] Krishnamoorthy K, Veerapandian M, Zhang L-H, Yun K, Kim SJ. Antibacterial Efficiency of Graphene Nanosheets against Pathogenic Bacteria via Lipid Peroxidation. J Phys Chem C 2012;116:17280–7. doi:10.1021/jp3047054.

[152] Tu Y, Lv M, Xiu P, Huynh T, Zhang M, Castelli M, et al. Destructive extraction of phospholipids from Escherichia coli membranes by graphene nanosheets. Nat Nanotechnol 2013;8:594–601. doi:10.1038/nnano.2013.125.

[153] Fernández-Ibáñez P, Polo-López MI, Malato S, Wadhwa S, Hamilton JWJ, Dunlop PSM, et al. Solar photocatalytic disinfection of water using titanium dioxide graphene composites. Chem Eng J 2015;261:36–44. doi:10.1016/J.CEJ.2014.06.089.

[154] Miao H, Teng Z, Wang S, Xu L, Wang C, Chong H. Recent Advances in the Disinfection of Water Using Nanoscale Antimicrobial Materials. Adv Mater Technol 2018:1800213. doi:10.1002/admt.201800213.

[155] Xiang Q, Yu J, Jaroniec M. Graphene-based semiconductor photocatalysts. Chem Soc Rev 2012;41:782–96. doi:10.1039/C1CS15172J.

[156] Shahnawaz Khan M, Abdelhamid HN, Wu HF. Near infrared (NIR) laser mediated surface activation of graphene oxide nanoflakes for efficient antibacterial, antifungal and wound healing treatment. Colloids Surf B Biointerfaces 2015;127:281–91. doi:10.1016/j.colsurfb.2014.12.049.

[157] Wu M-C, Deokar AR, Liao J-H, Shih P-Y, Ling Y-C. Graphene-Based Photothermal Agent for Rapid and Effective Killing of Bacteria. ACS Nano 2013;7:1281–90. doi:10.1021/nn304782d.

[158] Barbolina I, Woods CR, Lozano N, Kostarelos K, Novoselov KS, Roberts IS. Purity of graphene oxide determines its antibacterial activity. 2D Mater 2016;3:025025. doi:10.1088/2053-1583/3/2/025025.

[159] Marković ZM, Jovanović SP, Mašković PZ, Danko M, Mičušík M, Pavlović VB, et al. Photo-induced antibacterial activity of four graphene based nanomaterials on a wide range of bacteria. RSC Adv 2018;8:31337–47. doi:10.1039/c8ra04664f.

[160] Jovanović S, Holclajtner-Antunović I, Uskoković-Marković S, Bajuk-Bogdanović D, Pavlović V, Tošić D, et al. Modification of graphene oxide surfaces with 12-molybdophosphoric acid: Structural and antibacterial study. Mater Chem Phys 2018;213:157–67. doi:10.1016/j.matchemphys.2018.04.011.

[161] Hegab HM, Elmekawy A, Zou L, Mulcahy D, Saint CP, Ginic-Markovic M. The controversial antibacterial activity of graphene-based materials. Carbon 2016;105:362–76. doi:10.1016/j.carbon.2016.04.046.

[162] Marković ZM, Matijašević DM, Pavlović VB, Jovanović SP, Holclajtner-Antunović ID, Špitalský Z, et al. Antibacterial potential of electrochemically exfoliated graphene sheets. J Colloid Interface Sci 2017;500:30–43. doi:10.1016/j.jcis.2017.03.110.

[163] Cheng Y-W, Wang S-H, Liu C-M, Chien M-Y, Hsu C-C, Liu T-Y. Amino-modified graphene oxide nanoplatelets for photo-thermal and anti-bacterial capability. Surf Coatings Technol 2020;385:125441. doi:10.1016/j.surfcoat.2020.125441.

[164] Geng H, Wang T, Cao H, Zhu H, Di Z, Liu X. Antibacterial ability, cytocompatibility and hemocompatibility of fluorinated graphene. Colloids Surf B Biointerfaces 2019;173:681–8. doi:10.1016/j.colsurfb.2018.10.050.

[165] Lim SY, Shen W, Gao Z. Carbon quantum dots and their applications. Chem Soc Rev 2015;44:362–81. doi:10.1039/c4cs00269e.

[166] Li H, Kang Z, Liu Y, Lee S-T. Carbon nanodots: synthesis, properties and applications. J Mater Chem 2012;22:24230. doi:10.1039/c2jm34690g.

[167] Baker SN, Baker GA. Luminescent Carbon Nanodots: Emergent Nanolights. Angew Chem Int Ed 2010;49:6726–44. doi:10.1002/anie.200906623.

[168] Zhang H, Huang H, Ming H, Li H, Zhang L, Liu Y, et al. Carbon quantum dots/Ag 3 PO 4 complex photocatalysts with enhanced photocatalytic activity and stability under visible light. J Mater Chem 2012;22:10501–6. doi:10.1039/c2jm30703k.

[169] Ming H, Ma Z, Liu Y, Pan K, Yu H, Wang F, et al. Large scale electrochemical synthesis of high quality carbon nanodots and their photocatalytic property. Dalton Trans 2012;41:9526–31. doi:10.1039/c2dt30985h.

[170] Li H, He X, Kang Z, Huang H, Liu Y, Liu J, et al. Water-Soluble Fluorescent Carbon

Quantum Dots and Photocatalyst Design. Angew Chem Int Ed 2010;49:4430–4. doi:10.1002/anie.200906154.

[171] Xu X, Ray R, Gu Y, Ploehn HJ, Gearheart L, Raker K, et al. Electrophoretic analysis and purification of fluorescent single-walled carbon nanotube fragments. J Am Chem Soc 2004;126:12736–7. doi:10.1021/ja040082h.

[172] Sun YP, Zhou B, Lin Y, Wang W, Fernando KAS, Pathak P, et al. Quantum-sized carbon dots for bright and colorful photoluminescence. J Am Chem Soc 2006;128:7756–7. doi:10.1021/ja062677d.

[173] Yu SJ, Kang MW, Chang HC, Chen KM, Yu YC. Bright fluorescent nanodiamonds: No photobleaching and low cytotoxicity. J Am Chem Soc 2005;127:17604–5. doi:10.1021/ja0567081.

[174] Zhou J, Booker C, Li R, Zhou X, Sham TK, Sun X, et al. An electrochemical avenue to blue luminescent nanocrystals from multiwalled carbon nanotubes (MWCNTs). J Am Chem Soc 2007;129:744–5. doi:10.1021/ja0669070.

[175] Liu H, Ye T, Mao C. Fluorescent carbon nanoparticles derived from candle soot. Angew Chem Int Ed 2007;46:6473–5. doi:10.1002/anie.200701271.

[176] Dong Y, Zhou N, Lin X, Lin J, Chi Y, Chen G. Extraction of electrochemiluminescent oxidized carbon quantum dots from activated carbon. Chem Mater 2010;22:5895–9. doi:10.1021/cm1018844.

[177] Wang Q, Zheng H, Long Y, Zhang L, Gao M, Bai W. Microwave-hydrothermal synthesis of fluorescent carbon dots from graphite oxide. Carbon 2011;49:3134–40. doi:10.1016/j.carbon.2011.03.041.

[178] Bourlinos AB, Stassinopoulos A, Anglos D, Zboril R, Karakassides M, Giannelis EP. Surface functionalized carbogenic quantum dots. Small 2008;4:455–8. doi:10.1002/smll.200700578.

[179] Li H, He X, Liu Y, Huang H, Lian S, Lee ST, et al. One-step ultrasonic synthesis of water-soluble carbon nanoparticles with excellent photoluminescent properties. Carbon 2011;49:605–9. doi:10.1016/j.carbon.2010.10.004.

[180] Liu R, Wu D, Liu S, Koynov K, Knoll W, Li Q. An aqueous route to multicolor photoluminescent carbon dots using silica spheres as carriers. Angew Chem Int Ed 2009;48:4598–601. doi:10.1002/anie.200900652.

[181] Zhu S, Meng Q, Wang L, Zhang J, Song Y, Jin H, et al. Highly photoluminescent carbon dots for multicolor patterning, sensors, and bioimaging. Angew Chem Int Ed 2013;52:3953–7. doi:10.1002/anie.201300519.

[182] Yang Y, Cui J, Zheng M, Hu C, Tan S, Xiao Y, et al. One-step synthesis of amino-functionalized fluorescent carbon nanoparticles by hydrothermal carbonization of chitosan 2012;48:380–2.

[183] Shen L, Zhang L, Chen M, Chen X, Wang J. The production of pH-sensitive photoluminescent carbon nanoparticles by the carbonization of polyethylenimine and their use for bioimaging. Carbon 2013;55:343–9. doi:10.1016/j.carbon.2012.12.074.

[184] Yang ZC, Wang M, Yong AM, Wong SY, Zhang XH, Tan H, et al. Intrinsically fluorescent carbon dots with tunable emission derived from hydrothermal treatment of glucose in the

presence of monopotassium phosphate. Chem Commun 2011;47:11615–7. doi:10.1039/c1cc14860e.

[185] Sahu S, Behera B, Maiti TK, Mohapatra S. Simple one-step synthesis of highly luminescent carbon dots from orange juice: Application as excellent bio-imaging agents. Chem Commun 2012;48:8835–7. doi:10.1039/c2cc33796g.

[186] Zhao S, Lan M, Zhu X, Xue H, Ng TW, Meng X, et al. Green Synthesis of Bifunctional Fluorescent Carbon Dots from Garlic for Cellular Imaging and Free Radical Scavenging. ACS Appl Mater Interfaces 2015;7:17054–60. doi:10.1021/acsami.5b03228.

[187] D'Souza SL, Deshmukh B, Bhamore JR, Rawat KA, Lenka N, Kailasa SK. Synthesis of fluorescent nitrogen-doped carbon dots from dried shrimps for cell imaging and boldine drug delivery system. RSC Adv 2016;6:12169–79. doi:10.1039/c5ra24621k.

[188] Yang X, Zhuo Y, Zhu S, Luo Y, Feng Y, Dou Y. Novel and green synthesis of high-fluorescent carbon dots originated from honey for sensing and imaging. Biosens Bioelectron 2014;60:292–8. doi:10.1016/j.bios.2014.04.046.

[189] Zhai X, Zhang P, Liu C, Bai T, Li W, Dai L, et al. Highly luminescent carbon nanodots by microwave-assisted pyrolysis. Chem Commun 2012;48:7955–7. doi:10.1039/c2cc33869f.

[190] Zhu H, Wang X, Li Y, Wang Z, Yang F, Yang X. Microwave synthesis of fluorescent carbon nanoparticles with electrochemiluminescence properties. Chem Commun 2009:5118–20. doi:10.1039/b907612c.

[191] Namdari P, Negahdari B, Eatemadi A. Synthesis, properties and biomedical applications of carbon-based quantum dots: An updated review. Biomed Pharmacother 2017;87:209–22. doi:10.1016/J.BIOPHA.2016.12.108.

[192] Nie H, Li M, Li Q, Liang S, Tan Y, Sheng L, et al. Carbon dots with continuously tunable full-color emission and their application in ratiometric pH sensing. Chem Mater 2014;26:3104–12. doi:10.1021/cm5003669.

[193] Ren X, Liang W, Wang P, Bunker CE, Coleman M, Teisl LR, et al. A new approach in functionalization of carbon nanoparticles for optoelectronically relevant carbon dots and beyond. Carbon 2019;141:553–60. doi:10.1016/j.carbon.2018.09.085.

[194] Liu J-H, Anilkumar P, Cao L, Wang X, Yang S-T, Luo PG, et al. Cytotoxicity evaluations of fluorescent carbon nanoparticles. Nano Life 2010;01:153–61. doi:10.1142/s1793984410000158.

[195] Iida T, Mori T, Katayama Y, Niidome T. Overall interaction of cytosolic proteins with the PEI/DNA complex. J Control Release 2007;118:364–9. doi:10.1016/j.jconrel.2006.12.027.

[196] Pierrat P, Wang R, Kereselidze D, Lux M, Didier P, Kichler A, et al. Efficient invitro and invivo pulmonary delivery of nucleic acid by carbon dot-based nanocarriers. Biomaterials 2015;51:290–302. doi:10.1016/j.biomaterials.2015.02.017.

[197] Bjugstad KB, Lampe K, Kern DS, Mahoney M. Biocompatibility of poly(ethylene glycol)-based hydrogels in the brain: An analysis of the glial response across space and time. J Biomed Mater Res Part A 2010;95A:79–91. doi:10.1002/jbm.a.32809.

[198] Devi P, Saini S, Kim K-HH. The advanced role of carbon quantum dots in nanomedical applications. vol. 141. 2019. doi:10.1016/j.bios.2019.02.059.

[199] Bae YH, Park K. Targeted drug delivery to tumors: Myths, reality and possibility. J Control Release 2011;153:198–205. doi:10.1016/j.jconrel.2011.06.001.

[200] Knop K, Hoogenboom R, Fischer D, Schubert US. Poly(ethylene glycol) in Drug Delivery: Pros and Cons as Well as Potential Alternatives. Angew Chem Int Ed 2010;49:6288–308. doi:10.1002/anie.200902672.

[201] Nicollian EH. Surface Passivation of Semiconductors. J Vac Sci Technol 1971;8:S39–49. doi:10.1116/1.1316388.

[202] Guo Y, Wang Z, Shao H, Jiang X. Hydrothermal synthesis of highly fluorescent carbon nanoparticles from sodium citrate and their use for the detection of mercury ions. Carbon 2013;52:583–9. doi:10.1016/j.carbon.2012.10.028.

[203] Huang H, Lv JJ, Zhou DL, Bao N, Xu Y, Wang AJ, et al. One-pot green synthesis of nitrogen-doped carbon nanoparticles as fluorescent probes for mercury ions. RSC Adv 2013;3:21691–6. doi:10.1039/c3ra43452d.

[204] Yan F, Zou Y, Wang M, Mu X, Yang N, Chen L. Highly photoluminescent carbon dots-based fluorescent chemosensors for sensitive and selective detection of mercury ions and application of imaging in living cells. Sens Actuators, B Chem 2014;192:488–95. doi:10.1016/j.snb.2013.11.041.

[205] Posthuma-Trumpie GA, Wichers JH, Koets M, Berendsen LBJM, Van Amerongen A. Amorphous carbon nanoparticles: A versatile label for rapid diagnostic (immuno)assays. Anal Bioanal Chem 2012;402:593–600. doi:10.1007/s00216-011-5340-5.

[206] Li H, Zhang Y, Wang L, Tian J, Sun X. Nucleic acid detection using carbon nanoparticles as a fluorescent sensing platform. Chem Commun 2011;47:961–3. doi:10.1039/c0cc04326e.

[207] Qu K, Wang J, Ren J, Qu X. Carbon dots prepared by hydrothermal treatment of dopamine as an effective fluorescent sensing platform for the label-free detection of iron(III) ions and dopamine. Chem - A Eur J 2013;19:7243–9. doi:10.1002/chem.201300042.

[208] Zheng M, Xie Z, Qu D, Li D, Du P, Jing X, et al. On-off-on fluorescent carbon dot nanosensor for recognition of chromium(VI) and ascorbic acid based on the inner filter effect. ACS Appl Mater Interfaces 2013;5:13242–7. doi:10.1021/am4042355.

[209] Liu G, Li X, Yu Z, Ren P, Yang F, Wang J, et al. Nonenzymatic detection of glucose based on Cu 2+ catalytic oxidation on N-doped carbon quantum dots. J Phys Chem Solids 2018;123:344–54. doi:10.1016/j.jpcs.2018.08.025.

[210] Wang Y, Anilkumar P, Cao L, Liu J-H, Luo PG, Tackett KN, et al. Carbon dots of different composition and surface functionalization: cytotoxicity issues relevant to fluorescence cell imaging. Exp Biol Med 2011;236:1231–8. doi:10.1258/ebm.2011.011132.

[211] Bourlinos AB, Stassinopoulos A, Anglos D, Zboril R, Georgakilas V, Giannelis EP. Photoluminescent carbogenic dots. Chem Mater 2008;20:4539–41. doi:10.1021/cm800506r.

[212] Hsu PC, Chen PC, Ou CM, Chang HYHT, Chang HYHT. Extremely high inhibition activity of photoluminescent carbon nanodots toward cancer cells. J Mater Chem B 2013;1:1774–81. doi:10.1039/c3tb00545c.

[213] Fowley C, McCaughan B, Devlin A, Yildiz I, Raymo FM, Callan JF. Highly luminescent biocompatible carbon quantum dots by encapsulation with an amphiphilic polymer. Chem Commun 2012;48:9361–3. doi:10.1039/c2cc34962k.

[214] Liu C, Zhang P, Zhai X, Tian F, Li W, Yang J, et al. Nano-carrier for gene delivery and bioimaging based on carbon dots with PEI-passivation enhanced fluorescence 2012;33:3604–13. doi:10.1016/j.biomaterials.2012.01.052.

[215] Yang S-T, Cao L, Luo PG, Lu F, Wang X, Wang H, et al. Carbon Dots for Optical Imaging in Vivo. J Am Chem Soc 2009;131:11308–9. doi:10.1021/ja904843x.

[216] Cao L, Yang ST, Wang X, Luo PG, Liu JH, Sahu S, et al. Competitive performance of carbon "quantum" dots in optical bioimaging. Theranostics 2012;2:295–301. doi:10.7150/thno.3912.

[217] Hola K, Bourlinos AB, Kozak O, Berka K, Siskova KM, Havrdova M, et al. Photoluminescence effects of graphitic core size and surface functional groups in carbon dots: COO- induced red-shift emission. Carbon 2014;70:279–86. doi:10.1016/j.carbon.2014.01.008.

[218] Tao H, Yang K, Ma Z, Wan J, Zhang Y, Kang Z, et al. In Vivo NIR Fluorescence Imaging, Biodistribution, and Toxicology of Photoluminescent Carbon Dots Produced from Carbon Nanotubes and Graphite. Small 2012;8:281–90. doi:10.1002/smll.201101706.

[219] Li CF, Yan ZK, Chen LB, Jin JP, Li DD. Desmin detection by facile prepared carbon quantum dots for early screening of colorectal cancer. Medicine (United States) 2017;96. doi:10.1097/MD.0000000000005521.

[220] Zheng M, Ruan S, Liu S, Sun T, Qu D, Zhao H, et al. Self-Targeting Fluorescent Carbon Dots for Diagnosis of Brain Cancer Cells. ACS Nano 2015;9:11455–61. doi:10.1021/acsnano.5b05575.

[221] Anjana RR, Anjali Devi JS, Jayasree M, Aparna RS, Aswathy B, Praveen GL, et al. S,N-doped carbon dots as a fluorescent probe for bilirubin. Microchim Acta 2018;185. doi:10.1007/s00604-017-2574-8.

[222] Kurdekar A, Chunduri LAA, Bulagonda EP, Haleyurgirisetty MK, Kamisetti V, Hewlett IK. Comparative performance evaluation of carbon dot-based paper immunoassay on Whatman filter paper and nitrocellulose paper in the detection of HIV infection. Microfluid Nanofluidics 2016;20. doi:10.1007/s10404-016-1763-9.

[223] Dolmans DEJGJ, Fukumura D, Jain RK. Photodynamic therapy for cancer. Nat Rev Cancer 2003;3:380–7. doi:10.1038/nrc1071.

[224] Juzenas P, Kleinauskas A, George Luo P, Sun YP. Photoactivatable carbon nanodots for cancer therapy. Appl Phys Lett 2013;103. doi:10.1063/1.4817787.

[225] Wang Q, Huang X, Long Y, Wang X, Zhang H, Zhu R, et al. Hollow luminescent carbon dots for drug delivery. Carbon 2013;59:192–9. doi:10.1016/j.carbon.2013.03.009.

[226] Yang Y, Yan Z, Wei D, Zhong J, Liu L, Zhang L, et al. Tumor-penetrating peptide functionalization enhances the anti-glioblastoma effect of doxorubicin liposomes. Nanotechnology 2013;24. doi:10.1088/0957-4484/24/40/405101.

[227] Bing W, Sun H, Yan Z, Ren J, Qu X. Programmed Bacteria Death Induced by Carbon Dots with Different Surface Charge. Small 2016;12:4713–8. doi:10.1002/smll.201600294.

[228] Travlou NA, Giannakoudakis DA, Algarra M, Labella AM, Rodríguez-Castellón E, Bandosz TJ. S- and N-doped carbon quantum dots: Surface chemistry dependent antibacterial activity. Carbon 2018;135:104–11. doi:10.1016/j.carbon.2018.04.018.

[229] Meziani MJ, Dong X, Zhu L, Jones LP, LeCroy GE, Yang F, et al. Visible-Light-Activated Bactericidal Functions of Carbon "Quantum" Dots. ACS Appl Mater Interfaces 2016;8:10761–6. doi:10.1021/acsami.6b01765.

[230] Li Y-J, Harroun SG, Su Y-C, Huang C-F, Unnikrishnan B, Lin H-J, et al. Synthesis of Self-Assembled Spermidine-Carbon Quantum Dots Effective against Multidrug-Resistant Bacteria. Adv Healthcare Mater 2016;5:2545–54. doi:10.1002/adhm.201600297.

[231] Zhao DL, Chung TS. Applications of carbon quantum dots (CQDs) in membrane technologies: A review. Water Res 2018;147:43–9. doi:10.1016/j.watres.2018.09.040.

[232] Ristic BZ, Milenkovic MM, Dakic IR, Todorovic-Markovic BM, Milosavljevic MS, Budimir MD, et al. Photodynamic antibacterial effect of graphene quantum dots. Biomaterials 2014;35:4428–35. doi:10.1016/j.biomaterials.2014.02.014.

[233] Nie X, Wu S, Mensah A, Lu K, Wei Q. Carbon quantum dots embedded electrospun nanofibers for efficient antibacterial photodynamic inactivation. Mater Sci Eng C 2020;108:110377. doi:10.1016/j.msec.2019.110377.

[234] Zhang J, An X, Li X, Liao X, Nie Y, Fan Z. Enhanced antibacterial properties of the bracket under natural light via decoration with ZnO/carbon quantum dots composite coating. Chem Phys Lett 2018;706:702–7. doi:10.1016/j.cplett.2018.06.029.

[235] Marković ZM, Kováčová M, Humpolíček P, Budimir MD, Vajďák J, Kubát P, et al. Antibacterial photodynamic activity of carbon quantum dots/polydimethylsiloxane nanocomposites against Staphylococcus aureus, Escherichia coli and Klebsiella pneumoniae. Photodiagnosis Photodyn Ther 2019;26:342–9. doi:10.1016/j.pdpdt.2019.04.019.

[236] Yadav P, Nishanthi ST, Purohit B, Shanavas A, Kailasam K. Metal free visible light photocatalytic carbon nitride quantum dots as efficient antibacterial agents: An insight study. Carbon 2019;152:587–97. doi:10.1016/j.carbon.2019.06.045.

[237] Polymer | Description, Examples, & Types | Britannica n.d. https://www.britannica.com/science/polymer (accessed January 23, 2020).

[238] Seymour RB, Kauffman GB. Products of chemistry - Polyurethanes: A class of modern versatile materials. J Chem Educ 1992;69:909–10. doi:10.1021/ed069p909.

[239] Yasuda HK. Plasma Polymerization - H K Yasuda - Google Books. Academic Press Inc.; 1985.

[240] Polyurethane synthesis - Wikimedia Commons n.d. https://commons.wikimedia.org/wiki/File:Polyurethane_synthesis.svg (accessed February 5, 2020).

[241] Polyethylenimine - Wikipedia n.d. https://en.wikipedia.org/wiki/Polyethylenimine (accessed January 23, 2020).

[242] Yemul O, Imae T. Synthesis and characterization of poly(ethyleneimine) dendrimers. Colloid Polym Sci 2008;286:747–52. doi:10.1007/s00396-007-1830-6.

[243] Godbey WT, Wu KK, Mikos AG. Poly(ethylenimine) and its role in gene delivery. J Control Release 1999;60:149–60. doi:10.1016/S0168-3659(99)00090-5.

[244] Wågberg L. Polyelectrolyte adsorption onto cellulose fibres. Pap. Chem. Technol., 2009, p. 147–72. doi:10.1515/9783110213447.

[245] Vicennati P, Giuliano A, Ortaggi G, Masotti A. Polyethylenimine In Medicinal Chemistry. Curr Med Chem 2008;15:2826–39. doi:10.2174/092986708786242778.

[246] Moghimi SM, Symonds P, Murray JC, Hunter AC, Debska G, Szewczyk A. A two-stage poly(ethylenimine)-mediated cytotoxicity: Implications for gene transfer/therapy. Mol Ther 2005;11:990–5. doi:10.1016/j.ymthe.2005.02.010.

[247] Vancha AR, Govindaraju S, Parsa KVL, Jasti M, González-García M, Ballestero RP. Use of polyethyleneimine polymer in cell culture as attachment factor and lipofection enhancer. BMC Biotechnol 2004;4. doi:10.1186/1472-6750-4-23.

[248] Helander IM, Alakomi HL, Latva-Kala K, Koski P. Polyethyleneimine is an effective permeabilizer of Gram-negative bacteria. Microbiology 1997;143:3193–9. doi:10.1099/00221287-143-10-3193.

[249] gamma ray | Definition & Applications | Britannica n.d. https://www.britannica.com/science/gamma-ray (accessed January 26, 2020).

[250] Steris. Contract Sterilization & Decontamination Services | STERIS AST 2017. https://www.steris-ast.com/ (accessed February 25, 2020).

[251] Ruryk. EM Spectrum Properties - Wikimedia Commons n.d. https://commons.wikimedia.org/wiki/File:EM_Spectrum_Properties_edit.svg (accessed February 5, 2020).

[252] Gamma ray - Wikipedia n.d. https://en.wikipedia.org/wiki/Gamma_ray (accessed January 26, 2020).

[253] Vagabond J. How do Photons Interact with Matter? Simple scatter, Compton scatter, Pair Production | John Vagabond's Physics and Chemistry Blog 2014. https://johnvagabondscience.wordpress.com/2014/04/14/how-photons-interact-with-matter/ (accessed February 5, 2020).

[254] Montanari L, Costantini M, Signoretti EC, Valvo L, Santucci M, Bartolomei M, et al. Gamma irradiation effects on poly(DL-lactictide-co-glycolide) microspheres. J Control Release 1998;56:219–29. doi:10.1016/S0168-3659(98)00082-0.

[255] Zhao C, Hirota K, Taguchi M, Takigami M, Kojima T. Radiolytic degradation of octachlorodibenzo-p-dioxin and octachlorodibenzofuran in organic solvents and treatment of dioxin-containing liquid wastes. Radiat Phys Chem 2007;76:37–45. doi:10.1016/j.radphyschem.2006.01.014.

[256] Seino S, Kinoshita T, Otome Y, Okitsu K, Nakagawa T, Yamamoto TA. Magnetic Composite Nanoparticle of Au/γ-Fe 2 O 3 Synthesized by Gamma-Ray Irradiation. Chem Lett 2003;32:690–1. doi:10.1246/cl.2003.690.

[257] Pospíšil M, Čuba V, Múčka V, Drtinová B. Radiation removal of lead from aqueous solutions - Effects of various sorbents and nitrous oxide. Radiat Phys Chem 2006;75:403–7. doi:10.1016/j.radphyschem.2005.09.008.

[258] Wu WT, Shi L, Wang Y, Pang W, Zhu Q. One-step functionalization of multi-walled carbon nanotubes with Ag/polymer under γ-ray irradiation. Nanotechnology 2008;19. doi:10.1088/0957-4484/19/12/125607.

[259] Barker SA, Lloyd IRL, Stacey M. Polymerization of Glucose Induced by Gamma Radiation. Radiat Res 1962;16:224. doi:10.2307/3571154.

[260] Haji-Saeid M, Safrany A, Sampa MH de O, Ramamoorthy N. Radiation processing of natural polymers: The IAEA contribution. Radiat Phys Chem 2010;79:255–60. doi:10.1016/j.radphyschem.2009.11.001.

[261] Zhang Y, Chen L, Xu Z, Li Y, Zhou B, Shan M, et al. Preparing graphene with notched edges and nanopore defects by γ-ray etching of graphite oxide. Mater Lett 2012;89:226–8. doi:10.1016/j.matlet.2012.08.113.

[262] Ansón-Casaos A, Puértolas JA, Pascual FJ, Hernández-Ferrer J, Castell P, Benito AM, et al. The effect of gamma-irradiation on few-layered graphene materials. Appl. Surf. Sci., vol. 301, Elsevier B.V.; 2014, p. 264–72. doi:10.1016/j.apsusc.2014.02.057.

[263] Xu Z, Chen L, Zhou B, Li Y, Li B, Niu J, et al. Nano-structure and property transformations of carbon systems under γ-ray irradiation: A review. RSC Adv 2013;3:10579–97. doi:10.1039/c3ra00154g.

[264] Erçin D, Eken M, Aktas Z, Çetinkaya S, Sakintuna B, Yürüm Y. Effect of γ-irradiation on the structure of activated carbons produced from Turkish Elbistan lignite. Radiat Phys Chem 2005;73:263–71. doi:10.1016/j.radphyschem.2004.09.025.

[265] Sekulić DR, Babić BM, Kljajević LM, Stašić JM, Kaludjerović B V. The effect of gamma radiation on the properties of activated carbon cloth. J Serbian Chem Soc 2009;74:1125–32. doi:10.2298/JSC0910125S.

[266] Zhang B, Li L, Wang Z, Xie S, Zhang Y, Shen Y, et al. Radiation induced reduction: An effective and clean route to synthesize functionalized graphene. J Mater Chem 2012;22:7775–81. doi:10.1039/c2jm16722k.

[267] Kleut D, Jovanović S, Marković Z, Kepić D, Tošić D, Romčević N, et al. Comparison of structural properties of pristine and gamma irradiated single-wall carbon nanotubes: Effects of medium and irradiation dose. Mater Charact 2012;72:37–45. doi:10.1016/j.matchar.2012.07.002.

[268] Safibonab B, Reyhani A, Nozad Golikand A, Mortazavi SZ, Mirershadi S, Ghoranneviss M. Improving the surface properties of multi-walled carbon nanotubes after irradiation with gamma rays. Appl Surf Sci 2011;258:766–73. doi:10.1016/j.apsusc.2011.08.085.

[269] Tošić D, Marković Z, Dramićanin M, Holclajtner Antunović I, Jovanović S, Milosavljević M, et al. Gamma ray assisted fabrication of fluorescent oligographene nanoribbons. Mater Res Bull 2012;47:1996–2000. doi:10.1016/j.materresbull.2012.04.012.

[270] Jovanović S, Marković Z, Budimir M, Spitalsky Z, Vidoeski B, Todorović Marković B. Effects of low gamma irradiation dose on the photoluminescence properties of graphene quantum dots. Opt Quantum Electron 2016;48. doi:10.1007/s11082-016-0516-z.

[271] Li C, Ye R, Bouckaert J, Zurutuza A, Drider D, Dumych T, et al. Flexible Nanoholey Patches for Antibiotic-Free Treatments of Skin Infections. ACS Appl Mater Interfaces 2017;9:36665–74. doi:10.1021/acsami.7b12949.

[272] Budimir M, Jijie R, Ye R, Barras A, Melinte S, Silhanek A, et al. Efficient capture and photothermal ablation of planktonic bacteria and biofilms using reduced graphene oxide-polyethyleneimine flexible nanoheaters. J Mater Chem B 2019;7:2771–81. doi:10.1039/c8tb01676c.

[273] Al Nafiey A, Addad A, Sieber B, Chastanet G, Barras A, Szunerits S, et al. Reduced graphene oxide decorated with Co 3 O 4 nanoparticles (rGO-Co 3 O 4) nanocomposite: A

reusable catalyst for highly efficient reduction of 4-nitrophenol, and Cr(VI) and dye removal from aqueous solutions. Chem Eng J 2017;322:375–84. doi:10.1016/j.cej.2017.04.039.

[274] Cai X, Lin M, Tan S, Mai W, Zhang Y, Liang Z, et al. The use of polyethyleneimine-modified reduced graphene oxide as a substrate for silver nanoparticles to produce a material with lower cytotoxicity and long-term antibacterial activity. Carbon 2012;50:3407–15. doi:10.1016/j.carbon.2012.02.002.

[275] Dresselhaus MS, Jorio A, Souza Filho AG, Saito R. Defect characterization in graphene and carbon nanotubes using Raman spectroscopy. Philos Trans R Soc A Math Phys Eng Sci 2010;368:5355–77. doi:10.1098/rsta.2010.0213.

[276] Gómez-Navarro C, Weitz RT, Bittner AM, Scolari M, Mews A, Burghard M, et al. Electronic transport properties of individual chemically reduced graphene oxide sheets. Nano Lett 2007;7:3499–503. doi:10.1021/nl072090c.

[277] Wang Q, Vasilescu A, Wang Q, Coffinier Y, Li M, Boukherroub R, et al. Electrophoretic Approach for the Simultaneous Deposition and Functionalization of Reduced Graphene Oxide Nanosheets with Diazonium Compounds: Application for Lysozyme Sensing in Serum. ACS Appl Mater Interfaces 2017;9:12823–31. doi:10.1021/acsami.6b15955.

[278] Couture M, Liang Y, Poirier Richard HP, Faid R, Peng W, Masson JF. Tuning the 3D plasmon field of nanohole arrays. Nanoscale 2013;5:12399–408. doi:10.1039/c3nr04002j.

[279] Nishida M, Hatakenaka N, Kadoya Y. Multipole surface plasmons in metallic nanohole arrays. Phys Rev B - Condens Matter Mater Phys 2015;91. doi:10.1103/PhysRevB.91.235406.

[280] Schwind M, Kasemo B, Zorić I. Localized and propagating plasmons in metal films with nanoholes. Nano Lett 2013;13:1743–50. doi:10.1021/nl400328x.

[281] Chaney EN, Baldwin RP. Voltammetric determination of doxorubicin in urine by adsorptive preconcentration and flow injection analysis. Anal Chim Acta 1985;176:105–12. doi:10.1016/S0003-2670(00)81637-2.

[282] Lesuffleur A, Im H, Lindquist NC, Oh SH. Periodic nanohole arrays with shape-enhanced plasmon resonance as real-time biosensors. Appl Phys Lett 2007;90. doi:10.1063/1.2747668.

[283] Stanković NK, Bodik M, Šiffalovič P, Kotlar M, Mičušik M, Špitalsky Z, et al. Antibacterial and Antibiofouling Properties of Light Triggered Fluorescent Hydrophobic Carbon Quantum Dots Langmuir–Blodgett Thin Films. ACS Sustain Chem Eng 2018;6:4154–63. doi:10.1021/acssuschemeng.7b04566.

[284] Kováčová M, Marković ZM, Humpolíček P, Mičušík M, Švajdlenková H, Kleinová A, et al. Carbon Quantum Dots Modified Polyurethane Nanocomposite as Effective Photocatalytic and Antibacterial Agents. ACS Biomater Sci Eng 2018;4:3983–93. doi:10.1021/acsbiomaterials.8b00582.

[285] Nečas D, Klapetek P. Gwyddion: an open-source software for SPM data analysis. Open Phys 2012;10:181–8. doi:10.2478/s11534-011-0096-2.

[286] Ruiz V, Yate L, García I, Cabanero G, Grande H-J. Tuning the antioxidant activity of graphene quantum dots: Protective nanomaterials against dye decoloration. Carbon 2017;116:366–74. doi:10.1016/J.CARBON.2017.01.090.

[287] Ishibashi KI, Fujishima A, Watanabe T, Hashimoto K. Detection of active oxidative species

in TiO2 photocatalysis using the fluorescence technique. Electrochem Commun 2000;2:207–10. doi:10.1016/S1388-2481(00)00006-0.

[288] ISO. Measurement of antibacterial activity on plastics and other non-porous surfaces. Norma ISO 22196 2011. doi:10.1017/CBO9781107415324.004.

[289] Kwon W, Rhee S-W. Facile synthesis of graphitic carbon quantum dots with size tunability and uniformity using reverse micelles. Chem Commun 2012;48:5256. doi:10.1039/c2cc31687k.

[290] Budimir M, Marković Z, Jovanović D, Vujisić M, Mičušík M, Danko M, et al. Gamma ray assisted modification of carbon quantum dot/polyurethane nanocomposites: Structural, mechanical and photocatalytic study. RSC Adv 2019;9:6278–86. doi:10.1039/c9ra00500e.

[291] Al-Harthi SH, Elzain M, Al-Barwani M, Kora'a A, Hysen T, Myint MTZ, et al. Unusual surface and edge morphologies, sp2 to sp3 hybridized transformation and electronic damage after Ar+ ion irradiation of few-layer graphene surfaces. Nanoscale Res Lett 2012;7:466. doi:10.1186/1556-276X-7-466.

[292] Tamada Y, Ikada Y. Effect of preadsorbed proteins on cell adhesion to polymer surfaces. J Colloid Interface Sci 1993;155:334–9. doi:10.1006/jcis.1993.1044.

[293] Alves P, Coelho JFJ, Haack J, Rota A, Bruinink A, Gil MH. Surface modification and characterization of thermoplastic polyurethane. Eur Polym J 2009. doi:10.1016/j.eurpolymj.2009.02.011.

[294] Chvedov D, Arnold A. Effect of Surface Topography of a Rolled Sheet on Contact Angle. Ind Eng Chem Res 2004;43:1451–9. doi:10.1021/ie0307131.

[295] Wenzel RN. Resistance of solid surfaces to wetting by water. Ind Eng Chem 1936;28:988–94. doi:10.1021/ie50320a024.

[296] Gorna K, Gogolewski S. The effect of gamma radiation on molecular stability and mechanical properties of biodegradable polyurethanes for medical applications. Polym Degrad Stab 2003;79:465–74. doi:10.1016/S0141-3910(02)00362-2.

[297] Mitra S, Chandra S, Kundu T, Banerjee R, Pramanik P, Goswami A. Rapid microwave synthesis of fluorescent hydrophobic carbon dots. RSC Adv 2012;2:12129–31. doi:10.1039/c2ra21048g.

[298] Yan H, He C, Li X, Zhao T. A solvent-free gaseous detonation approach for converting benzoic acid into graphene quantum dots within milliseconds. Diamond Relat Mater 2018;87:233–41. doi:10.1016/J.DIAMOND.2018.06.008.

[299] Eda G, Lin Y-Y, Mattevi C, Yamaguchi H, Chen H-A, Chen I-S, et al. Blue Photoluminescence from Chemically Derived Graphene Oxide. Adv Mater 2010;22:505–9. doi:10.1002/adma.200901996.

[300] Ge J, Lan M, Zhou B, Liu W, Guo L, Wang H, et al. A graphene quantum dot photodynamic therapy agent with high singlet oxygen generation. Nat Commun 2014;5:1–8. doi:10.1038/ncomms5596.

[301] Jovanović SP, Marković ZM, Syrgiannis Z, Dramićanin MD, Arcudi F, Parola VL, et al. Enhancing photoluminescence of graphene quantum dots by thermal annealing of the graphite precursor. Mater Res Bull 2017;93. doi:10.1016/j.materresbull.2017.04.052.

[302] Yan X, Li B, Cui X, Wei Q, Tajima K, Li L. Independent Tuning of the Band Gap and Redox Potential of Graphene Quantum Dots. J Phys Chem Lett 2011;2:1119–24. doi:10.1021/jz200450r.

[303] Chong Y, Ge C, Fang G, Tian X, Ma X, Wen T, et al. Crossover between Anti- and Pro-oxidant Activities of Graphene Quantum Dots in the Absence or Presence of Light. ACS Nano 2016;10:8690–9. doi:10.1021/acsnano.6b04061.

[304] Lion Y, Delmelle M, Van De Vorst A. New method of detecting singlet oxygen production. Nature 1976;263:442–3. doi:10.1038/263442a0.

[305] Moan J, Wold E. Detection of singlet oxygen production by ESR. Nature 1979;279:450–1. doi:10.1038/279450a0.

[306] Ruiz-Morales Y, Mullins OC. Singlet-triplet and triplet-triplet transitions of asphaltene PAHs by molecular orbital calculations. Energ Fuel 2013;27:5017–28. doi:10.1021/ef400168a.

[307] Bregnhøj M, Westberg M, Jensen F, Ogilby P, Chemistry. Solvent-dependent singlet oxygen lifetimes: temperature effects implicate tunneling and charge-transfer interactions. Phys Chem Chem Phys 2016;18:22946–61.

[308] Jesenská S, Plíštil L, Kubát P, Lang K, Brožová L, Popelka Š, et al. Antibacterial nanofiber materials activated by light. J Biomed Mater Res - Part A 2011;99 A:676–83. doi:10.1002/jbm.a.33218.

[309] Henke P, Kozak H, Artemenko A, Kubát P, Forstová J, Mosinger J. Superhydrophilic polystyrene nanofiber materials generating O 2(1Δg): Postprocessing surface modifications toward efficient antibacterial effect. ACS Appl Mater Interfaces 2014;6:13007–14. doi:10.1021/am502917w.

[310] Barneck MD, Rhodes NLR, de la Presa M, Allen JP, Poursaid AE, Nourian MM, et al. Violet 405-nm light: a novel therapeutic agent against common pathogenic bacteria. J Surg Res 2016;206:316–24. doi:10.1016/j.jss.2016.08.006.

[311] Liu Y, Zeng X, Hu X, Hu J, Zhang X. Two-dimensional nanomaterials for photocatalytic water disinfection: recent progress and future challenges. J Chem Technol Biotechnol 2019;94:22–37. doi:10.1002/jctb.5779.

[312] Cho M, Chung H, Choi W, Yoon J. Linear correlation between inactivation of E. coli and OH radical concentration in TiO2 photocatalytic disinfection. Water Res 2004;38:1069–77.

[313] Attri P, Kim YH, Park DH, Park JH, Hong YJ, Uhm HS, et al. Generation mechanism of hydroxyl radical species and its lifetime prediction during the plasma-initiated ultraviolet (UV) photolysis. Sci Rep 2015;5. doi:10.1038/srep09332.

[314] Painter KL, Strange E, Parkhill J, Bamford KB, Armstrong-James D, Edwards AM. Staphylococcus aureus adapts to oxidative stress by producing H2O2-resistant small-colony variants via the SOS response. Infect Immun 2015;83:1830–44. doi:10.1128/IAI.03016-14.

[315] Anselme K. Osteoblast adhesion on biomaterials. Biomaterials 2000;21:667–81. doi:10.1016/S0142-9612(99)00242-2.

[316] Khalili AA, Ahmad MR. A Review of cell adhesion studies for biomedical and biological applications. Int J Mol Sci 2015;16:18149–84. doi:10.3390/ijms160818149.

Abbreviations and acronyms:

0D – zero dimensional

2D – two dimensional

3D – three dimensional

AFM – atomic force microscopy

Au NH – gold nanoholes

BHI – brain hearth infusion

BL – blue light

CA – community-acquired

CQDs – carbon quantum dots

CVD – chemical vapor deposition

CCM – Czech Collection of Microorganisms

DBPs – disinfection by-products

DMEM – Dulbecco's Modified Eagle's medium

DMA – Dynamic mechanical analysis

DNA – Deoxyribonucleic acid

DPPH – 2,2-diphenyl-1-picrylhydrazyl

EPR – electron paramagnetic resonance

FBS – fetal-bovine serum

FET – field effect transistor

FTIR – Fourier transform infrared

GO – Graphene oxide

GQD – graphene quantum dots

HAI – hospital-acquired infections

hCQDs – hydrophobic carbon quantum dots

HOPG – highly oriented pyrolytic graphite

ITO - indium tin oxide

LB medium – Luria Bretani medium

LED - light-emitting diodes

MB – methylene blue

MRSA – methicillin-resistant *S. aureus*

MWCNTs – multi-walled carbon nanotubes

NIR – near-infrared

NPs – nanoparticles

OD – optical density

PB – Prussian blue

PBS – phosphate buffer saline

PDT – photodynamic therapy

PEG – polyethylene glycol

PEI – polyethyleneimine

PET – polyethylene terephthalate

PL – photoluminescence

PMMA – polymethylmethacrylate

POC – point of care

PSs – photosensitizers

PS – Polystyrene

PTT – photothermal therapy

PU – polyurethane

PVC – polyvinyl chloride

PVP – polyvinyl pyrrolidine

rGO – reduced graphene oxide

RNA – ribonucleic acid

ROS – reactive oxygen species

RSA – radical scavenging activity

SEM – scanning electron microscopy

SiC – silicon carbide

SWCNTs – single-walled carbon nanotubes

TBO – toluidine blue O

TEM – transmission electron microscopy

TEMP – 2,2,6,6-tetramethylpiperidine

TEMPO – 2,2,6,6-tetramethylpiperidine-1-oxyl

WHO – World Health Organization

XPS – X-ray photoelectron spectroscopy

Biography

Milica Budimir was born on February 24th, 1988 in Ćuprija, Serbia. In May 2013, she has graduated from the University of Belgrade, School of Electrical Engineering, Department – Physical Electronics: Nanoelectronics and Photonics. She finished her Master's studies in 2014, at the School of Electrical Engineering with the master thesis "Atomic Force Microscopy of bacteria treated with nanoparticles".

In January 2013, she started working as an intern at the Vinča Institute of Nuclear Sciences, in the Laboratory for Radiation Chemistry and Physics, within the Carbon Nanomaterials Group, where she performed the experimental part of her Master thesis. In March 2015, she started working as a Research Assistant at "Vinca" Institute of Nuclear Sciences.

She started her Ph.D. studies in 2015, at the School of Electrical Engineering, the module for Nuclear, Biomedical, and Ecological Engineering. In 2016, she was granted with Scholarship of the French Government for co-tutorial Ph.D. studies between the University of Lille - Institute of Electronics, Microelectronics and Nanotechnology (IEMN) and University of Belgrade - School of Electrical Engineering. She has spent 16 months in Lille, working at the Institute of Electronics, Microelectronics, and Nanotechnology (IEMN), where she performed one experimental part of her thesis.

Her research interest is in the field of carbon nanomaterials and their biomedical and ecological application. During her doctoral studies, she has been working on the synthesis of carbon nanomaterials and their nanocomposites with different polymers, characterization of these materials, and their antibacterial applications.

Milica Budimir was a co-author of 20 articles and one book chapter. She was the first author of two papers, which are directly connected to the thesis, and she was a participant at four International Conferences.

Bibliography

Papers connected to the thesis:

1. Milica Budimir, Roxana Jijie, Ran Ye, Alexandre Barras, Sorin Melinte, Alejandro V Silhanek, Zoran Markovic, Sabine Szunerits, Rabah Boukherroub: *Efficient capture and photothermal ablation of planktonic bacteria and biofilms using reduced graphene oxide-polyethyleneimine flexible nanoheaters*. Journal of Materials Chemistry B (Back cover page) 03/2019; 7(17)., IF=5.047, DOI:10.1039/C8TB01676C

2. Milica Budimir, Zoran Marković, Dragana Jovanović, Miloš Vujisić, Matej Mičušík, Martin Danko, Angela Kleinová, Helena Švajdlenková, Zdeno Špitalský, Biljana Todorović Marković: *Gamma ray assisted modification of carbon quantum dot/polyurethane nanocomposites: Structural, mechanical and photocatalytic study*. RSC Advances 01/2019; 9(11):6278-6286., IF=3.049, DOI:10.1039/C9RA00500E

3. Milica Budimir, Duska Kleut, Biljana Todorovic Markovic, Rabah Boukherroub: *Reduced graphene oxide-chitosan flexible nanocomposite for efficient bacteria capture and photothermal ablation.* Resolution and Discovery 2020, accepted manuscript

Book chapter:

- Milica Budimir, Zoran Markovic, Sabine Szunerits, Rabah Boukherroub: Nanomaterials for Sustainable Energy and Environmental Remediation - Chapter 9: *Nanoscale materials for the treatment of water contaminated by bacteria and viruses*, Elsevier, Materials Today 2020, 261-305. DOI:10.1016/B978-0-12-819355-6.00009-1